UNIVERSITY OF CALIFORNIA
RIVERSIDE

Design of Fluorescent Tools and Fluorophores for Bioimaging, Photonics and Charge Transfer

A Dissertation submitted in partial satisfaction
of the requirements for the degree of

Doctor of Philosophy

in

Bioengineering

by

John A Clark

June 2023

Dissertation Committee:
Dr. Valentine I. Vullev, Chairperson
Dr. Hyle Park
Dr. William Grover

The Dissertation John A Clark is approved:

Committee Chairperson

University of California, Riverside

Acknowledgements

There are numerous people I would like to thank for all the help along this journey. I stand on the shoulders of giants and am incredibly humbled by the people I have had the honor of working with over the several years I spent at UCR. I have an incredible lab and support group that has helped and taught me so much. I am beyond grateful.

I want to begin with Dr. Vullev who has shown me an overwhelming amount of support from the moment he met me. From a young undergrad until a graduating PhD he has always treated me with the upmost consideration and kindness while mentoring me for optimal growth. He has inspired and encouraged me to achieve something I would have never thought was possible. With his confidence and support in my endeavors I felt like I could accomplish any task and I don't believe I can ever adequately convey how much he means to me and how much of an impact he has had on my life over the last 10 years. Thank you Dr. Vullev.

I couldn't imagine having as nearly as much success if not for my group of phenomenal lab members and best friends. Dr. Espinoza who has shown me many techniques and pushed me to collaborate on multiple projects. Dr. Derr who always been there when I needed for any lab synthetic help and always up for our favorite delicacy of tacos. Maryann, Dr. Rybicka-Jasinska, Mimi, Chin, Gregory, Omar, Dr. Nunez and many more. The entire Gryko lab from Poland who greatly improved my synthetic skills. Also I would like to thank Dr. Frank Quina for all the collaborative work we have accomplished.

It was an honor to have my committee composed of Dr. Park and Dr. Grover. Both of you have had profound effects on me through the years with your classes and mentorship. Working with Dr. Park in BMES helped shape me professionally and introduced me to undergraduate research so many years ago.

I'm incredibly grateful for everything you have all done for me during the time I have spent here. I would not be where I am if not for your kind words, honest opinions, help and advice. From the bottom of my heart thank you so much.

ABSTRACT OF THE DISSERTATION

Design of Fluorescent Tools and Fluorophores for Bioimaging, Photonics and Charge Transfer

by

John A Clark

Doctor of Philosophy, Graduate Program in Bioengineering
University of California, Riverside, June 2023
Dr. Valentine I. Vullev, Chairperson

Fluorescence is a radiative-deactivation phenomenon of broad importance for optical imaging and sensing. Fluorescence also can serve as a signal for characterizing excited-state dynamics and the kinetics of other parallel processes such as energy transfer and charge transfer (CT). The importance of CT cannot be overstated. In addition to sustaining life on earth in photosynthesis, cellular respiration and redox enzymatic conversions, CT ensures the modern ways of living possible as a part of electronics photonics and energy conversion. My work focuses on developing methods for characterizing fluorescent chromophores and redox species that can undergo CT. The viscosity of the microenvironment can have a huge impact on the fluorescence properties of photoprobes of biological importance. After a brief introduction, the second chapter of my dissertation describes the development of methodology for utilizing a thermoset transparent polymer as a room-temperature solid solvent for spectroscopy applications. With ultimately large viscosity, this solid-state media shows significant effects on suppressing non-radiative pathways of deactivation and enhancing the fluorescence quantum yields of certain dyes by orders of magnitude. The third chapter describes a method for expanding the applicability of cyclic voltammetry (CV),

which is the most widely used technique in electrochemical analysis. My work demonstrates how to obtain useful information, in terms of standard electrochemical potentials, from voltammograms showing irreversible behavior. Such information is essential for characterizing electron donors and acceptors for CT systems. The fourth chapter demonstrates the utility of spectroscopic and electrochemical studies for CT. Fundamental scientific studies show the importance of hydrogen bonding for transferring holes and electrons in peptide conjugates. Deciphering structure-function relationships also demonstrates how hydrogen-bonding propensity of fluorescent probes, which can act as electron donors and acceptors, can induce well-defined folds in oligopeptides that are as short as four residues. These fundamental-science studies set an important foundation for electronics, photonics and bioinspired engineering.

Table of Contents

List of figures

List of Schemes

List of Tables

List of Charts

List of Abbreviations

CT: Charge Transfer

CV: Cyclic Voltammetry

ET: Electron Transfer

HT: Hole Transfer

HOMO: Highest Occupied Molecular Orbital

LUMO: Lowest Unoccupied Molecular Orbital

PCT: Photoinduced Charge Transfer

PET: Photoinduced Electron Transfer

FRET: Forster Resonance Energy Transfer

PDMS: oly(dimethylsiloxane)

(ϕ_f): Quantum yield

(τ): Lifetime

k_f : radiative decay rate

k_{nd} : non radiative decay rate

THIA: 3,3'-diethylthiacyanine Iodide

ThT: thioflavin T

SOA: Sucrose Octaacetate

DCM: Dichloromethane

$E^{(0)}$: Electrochemical Potentials

$E^{(1/2)}$: Halfwave Potentials

E_a: Anodic Potentials

$E^{(p)}$: Peak Potentials

E_c: Cathodic Potentials

$E^{(p/2)}$:Half Peak Potentials

$E^{(e)}$ = edge potential

MeCN: Acetonitrile

SCE: saturated calomel electrode

C_{el} : Concentration of Electrolyte

H^0: Null Hypothesis

Aa: Anthranilamide

PDI: Perylene-diimide

Cor: Corrole

DBA: donor-bridge-acceptor

Phe: Phenylalanine

Ala: Alanine

CR: Charge Recombination

TA: Transient Absorption

Chapter 1:

Introduction

Fluorescence and Energy

Fluorescence is an indispensable tool with widespread versatility which we utilize for pathogen detection, labeling and more. The energy of light via emission is an amazing analytical tool to probe and measure fundamental processes such as charge transfer (CT) and energy transfer which are essential for every life sustaining process on earth. My research endeavors encompass studies which utilize fluorescence interactions between photoprobes as well as characteristic donors and acceptor molecules to monitor and track complex CT processes.

When the highest occupied orbitals (HOMO) and lowest unoccupied orbital (LUMO) are oriented in such a way between donor and acceptors we may induce electron transfer (ET) or hole transfer (HT). ET is accomplished by an electron passing from the LUMO of the donor to the LUMO of the acceptor. The result would grant a CT state of a radical cation on the donor while a radical anion on the acceptor. When there is a vacancy on the HOMO of the acceptor then electron may move from HOMO of the donor to fill the vacancy which is result also in a CT state. The HOMO and LUMO must be oriented between donor and acceptor molecules to facilitate this process but often we require additional excitation energy for these processes to proceed. Photoinducing the donor or acceptor can lead to excited state species and then CT which is referred to as photoinduced CT (PCT) via PET or PHT.

Photoprobes (which are fluorescent molecules) may have multiple deactivation pathways that are dominated by non-radiative routes of energy dissipation in one environment but radiative in a different environment. Discoveries of such photoprobes by staining can be arduous and untimely. It is why my initial endeavor of research involves the use of polydimethylsiloxane as a room temperature solid state solvent for emulating vicious

environments to observe emission enhancement of such photoprobes. Influencing fluorophores to alter favorable deactivation pathways lead my interests into understanding other properties needed to understand the driving forces that govern CT. My next focus delved into finding a means to approximate the electrochemical properties when chemical irreversibility is prevalent. Indeed, by use of differential analysis I was able to use the inflection point of cyclic voltammograms to calculate reduction potentials. Having cultivated this knowledge and understanding of light energy particle interactions and electrochemical band gaps poised my studies of the influence of peptide linkers in CT. Significant impact of research (1) design of PDMS fluorescence tool for solid state optical measurements (2) implementation of practical methods for approximating reduction potentials and (3) revelation hydrogen bonding facilitated CT dynamics in oligopeptides linkers between donor bridge acceptor motifs.

Luminescence is the emission of light from any substance and occurs from electronically excited states[1] and can be divided between fluorescence and phosphorescence. In fluorescence, singlet state transitions involve electrons paired of opposing spins moving between ground and excited orbitals and emitting a photon during deactivation. Charge transfer encompasses a transition of states between two materials of different spatial distribution of charged particles, for example electrons and protons[(1,2)].

Fluorophores and Energy Dissipation

Diverse fluorophores with an unlimited combination of substituents or arrangements allows so much versatility in energy deactivation pathways. It is often difficult to know which desired properties can be optimum for desired studies. For example, a fluorescence

enhancement mechanism of restricted intramolecular rotations is needed to have a meaningful interaction with staining of beta proteins commonly found in bacterial cell walls [3,4]. Immobilization of the fluorophore leads to an emission enhancement thus granting great signal to noise ratio between the immobile and mobile fluorophores. Other molecules may be governed by different dynamics that may render their utility as a stain null and such a binding may lead to quenched fluorescence. In fact, even pairing two fluorophores where the absorption of one fluorophore overlaps with the emission of another may lead to the very known Forster Resonance Energy Transfer (FRET) when they are in proximity to one another [5.6]. Indeed, the versatility of fluorophores renders their use widespread for a myriad of applications.

To obtain insight as to the electrical properties of fluorophores for use in CT studies it is essential to know their reduction potential. Electrochemical properties can be revealed via cyclic voltammetry to approximate and measure their electrical band gap. Cyclic voltammetry involves varying the voltage and monitoring the change in current. From here we understand how much of a potential change in voltage is required to push or pull an electron from the molecule. In previous studies we have demonstrated that taking measurements of multiple electrolyte concentrations will allow us to perform calculations for neat solvents [7]. This will also enable us to calculate the driving force of a CT. Knowing the driving force will grant insight as to if CT is feasible between any two potential donor or acceptor molecules. Not all analytes exhibit chemical reversibility and calculating correct values becomes difficult with conventional methodologies applied to irreversible behavior. It is such imperative to approximate reduction potentials that do not elicit nicely reversible and symmetric voltammograms reliably and so we delved into a study to ascertain a robust

methodology to accomplish this endeavor by differential analysis that involves taking the first and second derivative of acquired voltammograms.

Biological peptide residue's charge transfer properties are of great interest. Long range charge transfer is essential for all living processes that we know of. Elucidating the factors that control the rates of long-range electron transfer remains an outstanding challenge, owing in part to the complexity of proteins and other macromolecular structures that mediate such processes. We have found that it is possible to ensure ultrafast electron transfer in Donor-short peptide-Acceptor architectures *via* the choice of a donor and acceptor capable of forming hydrogen bonds and judiciously positioned intramolecular hydrogen bonds. We have found that electronic coupling through intramolecular hydrogen bonds accounts for ultrafast electron and hole transfers through a bridging tetrapeptide in a conjugate of a donor and acceptor. In our studies we have chosen donor and acceptor photoprobes that we can locally excite and monitor. Our work constitutes a new paradigm in designing efficient donor-acceptor systems for mediating efficient electron transfer.

References

1. S. Rather, V. Saraswatula, G. Sharada, S. D, B. Saha (2019) *New Journal of Chemistry*. 43 (44): 17146–17150.

2. K. Goetz, D. Vermeulen, M. Payne, C. Kloc, L. McNeil, O. Jurchesc (2014). *J. Mater. Chem. C.* 2 (17): 3065–3076.

3. D. Voet,JG. Voet (2004) *Biochemistry* (3rd ed) *Wiley.* pp. 227–231.

4. JS. Richardson,DC. Richardson. (2002) *PNAS*. 99 (5): 2754–9.

5. V. Helms (2008). *Principles of Computational Cell Biology. Weinheim: Wiley-VCH*. p. 202.

6. H. Schneckenburger (2009). *Methods and Applications in Fluorescence.* 8 (1): 013001.

7. D. Bao, S. Ramu, A. Contreras, S. Upadhyayula, J. M. Vasquez, G. Beran, and V. I. Vullev (2010). J. Phys. Chem. B, 114, 14467.

Chapter 2:

PDMS as a solid-state solvent for photophysical studies

ABSTRACT. Medium viscosity strongly affects the dynamics of solvated species and can drastically alter the deactivation pathways of their excited states. This study demonstrates the utility of poly(dimethylsiloxane) (PDMS) as a room-temperature solid-state medium for optical spectroscopy. This thermoset elastic polymer is transparent in the ultraviolet (UV), visible and near infrared (NIR) spectral regions. It is easy to mold into any shape forming surfaces with pronounced smoothness. PDMS is susceptible to reversible swelling in a range of organic solvents, offering a facile means for loading samples into its sold matrix. Transferring molecular-rotor dyes, used for staining prokaryotic cells and amyloid proteins, from non-viscus solvents into PDMS induces fluorescence enhancement amounting to a three-orders-of-magnitude increase in their fluorescence quantum yields and the lifetimes of their emissive excited states. These findings demonstrate the unexplored potential of PDMS as a solid solvent in a broad range of spectroscopic applications.

Introduction

Solid-state solvating matrices restrict conformational dynamics and translational degrees of freedom, permitting the emergence of excited-state pathways that are undetectable in liquid solutions. When large-amplitude structural relaxation drives dominating non-radiative decays, observing radiative deactivation requires rigid media.[(1)] Employing solid optically-transparent solvents has led to important discoveries in science, such as the first demonstration of the Marcus inverted region.[2]

Traditionally, flash-frozen organic solutions, where the solvents form solid glass structures, offer the rigid environment required for phosphorescence and Stark-spectroscopy measurements, for example.[3] In addition to the increased complexity of cryogenic setups, the liquid-nitrogen temperatures are not quite relevant to the ambient conditions of every-day life and biological systems. Introducing molecular samples into porous solids, such as zeolites, provides rigid environment at elevated temperatures.[4] The pore diameter of such minerals, however, restricts the sizes of molecules and ions that are possible to absorb in them. Dissolving molecular species in prepolymer mixtures, followed by the polymerization itself, presents another approach for forming solid solutions.[5] For the fidelity of such methods, however, the polymerization chemistry must not interfere with the examined species.

Sucrose octaacetate (SOA) is a crystalline material that melts at 86.5 ºC. When allowed to cool under ambient conditions, molten SOA solidifies into transparent glass. Dissolving molecular (or other) species in molten SOA and letting it cool down produces room-temperature solid-state solutions.[6] Due to formation of SOA crystalline phase, however, such glass samples lose their transparency when kept for extended periods of time. In addition, the elevated temperature of molten SOA may compromise the stability of the examined species.

Herein, we examine the utility of PDMS as a solid-state solvent involving room-temperature sample preparation and spectroscopic examination. Despite its importance for fabricating microfluidic devices and other microelements with pronounced biocompatibility, PDMS swells in a range of organic solvents increasing its volume by a factor of two or more.[7,8] While this swelling in non-reactive solvents is reversible, i.e., PDMS restores its shape and size upon removal of the solvent, it presents a principal limitation for the applicability of

devices made of this polymer. Nevertheless, we believe that this disadvantage for microdevices can prove immensely beneficial for loading PDMS with samples dissolved in the swelling solvents. Furthermore, PDMS is transparent between about 280 and 1,650 nm, making it promising for optical applications. Loading dyes referred to as "molecular rotors," namely, 3,3'-diethylthiacyanine (THIA) iodide and thioflavin T (ThT), into a PDMS matrix decreases the rates of non-radiative decay of their electronically excited states by about three orders of magnitude, which pronouncedly increases their fluorescence quantum yields (ϕ_f). This PDMS-induced emission enhancement is comparable to that observed for THIA and ThT not only when placed in a solid SOA glass, but also when taken up by Gram-positive and Gram-negative bacterial cells.

Fabrication of PDMS Cuvettes

Known as "silicon rubber," PDMS is a broadly used material in everyday life that is easy to prepare and mold. Prepolymer PDMS chains mixed together with a crosslinker, i.e., a curing agent, form a viscous liquid that can be poured into plastic or any non-silicon-based mold that precludes strong adhesion.[8]Upon photo- or thermal curing, following facile degassing under vacuum, the mold features imprint on the PDMS surface with sub-micrometer resolution. This property of PDMS made it widely popular for fabricating microfluidic devices that revolutionized the biological, biomedical and engineering research in the turn of this century.[8]

Employing 1-cm polystyrene cuvettes with four polished sides as molds allow us to prepare PDMS blocks that perfectly fit into the sample holders of most spectrophotometers and spectrofluorometers. The prepolymer mixture (PDMS, Slygard 184) poured into the polystyrene cuvettes and degassed under vacuum solidifies after left at room temperature for

about 24 hours (Figure 2-1). Breaking the polystyrene cuvette and removing the broken pieces leaves 1×1cm PDMS blocs with four smooth sides (Figure 2-1).

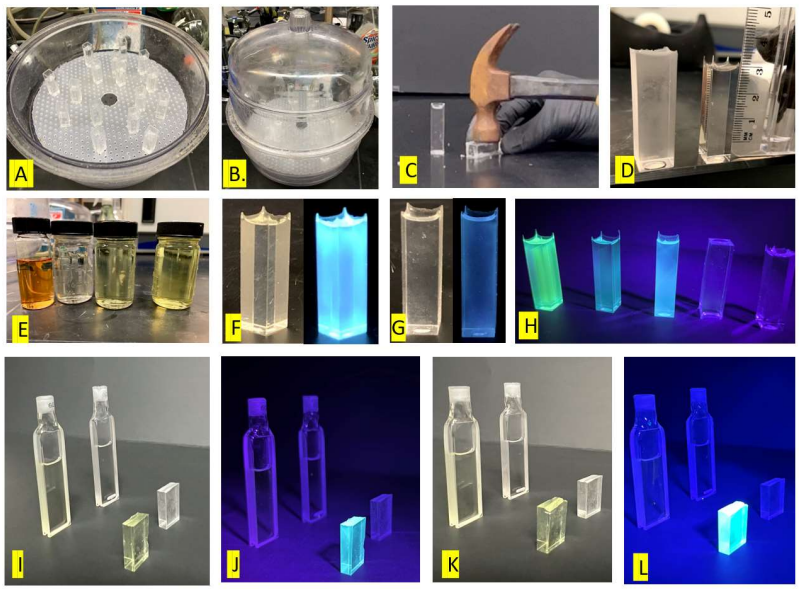

Figure 2-1. fabrication images of PDMS (A) poured into mold and then (B) vacuumed, followed by (C) breaking of cuvette mold. The PDMS is then swelled with DCM (D) as a wash and then shrunk prior to reswelling into desired photoprobe dissolved in DCM (E). Images of BF vs fluorescence is THIA (F) and THT (G) in PDMS blocks. Image of PDMS with various compounds (from right to left) Ani, THIA, ThT, Congo Red and Blank (H). BF image and fluorescent image of PDMS swelled in THIA (I, J) and ThT (K, L) next to concentrated dye in solution.

While aliphatic amines and hydrocarbons are the best swelling solvents for PDMS,[7,8] they can prove reactive or provide insufficient solubility for many samples of interests. On the other side of the spectrum, good solvents such as DMSO and DMF do not really swell PDMS.[7] Therefore, we select a chlorinated solvent, i.e., dichloromethane (DCM), as a compromise ensuring good swelling and sample solubility.[7] Furthermore, the volatility of DCM ensures its expedient and facile removal from the swollen PDMS blocks. Initial swelling in neat solvents allows removal of the non-crosslinked polymer chains and other impurities from the

polymerization process.[7,8] Placing the thus cleaned PDMS blocks (restored to their original sizes) in DCM solutions of THIA and ThT doubles their volumes and loads the dyes into them. After 24-hour soaking, we take the blocks out of the dye solutions, wash them with DCM and allow them to shrink to their original size by evaporating the solvent out of them (Figure 2-1D). The dye concentrations in the doped PDMS blocks (determined using optical absorption spectroscopy) is usually 7 to 10 times smaller than that of the concentrations of the DCM solutions and depends on the duration of soaking. The first most important observation is that the dye-doped PDMS blocks show stronger fluorescence than the concentrated DCM solutions of THIA and ThT (Figure 2-1 I-L). Furthermore, the intensity of the autofluorescence from the UV-illuminated PDMS blocks is negligibly small in comparison to the signals from the dye (Figure 2-1 I-L).

Results: Optical Spectroscopy of photoprobes in solvents

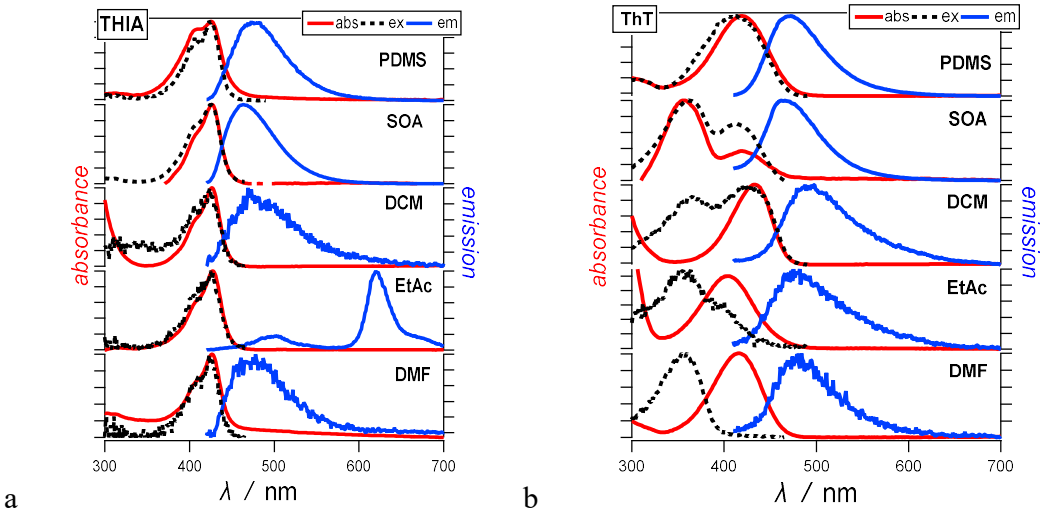

Figure 2-2. steady state spectroscopy absorption excitation and emission spectra of THIA (a) and ThT (b) in various solvents.

Steady-state spectra of THIA in most organic aprotic liquid solvents show absorption maxima around 427 nm (Figure 2-2), similar to what we observe for protic solvents.[10] The THIA fluorescence maxima vary between about 460 and 500 nm (Figure 2), with $\phi_f < 10^{-3}$ and picosecond lifetimes (τ) of the emissive excited states (Table 2-1). For a range of solvents, another emission band around 620 nm emerges (Figure 2), which we ascribe to excimer fluorescence since the absorption spectra, depicting the $S_0 \rightarrow S_1$ transition, do not show significant perturbations.

Table 2-1. Quantum yield (ϕ_f), lifetime (τ) radiative and non radiative decay rates (k_f and k_{nd}) of THIA and ThT for various solvents.

	THIA				*ThT*			
Solvent	ϕ_f [x 10^{-2}]	τ [ps]	k_f x 10^{-8} [s^{-1}]	k_{nd} x 10^{-8} [s^{-1}]	f_f [x 10^{-2}]	t [ps]	k_f x 10^{-8} [s^{-1}]	k_{nd} x 10^{-8} [s^{-1}]
EtAc	0.058	2.59	2.25	3860	0.10	3.35	3.06	2980
DCM	0.053	2.73	1.94	3660	0.52	2.92	18	3410
DMF	0.07	3.64	1.93	2750	0.18	1.68	10.4	5940
SOA	5.7	1140	50	37.6	54	2130	2.54	2.15
PDMS	15	1270	1.18	6.67	41	1910	2.15	3.09
B. sub	15	2740	0.547	3.10	1.5	1960	0.0765	5.03
B. mega	20	2710	0.738	2.95	2.3	1790	0.128	5.46
E. aero	9.2	2270	0.405	4.00	8.6	1660	0.518	5.51
E. coli	3.5	2690	1.3	2.42	6.2	1250	0.496	7.50

Calculated yields determined and referenced against standard coumarin 151 in ethanol same excitation wavelengths as from Table 1. Lifetimes found using Time correlated single photon counting using nanoLED with excitation pulse 406nm repetition rate 1MHz.

The steady-state spectra of ThT also reveal propensity for aggregation in aprotic organic solvents (Figure 2-2). In liquid media ThT is weakly fluorescent $\phi_f < 10^{-2}$ and $\tau < 5$ ps (Table 2-1), exhibiting a single absorption band with a maximum around 400 to 430 nm and a single fluorescence band around 430 to 500 nm (Figure 2-2). The excitation spectra of ThT in many

of the organic solvents, however, reveal a band at around 360 nm that is not present in the absorption spectra (Figure 2-2). It is consistent with the presence of small amount of strongly fluorescent species.

Placing THIA and ThT in a solid SOA glass drastically increases their ϕ_f to about 0.6 and τ to about 2 ns (Figure 2-2, Table 2-1). PDMS as a solvent medium also immensely enhances ϕ_f and τ of these to dyes but to a slightly lesser extent than SOA (Table 2-1). The SOA glass is more rigid than the elastic PDMS, which reflects the differences between the measured ϕ_f and τ for these two solid solvents. THIA and ThT in PDMS, as well as THIA in SOA, exhibit a single absorption and a single emission band (at $\lambda > 300$ nm) with excitation spectra matching the absorption features (Figure 2-2). Conversely, placing ThT in SOA leads to the emergence of: (1) a 360-nm band in the absorption and excitation spectra that dominates over the 420-nm one, and (2) a shoulder in the 470-nm fluorescence band. These spectra features are consistent with ground-state aggregation of ThT in SOA. Even though liquid siloxanes are not good solvents for THIA and ThT, the diffusion-driven loading of these two cationic dyes in the swollen PDMS appears to prevent aggregation that can lead to detectable perturbation in the absorption and emission steady-state spectra. This feature presents an advantage in using PDMS as a room-temperature solid solvent.

The radiative-decay rate constants, k_f, for THIA in the tested solid and liquid solvent media vary within a factor of two (Table 2-1). The rate constants of non-radiative deactivation, k_{nd}, of THIA in the solid SOA and PDMS, however, are about three orders of magnitude smaller than k_{nd} for the liquid solvents (Table 2-1). Despite the dye aggregation in the organic aprotic media that inherently induces overestimations of k_f, transferring ThT from the liquid to the

solid solvents also causes a three-orders-of-magnitude decrease in k_{nd} (Table 2-1). That is, the increased rigidity of the solvating microenvironment of these molecular rotors restricts the conformational freedom of their excited states, preventing them from relaxing to the conical intersections that mediate the internal conversion to the ground states, which is principally responsible for the observed picosecond non-radiative deactivation.[8] Most importantly, the PDMS matrix provides the necessary rigidity for slowing down the excited-state conformational dynamics leading to the drastic enhancement of the fluorescence of THIA and ThT.

a

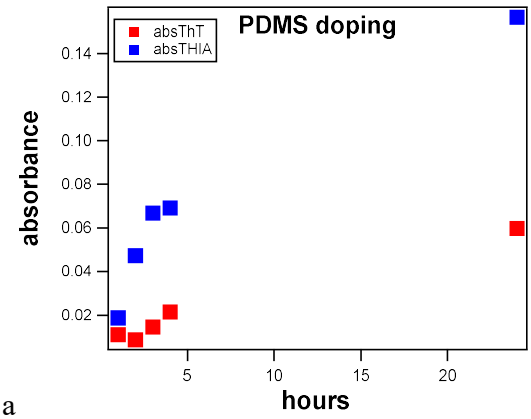

b

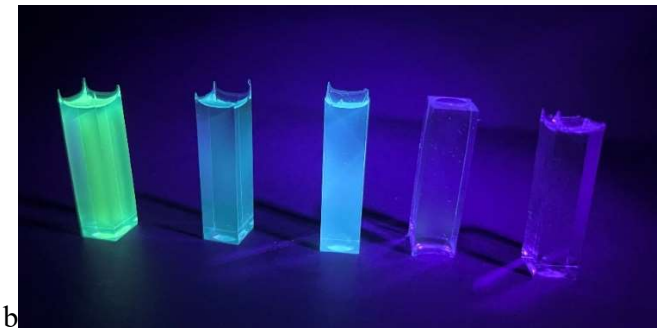

Figure 2-3. PDMS blocks were measured after 1, 2, 3, 4 and 24 hours (a) and image (b) of PDMS blocks swelled (from right to left: ANI, THIA, ThT, Congo Red and PDMS no solvent).

Table 2-2. PDMS blocks swelled with photoprobe after various times.

Time (hours)	Absorbance THIA	Absorbance ThT
1	0.019	0.011
2	0.047	0.009
3	0.067	0.015
4	0.069	0.022
24	0.16	0.060

A close examination of the PDMS blocks soaked in the THIA and ThT solutions, however, reveals stronger fluorescence at their sides and edges than from their bulk in the middle (Figure 2-1G). This heterogeneity of the doping is consistent with relatively slow mass transport of the dyes toward the center of the PDMS blocks.[10] The relatively fast swelling indicates that the solvent quickly diffuses into the bulk of the blocks and solvates the polymer chains. It takes 24 hours to reach maximal swelling and uptake of the photoprobe (Table 2-2). Nevertheless, even after soaking in the DCM solutions of THIA and ThT for 24 hours, the PDMS blocks reveal dye-concentration gradients from their exterior to their interior. Regardless this heterogeneity, the lack of detectable aggregation ensures that the shapes of the steady-state optical spectra and the fluorescence-decay curves are representative of single-dye molecules, perhaps with their counterions, solvated by the solid PDMS matrix.

For estimating relative ϕ_f from emission spectra recorded at a right-angle configuration, however, sample heterogeneity along the path of the excitation beam is essential to prevent

instrumental errors. Therefore, we prepare 3-mm-thick PDMS slabs for the quantum-yield measurements. The concentrations of the loaded THIA and ThT in the 3-mm slabs are higher than those in the 1-cm blocks to ensure $A(\lambda_{ex})$ between 0.1 and 0.2. Nevertheless, the decrease in the PDMS thickness improves the attained homogeneity across it. Employing small-angle front-face configuration for recoding the emission spectra of the thin PDMS samples for the ϕ_f calculations, further minimizes the potential errors from heterogeneity of the dye distribution (Table 2-1).

In addition to its affinity for siloxanes, the solubility of a dye in the swelling solvent is truly important for loading it into the PDMS matrices. The same loading procedure with Congo red, a dianioninc dye with worse solubility in DCM than THIA and ThT, yields PDMS blocks with only colored fluorescent patches of at their edges (Figure 2-3a). In contrast, 4-Amino-1,8-naphthalimide (ANI) derivatives, which have excellent solubility in chlorinated solvents, readily distribute homogeneously when loaded in PDMS (Figure 2-3a). THIA and ThT, therefore, represent a somewhat intermediate case where they load sufficiently well in PDMS block and thin slabs without aggregation allowing exploration of the effects of medium rigidity on their excited-state dynamics and photophysics.

The enormous fluorescence enhancement that medium rigidity can induce on ThT, along with its high propensity for binding to β-strand proteins, has made this dye an indispensable fluorescence probe for imaging amyloid proteins.[10] These same properties, allow ThT to serve as a photoprobe for fluorescence imaging of bacterial endospores and vegetative prokaryotic cells in biological samples, such as blood and cell extracts, as we previously reported.[11] The abundant β-sheet structures in spore coats and in the S-layers of proteins on the surface of

bacterial cell walls selectively bind ThT and drastically enhance its fluorescence. This photolabeling of bacterial spores and vegetative cells does not compromise their vitality and allows for real-time imaging of sporulation and germination for example.[10]

Cyanine dyes, such as THIA, have similar affinity for bacterial cells and have been the foundation for the discovery and the development of *dynamic staining*.[10] Instead of testing if a dye stains the cells or not, the kinetics of fluorescence enhancement originating from the dye uptake correlates with the type of the microbial species.([9,10)] It provides opportunities for expanding the staining analysis beyond their binary "yes/no" nature.

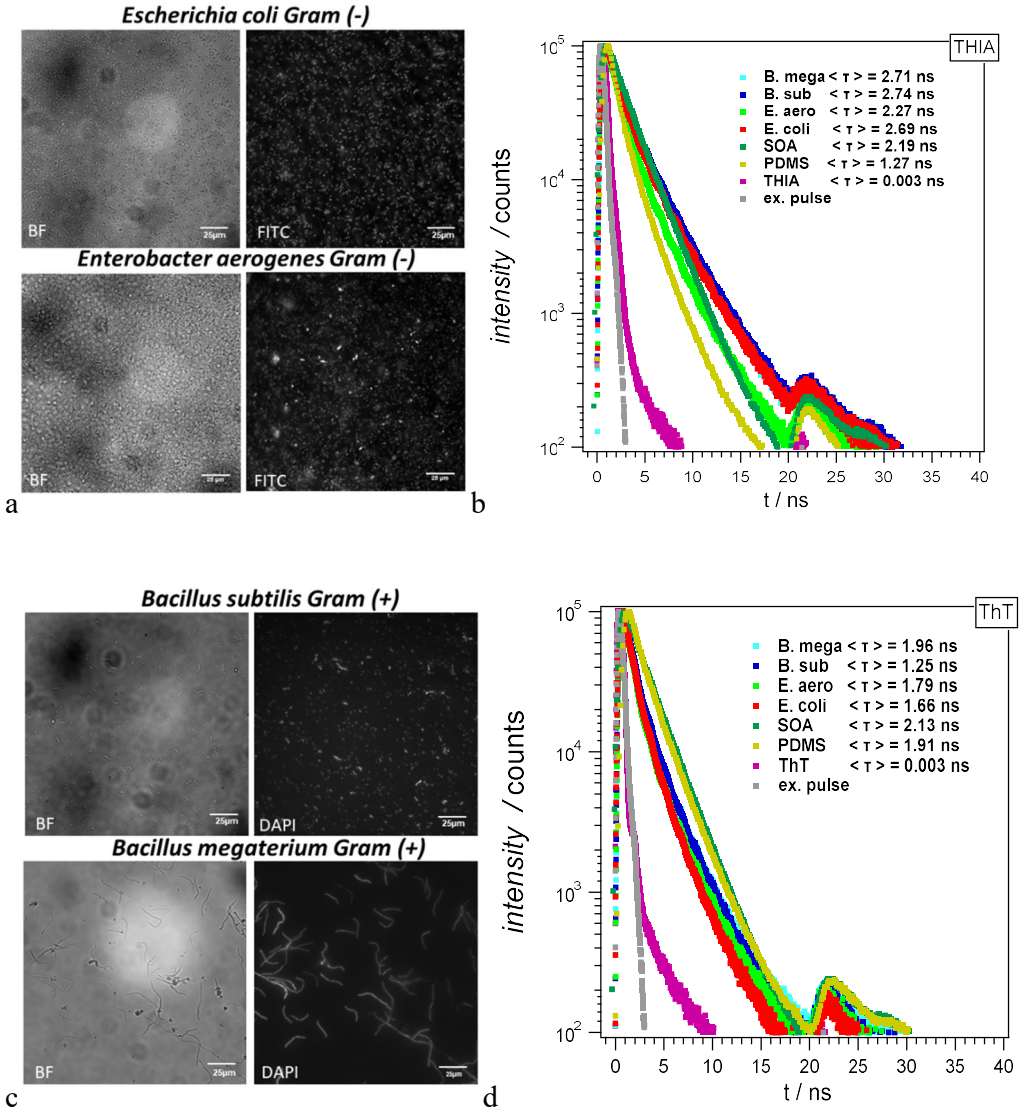

Figure 2-4. Brightfield and Fluorescent images of bacterial cells and TCSPC stained with THIA (a,b) and ThT (c,d).

Adding THIA and ThT solutions to suspensions containing Gram-positive and Gram-negative bacteria allows facile fluorescence imaging of the cells (Figure 2-4). Indeed, the dye taken up by the prokaryotic cells is strongly fluorescent. Conversely, the unbound dye in the liquid media does not fluoresce and interfere with the cell imaging. While τ of THIA and ThT in aqueous media is in the order of a picosecond, mixing THIA and ThT with the bacterial cells

increases τ to about 2 to 3 ns (Figure 2-4b,d). These trends of emission enhancement in the biological samples are similar to what we observe when transferring these two dyes from liquid organic solvents to SOA and PDMS solid media.

Conclusion

Emission enhancement due to rigid media provided by PDMS allows exploration of information otherwise inaccessible unless samples were subjected to harsher conditions. The swelling propensity of PDMS in a range of organic solvents provides an attractive means for facile loading of molecular and nanometer-scale samples in it under mild conditions. Its optical transparency, along with the ease of its preparation and molding, makes PDMS quite promising as a room-temperature solid-state solvent for a broad range of spectroscopy applications which may expedite revealing candidates of photoprobes for viscous based emission enhancement.

References

1. B. Valeur, M. Berberan-Santos (2011). *Journal of Chem Education.* 88 (6): 731–738. ISSN 0021-9584.

2. R. A. Marcus (2004) *Angew. Chem. lnr. Ed. Engl.*, **32**, 1111 (1993). D. Voet, JG. Voet*, Wiley.*

3. F. Nie, KZ. Wang, D. Yan *(*2006). *Nat Commun*. 14(1):1654 *Springer. pp. 162–206.*
4. Helms V Weinheim: *Wiley-VCH. p.* 202.

5. D. Bao, S. Ramu, A. Contreras, S. Upadhyayula, J. M. Vasquez, G. Beran, and V. I. Vullev (2010). *J. Phys. Chem. B*, **114**, 14467.

6. P. Shelley, T. Bannan, S. Worrall, M. Alfarra, U. Krieger, C. Percival, A. Garforth, and D. Topping (2020). *Atmos. Chem. Phys*, 20, 8293–8314.

7. J. NgLee, P. Cheolmin, and G. Whitesides. *Anal.Chem.*75,6544-6554(2003)

8. S. Upadhyayula, V. Nuñez, E. Espinoza,J. Larsen,D. Bao, D, Shi, J. Mac, B. Anvari and V. Vullev (2015). *Chem. Sci*, 6, 2237-2251

9. K. Jiao, CL. Graham, J. Wolff, RG. Iyer, P. Kohli. *J Memb Sci.*;401-402:25-32(2012).

10. S. Upadhyayula, S. La, A. Ha, HK. Malik-Chaudhry, V. Vullev. (2012) *Annu Int Conf IEEE Eng Med Biol Soc*; 2012:499-502

Chapter: 3:

Practical Aspects of Cyclic Voltammetry:

How to Estimate Reduction Potentials When Irreversibility Prevails

Abstract

What is the best approach for estimating standard electrochemical potentials, $E^{(0)}$, from voltammograms that exhibit chemical irreversibility? The lifetimes of the oxidized or reduced forms of the majority of known redox species are considerably shorter than the voltammetry acquisition times, resulting in irreversibility and making the answer to this question of outmost importance. Halfwave potentials, $E^{(1/2)}$, provide the best experimentally obtainable representation of $E^{(0)}$. Due to irreversible oxidation or reduction, however, the lack of cathodic or anodic peaks in cyclic voltammograms renders $E^{(1/2)}$ unattainable. Therefore, we evaluate how closely alternative potentials, readily obtainable from irreversible voltammograms, estimate $E^{(0)}$. Our analysis reveals that, when $E^{(1/2)}$ is not available, inflection-point potentials provide the best characterization of redox couples. While peak potentials are the most extensively used descriptor for irreversible systems, they deviate significantly from $E^{(0)}$, especially at high scan rates. Even for partially irreversible systems, when the cathodic peak is not as pronounced as the anodic one, the half-wave potentials still provide the best estimates for $E^{(0)}$. The importance of these findings extends beyond the realm of electrochemistry and impacts fields, such as materials engineering, photonics, cell biology, solar energy engineering and neuroscience, where cyclic voltammetry is a key tool.

Introduction

Cyclic voltammetry (CV) is the hallmark of electrochemical analysis and it impacts on countless fields outside of chemistry, such as materials science, photonics, cell biology,

neuroscience, electrical engineering and condensed-phase physics.1^{-1}0 Voltammograms provide a wealth of information about the charge-transfer and mass-transport processes at the surfaces of the working electrodes.[11–15] The evolving voltammetry theories, based on Butler-Volmer and Marcus-Hush formalisms, reveal key mechanistic insights about these interfacial phenomena.[16–20] Estimating standard electrochemical potentials ($E^{(0)}$) of oxidation and reduction encompasses one of the most widely spread uses of CV, which makes this technique popular. The strong correlation of $E^{(0)}$ with the energy levels of frontier orbitals and band edges defines the invaluable importance of the electrochemical potentials for characterization of electronic properties of molecular species and materials.

Combining the Butler-Volmer equation with Fick's second law results in an expression of the faradaic current (i_F) in terms of the applied potential $^{(e)}$, where $E^{(0)}$ is one of the parameters. This expression of i_F as a function of E, however, is an integral equation and its solution remain in the realm of numerical analysis, rendering it impractical for routine estimations of $E^{(0)}$ from voltammograms. Therefore, halfwave potentials ($E^{(1/2)}$) have become the preferred representation of $E^{(0)}$, i.e., $E^{(1/2)} \approx E^{(0)}$ for reversible oxidation and reduction. The average

between the anodic (Ea) and the cathodic (Ec) potentials define $^{(1/2)}$, which are facile to extract from cyclic voltammograms manifesting reversibility (Figure 1a).[11] This definition of $E^{(1/2)}$ also extends to quasireversible cases (i.e., chemically reversible and electrochemically irreversible) when the rates of interfacial electron transfer are slower that the rates of mass transport to and away from the electrode and $|E_a - E_c|$ increases with an increase in the scan rate.[11,21] The conundrum is how to estimate $E^{(0)}$ from voltammograms showing chemically irreversible oxidation and reduction (Figure 3-1b). Another question is how well $E^{(1/2)}$

estimates $E^{(0)}$ in the cases of partial chemical reversibility. For the rest of this discussion, we refer to chemical conversion, such as decomposition or dimerization, of the species produced on the electrode surface upon oxidation or reduction is the source of the observed chemical irreversibility. Two principal approaches allow for gaining reversibility: (1) increasing the scan rates so that the acquisition of the voltammograms is much faster than the lifetime of the formed oxidized or reduced species; and (2) lowering the temperature in order to slow down the undesired chemical conversions. The former approach produces voltammograms suffering from enormous capacitance currents (i_C) that are inherent for large scan rates. At scan rates of kV/s and MV/s, faradaic signals can be orders of magnitude smaller than the background, and decreasing the area of the working electrode, in order to decrease i_C, decreases the signal-to-noise ratios. Conversely, lowering the temperature sufficiently enough to attain reversibility limits the number of usable solvents with acceptable electrochemical windows due to their freezing points. Indeed, both of these approaches are quite involved, and they have not gained popularity as routine methods for electrochemical analysis.

When cyclic voltammograms show irreversible behavior, the most common practice involves reporting the peak potentials ($E^{(p)}$), i.e., anodic potentials (E_a) for oxidation or cathodic potentials (E_c) for reduction (Figure 3-1a). Voltammograms of reversible processes, however, elucidate that the values of the peak potentials deviate quite a bit from $E^{(1/2)}$, especially for large scan rates.

Another option involves the use of the edge potentials ($E^{(e)}$) of the anodic or cathodic waves as estimates of $E^{(0)}$ of irreversible processes (Figure 3-1). At the edges of the voltammogram waves, $E^{(e)}$ represents the potentials of the first detectable faradaic currents. Thus, $E^{(e)}$ underestimates $E^{(0)}$ of oxidation and overestimates $E^{(0)}$ of reduction by a few kBT/F

(kBT is the thermal energy and F is the Faraday constant). Conversely, we determined that the potentials, $E^{(i)}$ (Figure 1), at the inflection points of the anodic and cathodic waves are quite close to $E^{(1/2)}$ for reversible processes.[22] Therefore, we employ $E^{(i)}$ for estimating $E^{(0)}$ of irreversible oxidation and reduction.[23–27] Recently, Nicewicz et al. proposed the use of the half-peak potentials ($E^{(p/2)}$) for estimating $E^{(0)}$ of cyclic voltammograms showing irreversibility (Figure 3-1).[28] For symmetrical sigmoid curves progressing along the ordinate, the inflection points are at their half-heights, but the voltammogram waves do not necessarily have such a shape leading to the peaks.

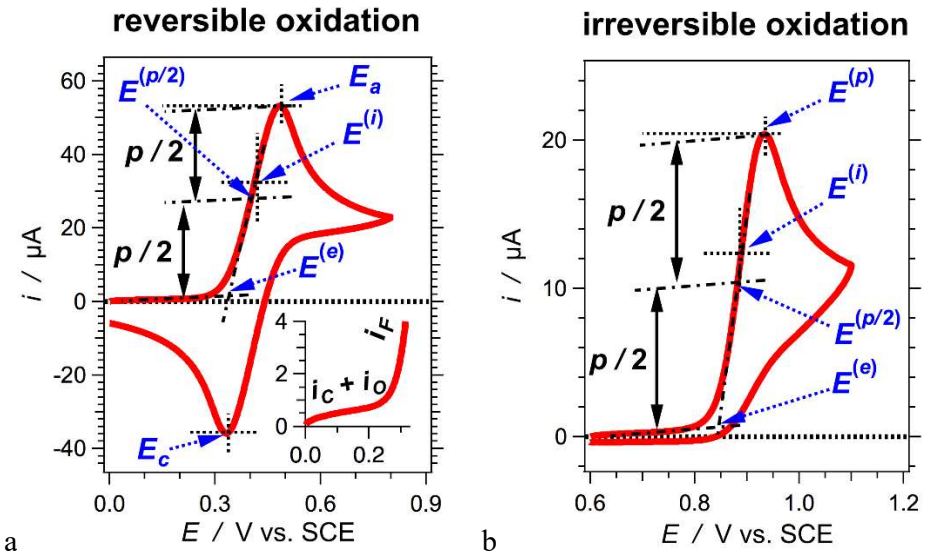

Figure 3-1. Examples of cyclic voltammograms showing chemically reversible and irreversible oxidation with designated potentials: E_a = anodic potential, E_c = cathodic potential, $E^{(i)}$ = inflection-point potential, $E^{(p/2)}$ = half-peak potential, $E^{(e)}$ = edge potential. (a) 1mM ferrocene. Inset: the initiation of the scan showing the rise of the faradaic current, i_F, on the background of the capacitance current, i_C, and the ohmic current, i_O. (b) 1 mM 4Pip. (For both voltammograms: 200 mM N(C4H9)4PF6 in MeCN, and v = 100 mV s^{-1}.)

Herein, we review $E^{(1/2)}$, $E^{(i)}$, $E^{(p/2)}$, $E^{(p)}$, and $E^{(e)}$ extracted from cyclic voltammograms for reversible, irreversible and partially reversible electrochemical oxidation. ANOVA analysis[29] provides statistical quantification of how close the values of $E^{(i)}$, $E^{(p/2)}$,

$E^{(p)}$, and $E^{(e)}$ are to those of $E^{(1/2)}$ for different scan rates. The values of $E^{(i)}$ are the closest to those of $E^{(1/2)}$, but $E^{(p/2)}$ fairs almost as well as $E^{(i)}$ in the statistical analysis. A straightforward differential analysis, i.e., the first and second derivatives of the cyclic voltammograms, provides convenient ways for determining peak potentials and inflection points.

In addition, this differential approach proves immensely beneficial for estimating the reversibility of the electrochemical processes. Regression analysis reveals that even for partially reversible system, $E^{(1/2)}$ still provides a good estimate for $E^{(0)}$.

Experimental and Methods

CV measurements were conducted using Reference 600 Potentiostat/Galvanostat/ZRA (Gamry Instruments, PA, U.S.A.), connected to a three-electrode cell equipped with a glassy carbon working electrode, an SCE reference electrode (connected to the cell via a salt bridge), and a platinum counter electrode, as previously described.32,33 The salt bridge was filled with a saturated KCl solution. Anhydrous acetonitrile (MeCN) was employed with different concentrations of a supporting electrolyte, N(C4H9)4PF6, N(C4H9)4BF4 and LiClO4. Prior to recording each voltammogram the sample is extensively purged with argon while maintaining its volume constant by adding more of the anhydrous solvent. For each sample, a set of voltammograms is recorded where the electrolyte concentration is increased from 25mM to 200mM in increments of 25 mM, at scan rates, v = 10, 20, 50, 100, 200 and 500 mV s^{-1}. For each sample and at each of the conditions and the scan settings, a triplicate of triplicates was measured, and the reported error bars represent plus-minus one standard deviation. That is, the same sample was

measured three times in three different days, and at each measurement three voltammograms were recorded.

Analysis of the voltammograms and the obtained electrochemical potentials was carried out using Igor Pro, v. 7.02 (WaveMetrics, Inc., Lake Oswego, Oregon, U.S.A.). The half-wave potentials, $E^{(1/2)}$, are determined from the midpoints between the cathodic and anodic peak potentials, E_a and E_c, respectively. Ea and Ec are determined from the zero points of the first derivatives of the voltammograms, i.e., the potentials where $\partial i/\partial E = 0$ at $\partial E/\partial t =$ constant. The inflection point potentials, $E^{(i)}$, are determined from the zero points of the second derivatives at the rising spans of the anodic waves of the voltammograms, i.e., the potentials where $\partial 2i/\partial E2 = 0$ at $\partial E/\partial t =$ constant.

When the signal-to-noise ratios of the second derivatives are not high enough, they are smoothed using 4^{th} order Savitzky-Golay algorithm. Linear fits of the voltammogram sections after the initial capacitance rise and before the faradaic wave provide the estimates for the baselines. Similar linear fits of the anodic waves after the beginning of the initial faradaic rise and before the curvature leading to the peak yields the anodic asymptotic lines. The edge potentials, $E^{(e)}$, are estimates from the points where these asymptotes cross the baselines. The peak heights, p, is determined from the current difference between the anodic peak and inclined baseline at the peak potential. The potentials at the points on the rising anodic wave that corresponds to p/2 provide the estimates for $E^{(p/2)}$. Functions, built in Igor Pro, were used for the statistical tests that produced the p-values.

General Considerations for voltammogram

For reversible processes, the CV-obtained values of $E^{(1/2)}$ offer excellent estimates for $E^{(0)}$. Irreversibility or partial reversibility, however, are significantly more prevalent than reversibility, especially for organic and bioorganic redox couples, and for protic and other potentially reactive media. Oxidative or reductive degradation, dimerization, reactions with the solvent, relatively fast mass transport and other processes that deplete the electrochemically produced species at the surface of the working electrode, strongly affect the recorded cyclic voltammograms making them "asymmetric" and even eliminating the anodic or the cathodic peak.

The pressing question at hand is how well $E^{(i)}$, $E^{(p/2)}$, $E^{(p)}$, and $E^{(e)}$ can serve as estimates for $E^{(0)}$ when $E^{(1/2)}$ is not available? The shapes of the voltammogramic waves depend on the electron-transfer kinetics, mass transport dynamics and scan rates, as well as on chemical reactions that deplete the analyte from the surface of the working electrode. For example, an increase in the scan rate can improve the reversibility if the lifetimes of the electrochemically produces species are comparable with the time spans between the beginning of the forward-scan wave and the end of the back-scan one. An increase in the scan rates, however, pushes the peak potentials away from $E^{(1/2)}$.

Therefore, if reversibility is not achieved, increasing the scan rates can prove detrimental, especially when $E^{(p)}$ provides the metrics for $E^{(0)}$. Concurrently, reversing the direction of the scans at potentials as soon as possible after the peak of the forward-scan waves can also improve the reversibility of the cyclic voltammograms. Bringing the potential of the scan reversal too close to the peak, however, can alter its shape and shift $E^{(p)}$.

The values of $E^{(p)}$ are most frequently reported for potentials of processes displaying irreversible voltammograms. The positions of the peaks of the voltammogramic waves, however, strongly depend on the scan rates, the sample concertation, and the kinetics of interfacial electron transfer especially when side reactions deplete the analyte from the electrode surface. Hence, $E^{(p)}$ is not invariant to the experimental settings. Inherently, the peak potentials can never overlap with $E^{(1/2)}$, and with $E^{(0)}$. Therefore, two-dimensional extrapolation of $E^{(p)}$ to zero scan rate and zero sample concentrations from multiple measurements is the way to obtain values from the peak potentials that are close to $E^{(0)}$.

Conversely, $E^{(e)}$ represents the potential at which the Fermi level of the working electrode approaches the energy level of the frontier orbital of the analyte and the interfacial electron transfer becomes detectable. The edge potentials, therefore, are inherently sensitive to temperature. An increase in the temperature of the electrode conductive material broadens the energy distribution of the electrons above and the holes below the Fermi energy level. Despite it, the values of $E^{(e)}$ are inherently invariant to most other experimental settings.

Nevertheless, $E^{(e)}$ cannot overlap with, and even approach, $E^{(1/2)}$. Furthermore, from a practical point of view, the capacitance and the ohmic currents affect the baseline of the voltammograms needed for estimating $E^{(e)}$. Overall, $E^{(p)}$ overestimates reduction potentials of oxidation and $E^{(e)}$ underestimates them. Conversely, the values of $E^{(i)}$ and $E^{(p/2)}$ are always between those of $E^{(e)}$ and $E^{(p)}$. It is reasonable to hypothesize, therefore, that $E^{(i)}$ and $E^{(p/2)}$ offer the best readily accessible estimates for $E^{(0)}$ when $E^{(1/2)}$ is not attainable.

The standard electrode potential, $E^{(0)}$, is a fundamental thermodynamic characteristic of a redox couple and as such, its estimated values should be invariant to the experimental

settings. In condensing phase, indeed, the media affects the electronic properties of analytes. The heterogeneous nature of electrochemical processes presents further challenges. How do the electrode material and the composition of the electrolyte solution near the electrode surface affect the solvation energy of the charged components of a redox couple? While extrapolation to zero salt concentration can eliminate the effects of the supporting electrolytes and produce the potentials of the redox couples for neat solvents,[32] it does not compensate for potential "artifacts" that may originate from certain types of working electrodes.

The material of the working and the counter electrodes should be inert. Thus, gold and platinum present good choices for such electrodes, except when the samples contain sulfur at low oxidation states. Thiols and other sulfur compounds have an immense affinity for coinage metals and may affect the recorded voltammograms. Concurrently, gold is a soft metal and routine mechanical chelating may compromise the smoothness of its surface. These challenges with noble metals, in addition to their cost, have made glassy carbon a preferred material for working electrodes for electrochemical analysis.

The morphology of the electrode surface also affects the recorded voltammograms, especially when sharp edges and roughness are essential for the nucleation of a new phase. For example, the overpotential for water reduction on mercury is huge because hydrogen bubbles cannot nucleate easily on their atomically flat surface. Therefore, mercury cathodes can readily reduce Na+ to metal sodium from aqueous solutions to form liquid Na/Hg amalgam. The high solubility of sodium metal in mercury also helps for driving this process. In addition, mercury always exposes new pristine surface when forming a drop. While the Hg susceptibility to oxidation reduces its anodic window, dropping mercury electrode has been an indispensable choice for analyzing reduction processes. Its toxicity, however, has

diminished the enthusiasm for its use. The morphology of electrode surface can control the selectivity of one process over another. Attaching a catalyst to the surface of an electrode offers the best way for attaining specificity of an interfacial process and observe thermodynamic limits of a redox reaction.

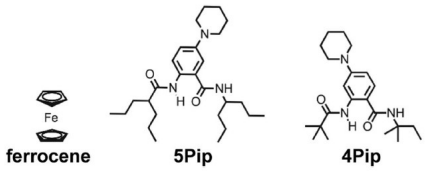

Chart 3-1. Analytes used for this study.

The dynamics of mass transport to and from the electrode surface also affects the recorded voltammograms. Agitating the solvent (e.g., purging with inert gas during data acquisition) and moving the electrode (e.g., using a rotating disc electrode) improves the efficiency of bringing fresh analyte to the electrode surface. It also aids the removal of the electrochemically generated species from the electrode surface and compromises the reversed waves. Therefore, rotating disc electrodes are invaluable for mechanistic studies of the dynamics of interfacial processes employing linear voltammetry, rather than CV. Similarly, using small electrodes (e.g., with area smaller than about 100 μm^2) enhances the edge effects, where the mass transport has multiple directions. Decreasing the working surface of an electrode increases the average mass-transport rates per unit area. Employing working electrodes with such small dimensions at relatively low scan rates, e.g., < 1 V s^{-1}, leads to cyclic voltammograms where the anodic and cathodic waves practically overlap and do not show apparent anodic and cathodic peaks, making it challenging to estimate $E^{(p)}$ and $E^{(1/2)}$. For a working electrode, therefore, we use a glassy carbon electrode with area of 7 mm^2.

Conducting CV measurements is relatively easy, which makes this technique as popular as it is. Setting up the reference electrode, however, can be a potential source for errors. While, for example, pseudo reference electrodes, such as silver wires, have their role in broadening the field,[34–46] they inherently have a range of shortcomings that are beyond the scope of this discussion. Conversely, we employ saturated calomel electrode (SCE) that, when not in use, we store in saturated aqueous solution of KCl. To prevent cross-contamination with the sample, we use a salt bridge for connecting the SCE electrode with the cell. Ideally, the salt bridge should contain the same solution with which the reference electrode is filled. It ensures that the electrolyte composition inside the electrode remains unchanged, and hence, prevents drifts of its potential during extended use.

When the reference electrode is water-based, however, such aqueous salt bridges present two practical issues for organic electrochemical analysis: (1) huge junction potentials between the bridge and the electrolyte solutions of the cell when using low-polarity solvents, such as CHCl3 and CH2Cl2; and (2) water leakage from the bridge into the cell, which may present challenges when the dryness of the organic solution is important for the analysis. The use of a salt bridge that contains electrolyte solution in a moderately polar water-miscible organic solvent, such as acetonitrile and DMF, presents a means for addressing both of those issues. Such a setup splits the huge junction potential into two moderate ones: at the bridge-electrode and the bridge-cell interfaces. Also, leaking an aprotic organic solvent with a wide electrochemical window into the sample solution is a better alternative to leaking water. This setup, however, is not ideal, either. Although it is slow, the diffusion of the component of the organic solution in such bridges across the frit of the reference electrode can cause drifts in the potential during extended use. Therefore, regular monitoring of the performance of the

reference electrode, using samples with well-known potentials, is paramount for electrochemical analysis.

For analysis of reversible oxidation, we focus on ferrocene (Chart 3-1), which is one of the most broadly studied compounds in analytical electrochemistry and its voltammograms manifest pronounced reversibility.[47–50] In voltammetry, therefore, ferrocene has gained popularity as a convenient internal standard and frequently potentials are reported vs. its oxidation.[51–53] As robust as the ferrocene-ferrocenium redox couple is, its use for a reference should be approached with caution. The reduction potential of ferrocenium strongly depends on the solvent polarity and the electrolyte concentration.[32] (According to the accepted convention, $E^{(0)}$ represents the reduction potentials of the oxidized components of redox couples, regardless whether the voltammograms examine the reduction or oxidation propensity of the analyte).[54,55]

To illustrate CV analysis of irreversible and partially reversible oxidation, we focus on electron rich anthranilamide residues that we developed as building blocks for hole-transfer bioinspired molecular electrets.[56–60] Placing an amine on position 5, such as in 5Pip (Chart 3-1), stabilizes the radical cation and leads to reversible electrochemical behavior.[22,25] Moving the amine to position 4, however, e.g., 4Pip (Chart 3-1), causes a positive shift of the anodic wave along with irreversible behavior.[22,25] We demonstrated that eliminating the proton on the C-terminal amide of 4Pip and replacing it with an alkyl group stabilizes the radical cation, $4Pip^{\bullet+}$, leading to voltammograms showing partial reversibility and showing that the amide proton is involved in the oxidative degradation of 4Pip.[22] In this study, we test if the α-protons on the aliphatic chains attached to the two amides are responsible for the

decomposition of $4Pip^{\bullet+}$. Therefore, we use a derivative of 4Pip capped with tertiary alkyl substituents (Chart 3-1).

For a solvent, we employ dry acetonitrile (MeCN) because its moderately high polarity minimizes the dependence of the measured potentials on the electrolyte concentration, C_{el}.[32,33] Nevertheless, we still extrapolate the measured potentials to $C_{el} = 0$ (Figure 3-2), estimating their values for the neat solvent.[32,33] The extrapolated values of $E^{(1/2)}$ for electrolyte-free media relate the electrochemical findings with results from optical studies,[26,32,61] which prove especially invaluable for analyzing systems mediating photoinduced charge transfer.[23,31,62]

The best way to validate the extrapolation of potential values to $C_{el} = 0$ is to test the same analyte with different electrolytes in the same solvent. Furthermore, the extrapolated potentials should be invariant to the sample concentration. For three different supporting electrolytes and ferrocene concentration between 1 and 20 mM, the extrapolation to $C_{el} = 0$ yields values for $E^{(1/2)}$ that are the same within experimental uncertainty (Figure 3-2). This finding validates the extrapolation approach for estimating $E^{(1/2)}$ for neat solvents. Conversely, the trends of $E^{(1/2)}$ vs. C_{el} reveal two features that are important for CV experimental designs. First, an increase in ferrocene concentration increases the standard deviations of the extrapolated potentials (Figure 3-2b). That is, increasing the analyte concentration increases the uncertainty of estimating the potentials for neat solvents, which appears to originate from deviations of the $E^{(1/2)}$ values for small C_{el}. This finding strongly suggests that the concentration of the supporting electrolyte should exceed the concentration of the analyte by at least a factor of 5 or 10.

Second, while lowering the electrolyte concentration converges $E^{(1/2)}$ to the same value, there is a significant difference between the potentials for perchlorate and the other two electrolytes (Figure 3-2a). Also, the values of $E^{(1/2)}$ for LiClO4 show stronger dependence on C_{el} than those for the PF6 and BF4 salts. While increasing the concentration of the supporting electrolyte improves the conductance of electrochemical cells and decreases the ohmic current (i_O), it also changes the dielectric constant of the solvent (ε). About ten years ago, we demonstrated that this variation in the dielectric properties of the media is responsible for the dependence of $E^{(1/2)}$ on C_{el} for electrolytes with bulky polarizable ions, such as N(C4H9)4PF6 and N(C4H9)4BF4.[32] The results for LiClO4 appear to suggest that this salt drastically changes the properties of acetonitrile. Indeed, as a hard Lewis acid, Li+ can affect the structure of solvents such as acetonitrile.[63] Still, it is unlikely for the lithium ions of the electrolyte to increase the dielectric constant of the solution to a large enough extent to induce 100-mV negative shifts of $E^{(1/2)}$ (Figure 3-2a). Considering the Born solvation energy, $E^{(1/2)}$ is proportional to $(1 - \varepsilon^{-1})$.[32,64] For polar media, therefore, variations in ε will have quite smaller effect on ε^{-1} (and on the reduction potentials) than for non-polar solvents.[32,33] Hence, differences in the interactions between the electrolyte ions and the solvent cannot singlehandedly provide an explanation for the observed trends (Figure 3-2a).

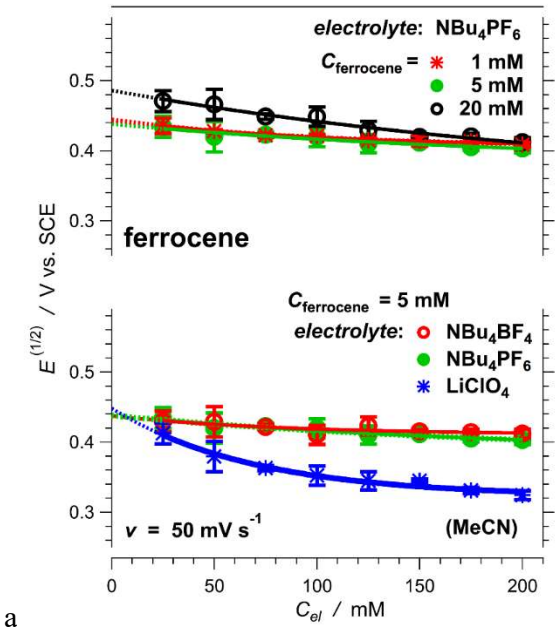

a

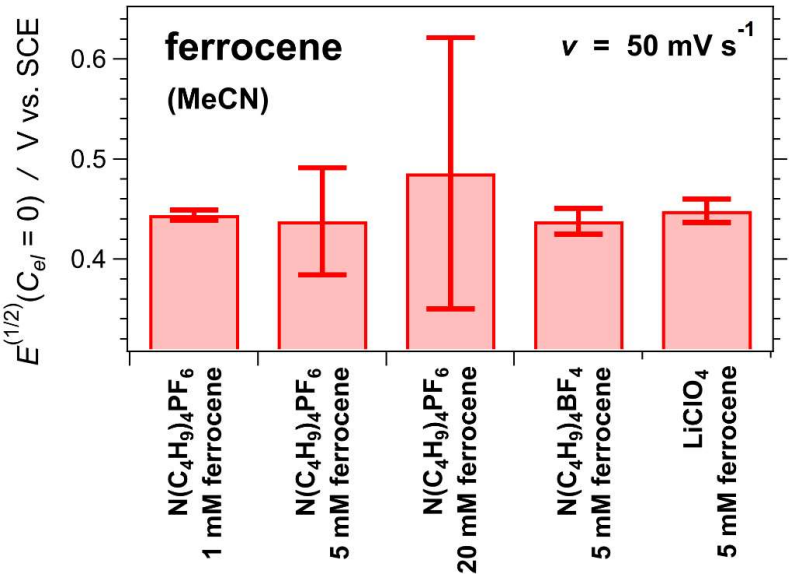

b

Figure 3-2. Extrapolation of the half-wave potentials of ferrocene to zero electrolyte concentration using different electrolytes and different ferrocene concentrations recorded at 50 mV s^{-1}. (a) Dependence of the half-wave potentials on the electrolyte concentration. The solid lines represent the data fits and the dotted lines – extrapolation to zero. (b) Comparison between the half-wave potentials obtained from the extrapolation to zero electrolyte concentration.

Recently, Miller et al. demonstrated the drastic effects that pairing with the ions of the supporting electrolyte can have on electrochemical potentials.[65] The anions of the three electrolytes, PF6–, BF4–and ClO4–, have similar radii and comparable electronic properties.[66] Conversely, N(C4H9)4+ and Li+ are distinctly different. Unlike N(C4H9)4 +, small alkaline ions, such as Li+ and Na+, have a strong propensity for coordination with oxygen-containing ligands, such as water. In organic solvents, which cannot provide such ligation, these cations are often prone to aggregation with the analyte. As an electron-rich compound, ferrocene has nucleophilic properties[67–69] and a propensity for binding alkaline ions,[70] especially Li^+.[71–73]

Binding lithium ions adds positive charges to the complexes with ferrocene and should impede the extraction of electrons. Hence, LiClO4 should cause a positive shift in the reduction potential, which is contrary to what we observe (Figure 3-2a). While electrochemical potentials correlate with the energy levels of the frontier orbitals of the analyte,[74–81] $FE^{(0)}$ and $FE^{(1/2)}$ of the oxidation and reduction do not measure the energies, respectively, of the highest occupied molecular orbitals (HOMOs) and the lowest unoccupied molecular orbitals (LUMOs). That is, the negative $E^{(1/2)}$ shifts, induced by LiClO4 (Figure 3-2a), do not indicate that the electrolyte raises the HOMO energy of ferrocene. Rather, $FE^{(1/2)}$ measures energy differences between the oxidized and the reduced forms of the analyte. Differences between the solvation energies of these two forms further modulate $E^{(1/2)}$. The change in the analyte charge during oxidation or reduction is the principal contribution to these solvation-energy differences.

Therefore, a loss of a lithium ion during the oxidation of Li+- ferrocene complexes can account for the observed trends (Figure 3-2a). In addition to an entropic gain, oxidizing a

Li+-ferrocene complex to a ferrocenium ion conserves the positive charge on the analyte and minimizes the changes in the solvation energy, assuming that the excess number of ClO4 – counterions can readily "assimilate" the released Li+ ions. In this manner, Li+ interaction with ferrocene can improve the ease of its oxidation and lower the reduction potential (Figure 3-2a). Overall, the supporting electrolyte is not necessarily a passive component of the samples. For the rest of the study, we employ N(C4H9)4PF6, and limit the analyte concentration to 1 mM to ensure reliable extrapolation to $C_{el} = 0$.

Results and Discussion

Reversible oxidations are the first we consider. The first and the second derivatives of cyclic voltammograms are immensely instrumental for determining some of the key potentials of the analyte (Figures 3-3a,3b). The zero values of the first derivatives, $\partial i/\partial E = 0$, yield the peak potentials, Ea and Ec, essential for calculating $E^{(1/2)}$, i.e., $E^{(1/2)} = (Ea + Ec) / 2$ (Figure 3-3b). Also, for oxidation, the peak potentials of interest correspond to the anodic peaks, i.e., $E^{(p)} = Ea$. The potentials at which the second derivatives assume zero, $\partial 2i/\partial E2 = 0$, represent the inflection points of the voltammograms and provide a straightforward way for determining $E^{(i)}$ (Figure 3-3b).

The derivatives also reveal a range of subtle details that are not truly apparent in the voltammogram. After all, differentiation eliminates the offset induced by i_C and yields in a constant value for the small linear rise due to i_R (Figures 3-1, 3-3). Visual inspection of the derivatives allows for facile examination of the reversibility. If a process is reversible, the first derivatives of its cyclic voltammograms have axial symmetry across $E = E^{(1/2)}$ with the forward and back sweep crossing at $E^{(1/2)}$ (Figure 3-3c). In addition, reversibility yields

second derivatives that are centrosymmetric around the point on the ordinate corresponding to the half-wave potential, i.e., ($E^{(1/2)}$,^{0}) (Figure 3d). As revealed by their derivatives, all voltammograms of ferrocene manifest reversibility.

The cyclic voltammograms of irreversible oxidation does not show cathodic peaks and cannot provide a means for estimating $E^{(1/2)}$ from E_a and E_c. Therefore, using the characteristic of the anodic waves of reversibly oxidizable ferrocene provides the ideal means for examining which of the potentials have values close to those of $E^{(1/2)}$. In addition to $E^{(i)}$ and $E^{(p)}$, which we estimate from the derivatives of the voltammograms, we also examined $E^{(p/2)}$ and $E^{(e)}$. The half-height peak potential, $E^{(p/2)}$, corresponds to the potential of the rising anodic wave that is in the middle between the peak and the baseline (Figures 3-1, 3-3b). The crossing of the asymptotic lines of the baseline and the rising anodic wave provides the estimates for the edge potentials $E^{(e)}$ (Figures 3-1, 3-3b).

Because $E^{(0)}$ is a fundamental characteristic, it is invariant to experimental parameters, such as scan rate (v). To examine the invariance of the different potentials on the scan rates (Figure 3-4), we resort to a linear regression analysis with a null hypothesis (H^0) that the linear relationship E vs. v has a slope 0. The calculated p-values represent the probability to obtain the measured potentials if H^0 is correct. While such analysis does not validate H^0, it can readily allow rejecting H^0 when p is a small number, i.e., when $p < \alpha$, and $\alpha = 0.01$, 0.05 or 0.1 depending on the selected confidence interval. The immensely small p-values for $E^{(p)}$, $E^{(i)}$ and $E^{(p/2)}$, extracted from voltammograms of samples with different electrolyte concentrations (Table 3-1), clearly show that we can readily reject the H0 for these potentials. We can also reject H^0 for $E^{(e)}$ for $\alpha = 0.05$ or larger. That is, $E^{(p)}$, $E^{(i)}$, $E^{(e)}$ and $E^{(p/2)}$ show dependence on v with 95% confidence (Figure 3-4a). Examining the scan-rate

dependence of the extrapolated potentials for neat solvent reveal the same trends (Figure 3-4b). While the extrapolation increases the uncertainty and the p-values, we can still reject the H0 for $E^{(p)}$, $E^{(i)}$ and $E^{(p/2)}$ with the same confidence of 95% (Table 3-1). The edge potential, $E^{(e)}$, appears to show some invariance to v (Figure 3-4). Despite the relatively small uncertainty (small standard deviations) of its estimates, its p-values are not too small, i.e., $p > 0.01$ for Cel = 100 mM and $p > 0.1$ for a neat solvent. This finding indicates that the inception of the faradaic signal does not have a strong dependence on the scan rate, which is consistent with large electron-transfer rates and with a relatively large amount of analyte adsorbed on the surface of the working electrode.

Because of the lack of invariance with v for most of the potentials, we test how close $E^{(p)}$, $E^{(i)}$, $E^{(p/2)}$ and $E^{(e)}$ are to $E^{(1/2)}$ for each scan rates. We employ Welch's analysis of variance (ANOVA) where H^0 states that the means of the compared potentials are the same, and the p-values represent the probability of obtaining the observed values when H^0 is correct. While small p-values, i.e., $p < \alpha$, permit rejection of H^0, ANOVA does not provide the basis for accepting H^0 when $p > \alpha$.

For data directly obtained from the measured voltammograms, e.g., for C_{el} = 100 mM, we can clearly reject H^0 for $E^{(e)}$ and $E^{(p)}$ with 95% confidence (Table 3-2). That is, the peak potentials and the edge potentials are not a good representation of $E^{(1/2)}$, and of $E^{(0)}$ for that matter. For $E^{(p/2)}$, only v = 200 and 500 mV s^{-1} yield p larger than about 0.05 and we can reject H^0 with 95% confidence for most of the examined scan rates (Table 3-2). Hence, $E^{(p/2)}$ is not a good representation of $E^{(1/2)}$ and of $E^{(0)}$ for small scan rates. The ANOVA tests for the inflection potential, $E^{(i)}$, appear most encouraging. If we adopt a less conservative 90% confidence, we can perhaps reject H^0 only for 10 and 20 mV s^{-1}. With 95% confidence,

however, we cannot truly reject H^0 for any of the scan rates for $E^{(i)}$. While ANOVA does not validate the acceptance of H^0, these findings imply that the inflection potentials provide the best estimates for $E^{(0)}$, when $E^{(1/2)}$ cannot be calculated due to irreversibility, for example. The extrapolation of the different potentials to $C_{el} = 0$ adds uncertainty in their estimates, which affects the outcome of the ANOVA tests. While the trends appear the same, the p-values for the extrapolated potentials are larger than the p-values for those obtained directly from the voltammograms, e.g., for $C_{el} = 100$ mM (Table 3-2). With 95% confidence we can still reject H^0 for the edge potentials even at $C_{el} = 0$, confirming that $E^{(e)}$ does not provide a good estimate for $E^{(0)}$.We cannot reject H^0 for any of the other cases for $C_{el} = 0$, except perhaps for $E^{(p)}$ at 500 mV s^{-1}, assuming 90% confidence (Table II). Overall for oxidation of ferrocene, the inflection potentials, $E^{(i)}$, provides the best estimates for $E^{(0)}$ (Table 3-2). The half-peak potentials, $E^{(p/2)}$, also appear promising for representing $E^{(0)}$, especially for larger scan rates. The peak potentials, $E^{(p)}$, are positively shifted from $E^{(1/2)}$ by 30 to 100 mV (Figure 3-4). With this level of uncertainty, however, the peak potentials, $E^{(p)}$, could be representative of $E^{(1/2)}$ but only for small scan rates. In contrast, for all cases the edge potentials, $E^{(e)}$, underestimate $E^{(1/2)}$ by about 70–80 mV for all scan rates (Figure 3-4), and should not be used for representing $E^{(0)}$.

While $E^{(1/2)}$ and $E^{(e)}$ are invariant to v, an increase in the scan rate causes positive shifts of $E^{(p)}$, $E^{(p/2)}$ and $E^{(i)}$ (Figure 4). These shifts bring the values of $E^{(p)}$ away from $E^{(1/2)}$ and the values of $E^{(i)}$ and $E^{(p/2)}$ closer to $E^{(1/2)}$. While at truly small scan rates, peak potentials can represent $E^{(0)}$ with some uncertainty, the values of $E^{(p)}$ can never overlap with those of $E^{(1/2)}$. Conversely, an increase in the scan rates makes $E^{(i)}$ closely overlap with $E^{(1/2)}$ for v of 100 mV s^{-1} and larger (Figure 3-4). The values of $E^{(p/2)}$ show a similar trend and an overlap

with $E^{(1/2)}$ at 500 mV s^{-1}. For the examined scan rates, however, the half-peak potentials show larger underestimates of $E^{(1/2)}$ than $E^{(i)}$, making the inflection potentials the preferred representation of $E^{(0)}$ when $E^{(1/2)}$ is inaccessible.

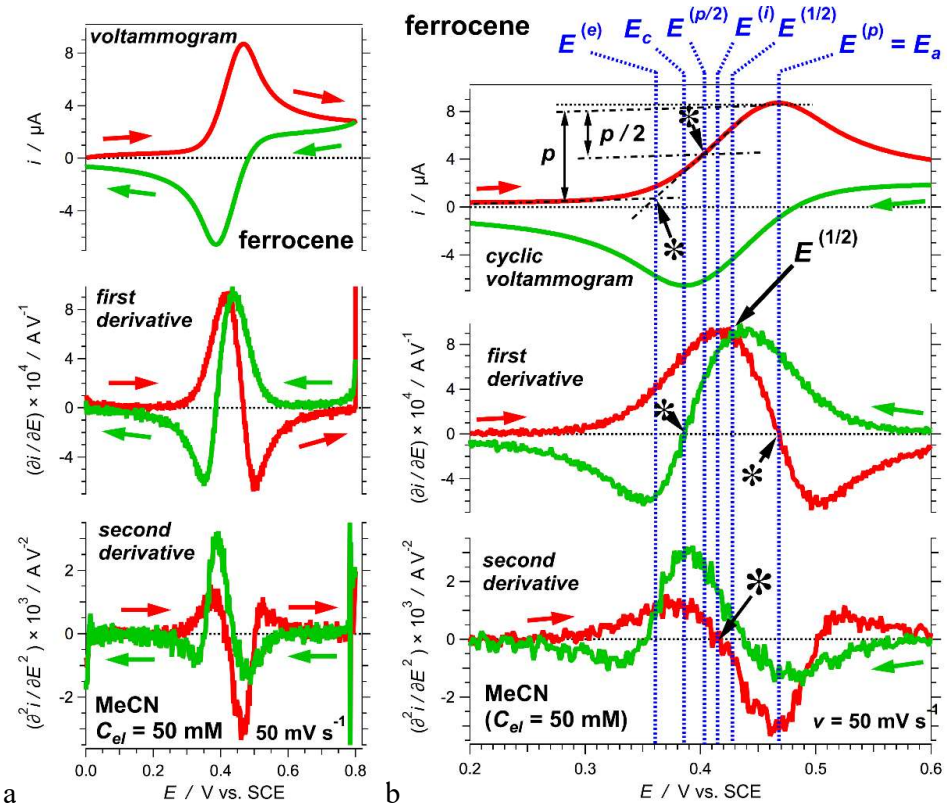

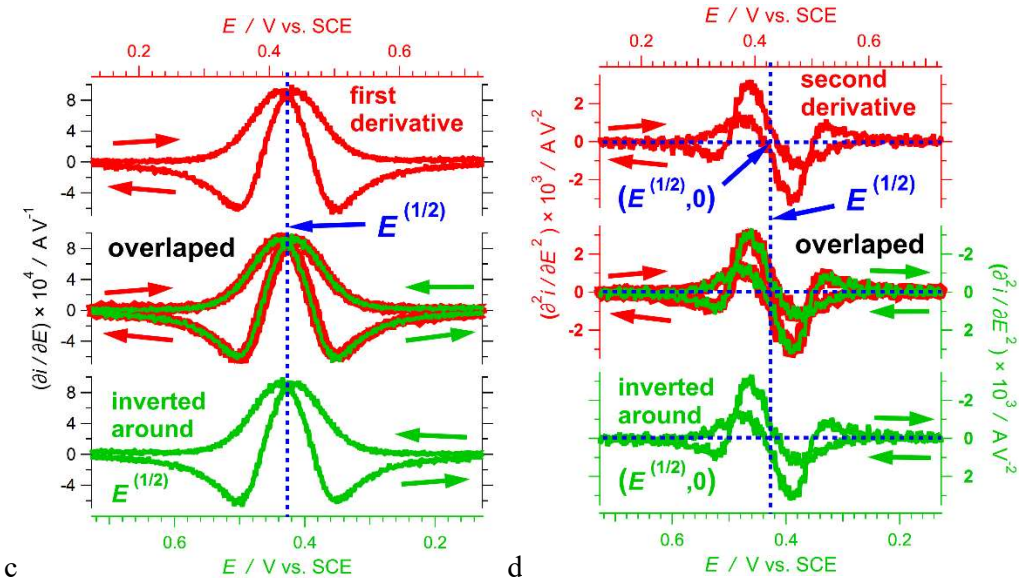

Figure 3-3. Cyclic voltammogram and its derivatives of ferrocene (1 mM), recorded in the presence of 50 mM N(C4H9)4PF6 as a supporting electrolyte at 50 mV s^{-1}. (a) The voltammograms and its first and second derivatives where different colors represent the forward and the back scans as designated by the arrows. (b) Representation of the voltammogram and its derivatives, zoomed on the anodic and the cathodic waves, with designation of the different potentials of interest. (c) Demonstration of the axial symmetry of the first derivative. The derivative (upper curve) and its representation inverted around E = $E^{(1/2)}$ (lower curve) overlap perfectly (middle curves). (d) Demonstration of the centrosymmetric shape of the second derivative. The derivative (upper curve) and its representation inverted around E = $E^{(1/2)}$ and around i = 0 (lower curve) overlap perfectly (middle curves).

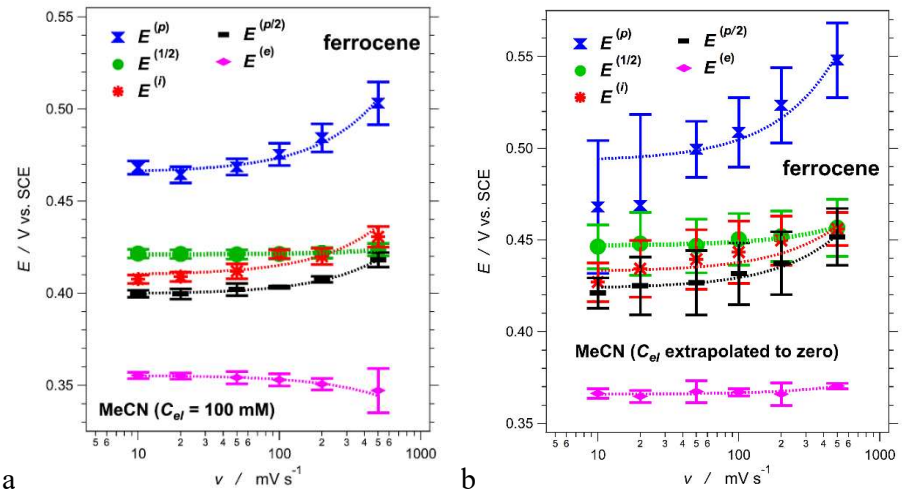

Figure 3-4. Dependence of the different potentials of ferrocene (1 mM) on the scan rate. (a) The potentials are obtained from voltammograms recorded for samples containing 100 mM N(C4H9)4PF6 as a supporting electrolyte. (b) The potentials are obtained from extrapolation to zero electrolyte concentration

When partial irreversibility is not obvious.

Ferroceneferrocenium is an extensively studied well-behaved redox couple and serves as an excellent model for testing concepts and ideas. To further validate and expand the findings from the ferrocene studies, we focus on an electron-rich amidated non-native amino acid, 5Pip (Chart 3-1), the dipole of which can induce significant rectification of charge transfer.[31] The cyclic voltammograms of 5Pip show excellent reversibility in anhydrous media, especially for polarizable solvents, such as CH2Cl2.[22,25] We observe similar behavior of 5Pip for this setup with aqueous salt bridge, but only at high scan rates (Figures 3-5a, 3-5b). At scan rates of 10 and 20 mV s^{-1}, however, the cathodic wave appears smaller than the anodic peak; and an additional small cathodic peak at about 0.3 V vs. SCE becomes apparent (insets of Figures 3-5a, 3-5b).

Table 3-1. p-values from linear regression tests of the dependence of the different potentials on the scan rate. [a]

potential	Ferrocene		5Pip
	C_{el} = 100 mM	C_{el} = 0 mM	C_{el} = 0 mM
$E^{(1/2)}$	0.14	0.27	0.054
$E^{(i)}$	5.1×10^{-6}	0.014	4.2×10^{-4}
$E^{(p/2)}$	2.5×10^{-9}	6.8×10^{-3}	5.6×10^{-4}
$E^{(p)}$	1.7×10^{-7}	3.3×10^{-3}	3.7×10^{-5}
$E^{(e)}$	0.023	0.11	0.20

[a]H^0: The relation E vs. v has a slope 0. Small p-values permit rejection of H^0 and suggest that E depends on v. [b]From extrapolation to zero electrolyte concentration.

The first derivatives of the cyclic voltammograms of 5Pip clearly show a lack of symmetry for small scan rates, which is consistent with deviation from reversibility (Figure 3-6). As the scan rates increase, the first derivatives gradually gain symmetry and the additional cathodic peak at 0.3 V vs. SCE becomes less apparent. At 500 mV s^{-1}, the oxidation is practically reversible, i.e., the first derivative exhibits axial symmetry across $E^{(1/2)}$, and the area of the second cathodic peak drops to less than 5% of the area under the anodic wave. These findings are consistent with degradation of the oxidized analyte, 5Pip•+, within the timescales of acquisition at small scan rates. The timespans between the beginning of the anodic and the completion of the cathodic waves range from about 2 s, for 500 mV s^{-1}, to about 70 s, for 10 mV s^{-1} (Figure 3-6c). Hence, the observed partial reversibility is

consistent with a lifetime of 5Pip•+ that is in the order of 100 s under the conditions of the measurements.

Regardless of the partial irreversibility, the presence of anodic and cathodic peaks allows for estimating the half-wave potentials of 5Pip for different scan rates and electrolyte concentrations. Extrapolation to C_{el} =0 yields similar values of $E^{(1/2)}$ for the different scan rates (Figure 5c). Increasing v from 10 to 500 mV s^{-1} increases $E^{(1/2)}$(Cel = 0) from about 0.73 to 0.75Vvs. SCE (Figure 3-7). The results for $E^{(1/2)}$ at 500mVs^{-1} are the best estimates for $E^{(0)}$ because of the reversibility at this scan rate. Despite the induced irreversibility, decreasing the scan rates by a factor of 50 changes $FE^{(1/2)}$ by less than kBT. This finding has important implications, demonstrating that even for partially reversible behavior, $E^{(1/2)}$ still provides the best estimates for $E^{(0)}$.

The extrapolated potentials for a neat solvents show that $E^{(1/2)}$, $E^{(i)}$ and $E^{(p/2)}$ of 5Pip practically overlap (Figure 3-7), and the ANOVA tests yield large p-values when comparing $E^{(1/2)}$ with $E^{(i)}$ and $E^{(p/2)}$ (Table 3-2). The values of $E^{(p)}$ and $E^{(e)}$ are distinctly separated from $E^{(1/2)}$ (Figure 3-7), and except for 10 mV s^{-1}, all p-values from the ANOVA test comparing $E^{(e)}$ with $E^{(1/2)}$ are smaller than 0.05 (Table 3-2).

While the differences between $E^{(p)}$ with $E^{(1/2)}$ are similar to those between $E^{(e)}$ with $E^{(1/2)}$, the ANOVA p-values for $E^{(p)}$ vs. $E^{(1/2)}$ are quite large due to uncertainty of estimating the peak potentials, which is like what we observe for ferrocene (Table 3-2). While the statistical analysis does not allow the rejection of H0, as an indication that $E^{(p)}$ vs. $E^{(1/2)}$ are significantly different, the large variations in the estimates $E^{(p)}$ (Figures 3-4b, 3-7) renders the peak potentials unattractive for quantification of molecular electronic characteristics.

Table 3-2. p-values from Welch's ANOVA tests comparing $E^{(1/2)}$ with the other potentials.[a]

Sample	C_{el} / mM	v / mV s^{-1}	($E^{(1/2)}$, $E^{(i)}$)	($E^{(1/2)}$, $E^{(p/2)}$)	($E^{(1/2)}$, $E^{(p)}$)	($E^{(1/2)}$, $E^{(e)}$)
Ferrocene	100	10	0.050	0.019	8.2×10^{-3}	1.8×10^{-3}
		20	0.070	0.027	0.013	1.9×10^{-3}
		50	0.19	0.043	0.011	3.9×10^{-3}
		100	0.42	0.022	0.015	3.8×10^{-3}
		200	0.75	0.049	0.017	3.6×10^{-3}
		500	0.40	0.39	0.022	0.022
	0	10	0.35	0.22	0.72	0.022
		20	0.61	0.43	0.73	0.041
		50	0.77	0.47	0.13	0.038
		100	0.78	0.48	0.13	0.028
		200	0.91	0.57	0.10	0.029
		500	0.97	0.84	0.071	0.032

[a]H^0: $E^{(1/2)}$ and E(x) have the same means, where x = i, p/2, p and e. Small p-values permit rejection of H^0 and suggest that $E^{(1/2)}$ and E(x) have different values. [b]From extrapolation to zero electrolyte concentration.

Irreversible behavior

For systems undergoing irreversible oxidation or reduction, $E^{(p)}$ (i.e., Ea or Ec, respectively) is the most frequent choice for representing their electrochemical potentials. This practice has a lot of shortcomings since the peak potentials are immensely sensitive to experimental settings (e.g., scan rate, sample concentration, and electrolyte concentration),

and the inherent properties of the redox couples (e.g., rates of interfacial electron transfer and diffusion). The studies with ferrocene and 5Pip show that inflection and half-peak potentials provide good estimates of $E^{(0)}$, better than the peak potentials. To illustrate how they compare for irreversible oxidation, we choose another electron-rich non-native amino acid derivative, 4Pip (Chart 1), forming a radical cation that is unstable under the CV conditions.[22,25]

In anthranilamide (Aa) residues, moving the amine from 5th to 4th position (i.e., 5Pip vs. 4Pip) makes the oxidation of these derivatives completely irreversible due to a significant change in the spin-density distribution in their radical cations.[22] Extending the positive charge of Aa•+ moieties over their C-terminal amides leads to decomposition. A loss of an amide proton is a possible path for this oxidative degradation. As we showed, derivatizing 4Pip with a tertiary C-terminal amide, i.e., -C(O)N(R2)-, induces partial reversibility.[22] It confirms that the C-terminal amide proton contributes to the instability of 4Pip•+ but is not solely responsible for the oxidative degradation.

Another possibility involves the alkyl α-protons next to the amides. In all Aa derivatives, these α-protons are deshielded, with chemical shifts downfield from those of the rest of the alkyl protons, which may make them labile enough under oxidative conditions. To test it, in this study we capped 4Pip amides with tertiary alkyl chains (Chart 1). For all scan rates and electrolyte concentrations, the cyclic

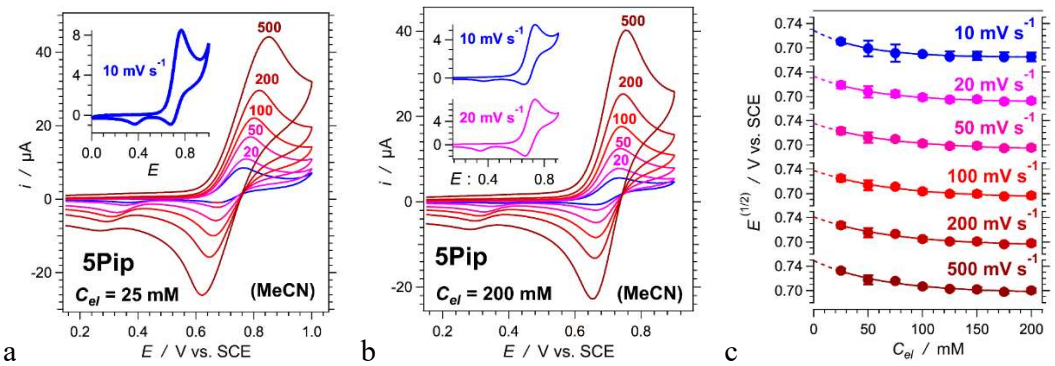

Figure 3-5. Cyclic voltammograms of 5Pip (1 mM) recorded at different scan rates in the presence of different concentrations of N(C4H9)4PF6 as a supporting electrolyte. (a,b) Voltammograms of samples containing 25 and 200 mM electrolyte. (c) Dependence of the half-wave potentials on the electrolyte concentration for the different scan rates. The solid lines represent the data fits and the dotted lines – the extrapolation to zero electrolyte concentration.

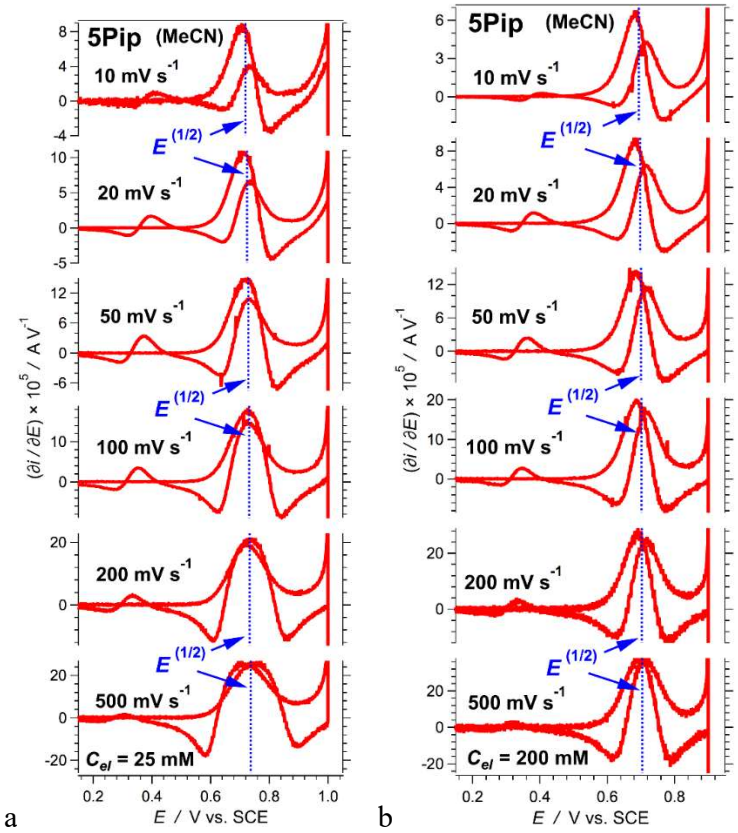

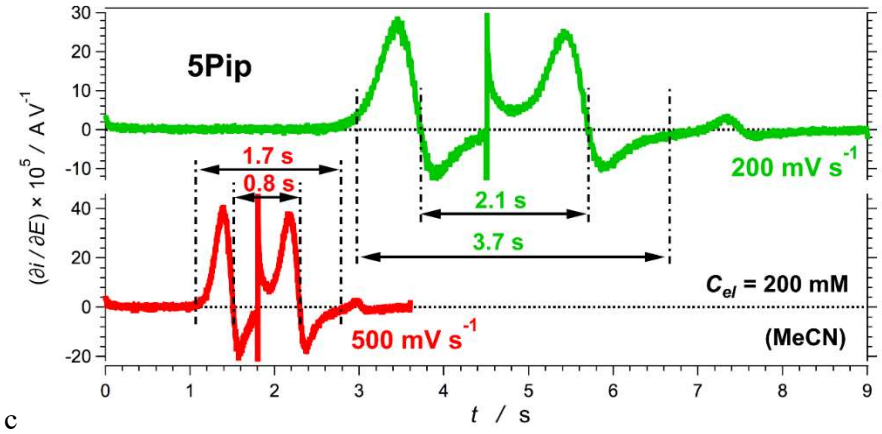

c

Figure 3-6. First derivatives of cyclic voltammograms of 5Pip (1 mM) recorded at different scan rates in the presence of 25 and 200 mM of N(C4H9)4PF6 as a supporting electrolyte. (a,b) the first derivatives. The obtained half-wave potentials are shown. (c) Dependence of the first derivatives on the scanning time showing the durations of data acquisition for different scan rates.

voltammograms of the t-alkyl capped 4Pip show complete irreversibility, with no detectable cathodic peaks. Hence, removal of the α-protons next to the amides does not stabilize the radical cation of 4Pip for the timescales of the CV data acquisition. The first and second derivatives of the cyclic voltammograms of the irreversible oxidation of 4Pip do not show symmetric features (Figure 3-8a). The derivatives of the anodic wave of 4Pip appear the same as those of ferrocene and 5Pip. It is, however, the derivatives of the cathodic waves that discern irreversible from reversible oxidation (Figures 3-3, 3-6, 3-8a).

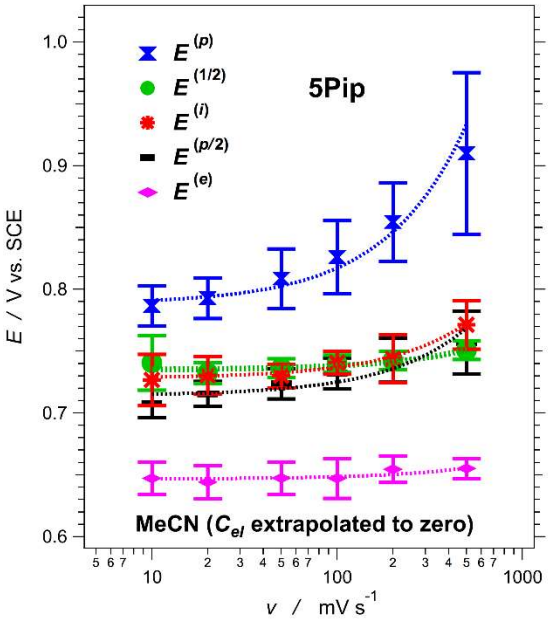

Figure 3-7. Dependence of the different potentials of 5Pip (1 mM) on the scan rate. The potentials are obtained from extrapolation to zero concentration of N(C4H9)4PF6 (Figure 3-5c).

Because the anodic waves of the voltammograms and their derivatives are quite similar for analytes undergoing reversible and irreversible oxidation, we can reliably use them for estimating $E^{(i)}$, $E^{(p/2)}$ and $E^{(e)}$, in addition to $E^{(p)}$ (Figure 3-8a), and extrapolate them to zero electrolyte concentration. Similar to 5Pip, the scan-rate dependence of the extrapolated potentials of 4Pip show clustering of the values for $E^{(i)}$ and $E^{(p/2)}$. Conversely, $E^{(e)}$ and $E^{(p)}$ are well separated from $E^{(i)}$ and $E^{(p/2)}$ (Figure 3-8b).

As the scan rates vary from 10 to 500 mV s^{-1}, $E^{(p)}$ of 4Pip increases with 150 mV, while $E^{(i)}$ and $E^{(p/2)}$ increase with about 80 mV (Figure 3-8b). For 4Pip, this increase in the potentials is predominantly at the small scan rates. Hence, between 100 and 500 mV s^{-1}, $E^{(i)}$ and $E^{(p/2)}$ of 4Pip vary within about 40 mV (i.e., less than 2kBT), while the $E^{(p)}$ of 4Pip varies

over 100 mV (Figures 8b). Considering that reversible oxidation results in the best overlap of $E^{(1/2)}$ with $E^{(i)}$ and $E^{(p/2)}$ at scan rates between 100 and 500 mV s^{-1} (Figures 3-4, 3-7), which is the range where $E^{(i)}$ and $E^{(p/2)}$ of 4Pip show the smallest dependence on v, makes the inflection and half-peak potentials the best estimate for $E^{(0)}$ of the irreversibly behaving systems, 4Pip.

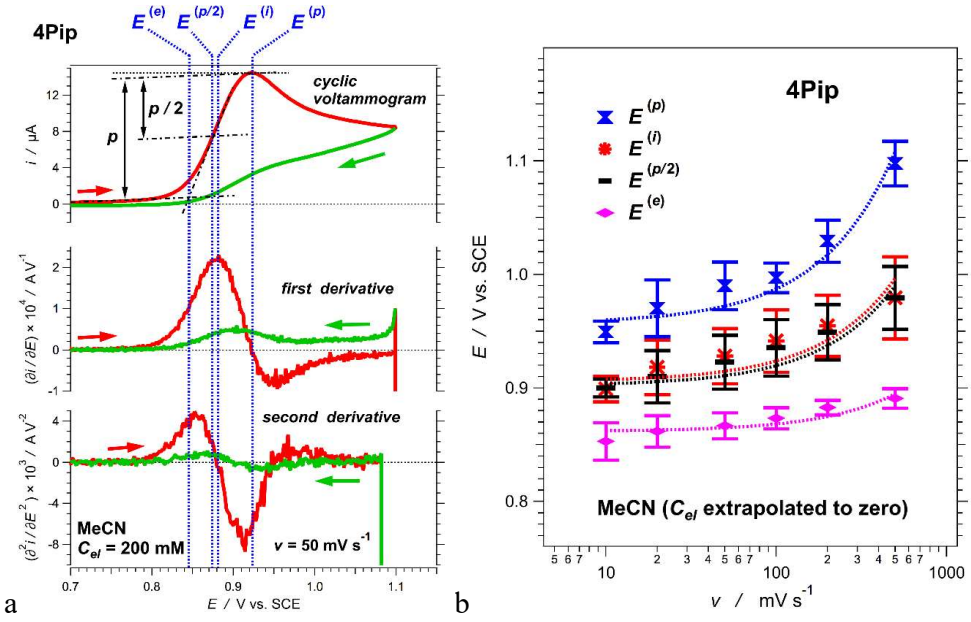

Figure 3-8. Electrochemical properties of 4Pip. (a) Cyclic voltammogram, along with its first and second derivative, of 4Pip (1mM) recorded at 50mVs^{-1} in the presence of 200 mM N(C4H9)4PF6. The different potentials obtainable from the anodic wave are designated. (b) Dependence of the different potentials of 4Pip on the scan rate. The potentials are obtained from extrapolation to zero concentration of N(C4H9)4PF6.

Pros and cons of inflection potentials

Our studies reveal that inflection potentials present the best estimates for $E^{(0)}$ from voltammograms showing irreversible behavior. Overall, differential analysis (needed for determining $E^{(i)}$) has the power to reveal subtle features of voltammograms (Figures 3-3, 3-6, 3-8). This property of differential analysis, however, is also responsible for amplifying the inherent experimental noise. While lowering the analyte concentration is essential for reliability of the recorded voltametric data (Figure 3-2a), it also decreases the signal-to-noise ratios. To address this challenge, we subject the first-derivatives curves to smoothing prior to the second numerical differentiation, as stated in the Experimental section. Limiting the span

of shape smoothing to about 25 data points (at 1 mV per a data-point increment) ensures that the uncertainties in the obtained values for the potentials at the curve extrema are considerably smaller that the thermal energy, i.e., << FkBT.

The differential nature of the analysis producing $E^{(i)}$, provides its most important advantage over $E^{(p/2)}$. The half-peak potential, $E^{(p/2)}$, depends only on three points: the baseline current, the peak current and the potential on the curve at the midpoint between these currents. Thus, $E^{(p/2)}$ cannot account for complex shapes of voltammogram waves. Conversely, differential analysis can reveal shoulders and overlapping waves, producing multiple inflection points. This feature can prove invaluable for the analysis of: (1) multi-electron processes; and (2) samples comprising a mixture of conformers or aggregates exhibiting close, but different, reduction potentials. For example, when the potentials of two sequential electron-transfer steps are relatively close, the voltammogram waves can appear broad but they cannot be discerned from those of single-step multi-electron processes.[13,15]

Increasing the difference between the potentials of sequential reduction or oxidation steps, first broadens the waves, then leads to the appearance of a shoulder and finally results in two distinct peaks. Differential analysis can prove invaluable for analysis of such complex shapes and allow for selective evaluation of $E^{(i)}$ of the first step, for example.

In addition to the scan rates and other experimental settings, the shapes of voltammograms depends on: (1) the rates of interfacial electron transfer, characterized with $k^{(0)}$; (2) the rates of diffusion of the reduced and oxidized forms of the analyte, Dred and Dox; (3) the charge transfer coefficient, α; and (4) the rates of degradation or other chemical transformation that depletes the electrochemically formed species, as characterized with k,

for example. Different $k^{(0)}$, k, Dox, Dred, and α result in voltammograms with different shapes where $E^{(p)}$ varies the most.11 While $E^{(e)}$ and $E^{(i)}$ appear to be least susceptible to these multiparameter variations, $E^{(e)}$ inherently always underestimates and overestimates $E^{(0)}$ of oxidation and reduction, respectively. Therefore, $E^{(i)}$ is the closest estimate of $E^{(0)}$ that is easy to obtained from voltammograms manifesting irreversible behavior.

Conclusions

The half-wave potential, which are readily obtainable from cyclic voltammograms, are by far the best representation for $E^{(0)}$ even in cases manifesting partial irreversibility due to slow decomposition of the produced species. Conversely, all evidence suggest that when $E^{(1/2)}$ is not attainable due to complete chemical irreversibility, the inflection potentials and the half-peak potentials provide the best estimates for $E^{(0)}$, for moderate scan rates, e.g., 100 – 500 mV s^{-1}. While in many cases $E^{(i)}$ and $E^{(p/2)}$ perform almost the same, the values of $E^{(i)}$ tend to be inherently closer to $E^{(1/2)}$ than those of $E^{(p/2)}$. This report provides an important foundation and key evidence for transforming widely accepted practices of analyzing electrochemical findings in order to improve and broaden their utility.

Supporting information

Materials and general synthetic considerations.—All reagents and solvents were purchased from TCI America, Sigma-Aldrich and Alfa Aesar and used as received. The reaction progress was monitored by the means of thin layer chromatography (TLC), which was performed with aluminum foil plates, covered with silica gel 60 F254 (Merck). The products were purified using column chromatography packed with Kieselgel 60 (Merck). All reported 1H-NMR and 13CNMR spectra were recorded on a 600 MHz spectrometer. Chemical shifts

(δ/ppm) were determined using the solvent peaks as internal references. High-resolution mass spectra were obtained using electrospray MS (ESI-MS). 2-nitro-N-(tert-pentyl)-4-(piperidin-1-yl)benzamide (1).—2- Nitro-4-(piperidin-N-yl)-benzoic acid (1.0 g, 4 mmol), prepared as previously described,30 was placed in a 100 mL Schlenk tube equipped with a magnetic stir bar. While purging with argon, chloro-N,N,N,N- tetramethylformamidinium hexafluorophosphate (2.0 g, 6 mmol) and 5 mL of dry dichloromethane (DCM) were added. The Schlenk tube was immersed in a dry ice/acetone bath and 2-methylbutan-2-amine (940 μL, 8 mmol) was slowly added to it followed by the addition of N-methylmorpholine (1.5 mL, 14 mmol). The reaction mixture was allowed to warm up to room temperature and was stirred overnight. The solution was diluted with 25 mL of DCM, and washed with 5% HCL (2 × 100 mL) and with a brine solution (100 mL). The organic layer was collected, dried over Na2SO4, and concentrated in vacuo.

The product was purified using flash chromatography (column: 1” internal diameter, packed with silica gel in hexanes, 6” to 8” height of the packed stationary phase). The purification (stationary phase: silica gel; eluent gradient: from 100% hexanes to 100% ethyl acetate) afforded 1.01 g (3.17 mmol, 79% yield) of a yellow solid of 1. 1H NMR (600 MHz, CDCl3) δ/ppm: 7.34 (1 H, d, J = 2.56 Hz), 7.30 (1 H, d, J = 8.70 Hz), 7.00 (1 H, d, J = 7.68 Hz), 5.43 (1 H, s), 3.27 (4 H, m), 1.79 (2 H, q, J = 7.68 Hz), 1.67 (4 H, m), 1.62 (2H, m), 1.37 (s, 1 H), 0.91 (3 H, t, J = 7.42 Hz). 13C NMR (150 MHz, CDCl3) δ/ppm: 165.87, 152.15, 148.25, 129.42, 122.43, 118.32, 109.84, 54.61, 49.22, 32.87, 26.19, 25.09, 24.00, 8.34. HRMS (m/z, ESI-TOF): calcd. for C17H26N3O3+, 320.1974 [M + H]+; found, 320.1956. N-(tert-pentyl)-4-(piperidin-1-yl)-2-(2-propylpentanamido) benzamide (4Pip).—510 mg of 1 (1.6 mmol) and dicobalt octacarbonyl (1.1 g, 3.2 mmol) were placed in a 100 mL Schlenk

tube equipped with a magnetic stir bar. While purging with argon, 5 mL of 1,2-dimethoxyethane and 2 drops of DI water were added. While stirring, the pressure tube was immersed in a temperature-controlled oil bath. The mixture was heated to 90◦C and stirred for an hour. The reaction mixture was filtered; the filtrate was collected, diluted with 25 mL DCM, and washed with water (100 mL). The organic layer was collected, dried over Na2SO4, and concentrated in vacuo. The formed amine was used for the next step without further purification. While purging with argon, the resulting organic solid was transferred into a Schlenk tube using 5 mL dry DCM. The Schlenk tube was immersed in a dry ice/acetone bath, allowed to cool down, followed by addition of pivaloyl chloride (500 μL, 4 mmol) and N-methylmorpholine (750 μL, 6.8 mmol). The reaction mixture was allowed to warm up to room temperature and was stirred overnight. The solution was diluted with 25 mL of DCM, and washed with 5% HCL (2 × 100 mL) and with a brine solution (100 mL). The organic layer was collected, dried over Na2SO4, and concentrated in vacuo. The product was purified using flash chromatography (column: 1” internal diameter, was packed with silica gel in hexanes, 6” to 8” height of the packed stationary phase). The purification (stationary phase: silica gel: eluent gradient: from 100% hexanes to 100% ethyl acetate) afforded 435 mg, (1.2 mmol, 73% yield) of 4Pip. 1H NMR (600 MHz, CDCl3) δ/ppm: 11.51 (1 H, s), 8.29 (1 H, s), 7.21 (1 H, m), 6.47 (1 H, s), 5.68 (1 H, s), 3.27 (4 H, s), 1.80 (2 H, q, J = 7.17 Hz), 1.63 (4 H, s), 1.58 (2 H, s), 1.36 (6 H, s), 1.29 (10 H, s), 0.86 (3 H, t, J = 7.42 Hz). 13C NMR (150 MHz, CDCl3) δ/ppm: 178.04, 168.99, 153.96, 141.31, 127.35, 111.18, 108.33, 106.54, 54.38, 48.94, 40.18, 32.72, 27.59, 26.52, 25.38, 24.30, 8.39. HRMS (m/z, ESI-TOF): calcd. For C22H36N3O3 +, 390.2757 [M + H]+; found, 374.2814. 2-nitro-N-(tert-pentyl)-5-(piperidin-1-yl)benzamide (2).—2- Nitro-5-(piperidin-N-yl)-benzoic acid (530 mg, 2.12 mmol),

prepared as previously described,31 was placed in a baked 50 mL round bottom flask equipped with a magnetic stir bar. While purging with argon, chloro-N,N,N,N-tetramethylformamidinium hexafluorophosphate (890 mg, 3.2 mmol) and 1,2-dichloroethane (5 mL) were added, and the reaction was cooled down in a dry ice/acetone bath.

While stirring, 4-heptylamine (380 μL, 2.5 mmol) and 1 mL triethylamine (7.2 mmol) were slowly added. The reaction mixture was allowed to warm up to room temperature and was stirred overnight at 60◦C.

The solution was diluted with 25 mL of DCM, and washed with 5% HCL (2 × 100 mL) and with brine (100 mL). The organic layer was collected, dried over Na2SO4, and concentrated in vacuo. The product was purified using flash chromatography (column, 1 internal diameter, packed with silica gel in hexanes, 6” to 8” height of the packed stationary phase). The purification (stationary phase: silica gel; eluent gradient: from 100% hexanes to 100% ethyl acetate) afforded 330 mg (0.95 mmol, 45% yield) of a yellow solid of 2. 1H NMR (600 MHz, CDCl3) δ/ppm: 8.02 (1 H, d, J = 9.2 Hz), 6.77 (1 H, dd, J = 9.5, 2.8 Hz), 6.68 (1 H, d, J = 3.1 Hz), 5.39 (1 H, d, J = 9.2 Hz), 4.1 (1 H, m), 3.41 (4 H, m), 1.67 (6 H, m), 1.53 (2 H, m), 1.43 (6 H, m), 0.94 (6 H, t, J = 7.2 Hz). 13C NMR (150 MHz, CDCl3) δ/ppm: 167.43, 153.88, 136.47, 134.04, 127.43, 112.82, 112.16, 49.61, 48.43, 36.91, 25.18, 24.05, 19.03, 14.11. HRMS (m/z, ESI-TOF): calcd. for C19H30N3O3+, 348.2287 [M + H]+; found, 348.1938.

N-(heptan-4-yl)-5-(piperidin-1-yl)-2-(2-propylpentanamido) benzamide (5Pip).—290 of 2 (0.84 mmol) was suspended in ethyl acetate with 60 mg Pd/C (10%) in a 50 mL round bottom flask equipped with a magnetic stir bar. The mixture was stirred overnight under a

hydrogen atmosphere at room temperature. The completion of the reduction led to a color change from yellow to colorless and appearance of blue fluorescence, which was monitored using TLC. The catalyst on the support was filtered out and the ethyl acetate was removed in vacuo. The solid was resuspended in 1,2-drichloroethane (5 mL), blanked with continuous flow of Ar and placed in a dry ice/acetone bath. Concurrently, 2-propylpentanoic acid (160 uL, 1mmol) was converted to its acyl chloride form by treatment with oxalyl chloride in a flask immersed in dry ice/acetone bath. The thus obtained 2-propylpentanoyl chloride was added to the amine solution dropwise followed by a dropwise addition of triethylamine (1 mL, 7.2 mmol). The reaction mixture was allowed to warm up to room temperature and was stirred overnight at 60◦C. The solution was diluted with 25 mL of DCM, and washed with 5% HCL (2 ×100 mL) and with brine (100 mL). The organic layer was collected, dried over Na2SO4, and concentrated in vacuo. The product was purified using flash chromatography (column, 1" internal diameter, was packed with silica gel in hexanes, 6" to 8" height of the packed stationary phase). The purification (stationary phase: silica gel: eluent gradient: from 100% hexanes to 100% ethyl acetate) afforded 110 mg (0.25 mmol, 30% yield) of 5Pip. 1H NMR (600 MHz, CDCl3) δ/ppm: 10.45 (1 H, s), 8.36 (1 H, d, J = 9.2 Hz), 7.02 (2 H, m), 5.0 (1 H, J = 9.2 Hz), 4.09 (1 H, m), 3.04 (4 H, m), 2.22 (1 H, dt, J =9.2, 4.6 Hz), 1.71 (4 H, dt, J = 11, 5.8 Hz), 1.63 (2 H, m), 1.53 (4 H, m), 1.34 (12 H, m), 0.9 (6 H, p, J = 7.2 Hz), 0.86 (6H, m). 13C NMR (150 MHz, CDCl3) δ/ppm: 174.70, 168.83, 147.45, 131.84, 123.04, 122.77, 120.72, 115.54, 51.91, 49.22, 49.00, 37.50, 35.40, 25.66, 23.82, 20.74, 19.20, 14.08, 13.97. HRMS (m/z, ESI-TOF): calcd. For C27H46N3O2+, 444.3590 [M + H]+; found, 444.3692.

References

1. C. Costentin, J.-M. Saveant, and C. Tard, *ACS Energy Lett*., **3**, 695 (2018).

2. N. Arshad and S. I. Farooqi, *Appl. Biochem. Biotechnol.*, **186**, 1090 (2018).

3. J. B. Derr, J. Tamayo, E. M. Espinoza, J. A. Clark, and V. I. Vullev, *Can. J. Chem.*, **96**, 843 (2018).

4. A. J. Wierzba, A. Wincenciuk, M. Karczewski, V. I. Vullev, and D. Gryko, *Chem. Eur. J.*, **24**, 10344 (2018).

5. N. T. Rodeberg, S. G. Sandberg, J. A. Johnson, P. E. M. Phillips, and R. M. Wightman, *ACS Chem. Neurosci.*, **8**, 221 (2017).

6. F. Harnisch and S. Freguia, *Chem. Asian J.*, **7**, 466 (2012).

7. I. Hwang and K. Yong, *ChemElectroChem*, **2**, 634 (2015).

8. S. Gupta, M. R. Chatni, A. L. N. Rao, V. I. Vullev, L. V. Wang, and B. Anvari, *Nanoscale*, **5**, 1772 (2013).

9. C. E. Nebel, B. Rezek, D. Shin, and H.Watanabe, *Physica Status Solidi A*, **203**, 3273 (2006).

10. N. Armaroli, G. Accorsi, F. Song, A. Palkar, L. Echegoyen, D. Bonifazi, and F. Diederich, *ChemPhysChem*, **6**, 732 (2005).

11. D. A. C. Brownson et al., “Interpreting Electrochemistry” in *The Handbook of Graphene Electrochemistry*, D. A. C. Brownson and C. E. Banks Editors, p. 23,

Springer-Verlag London Ltd. (2014).

12. B. J. Adesokan, X. Quan, A. Evgrafov, A. Heiskanen, A. Boisen, andM. P. Soerensen, *J. Electroanal. Chem.*, **763**, 141 (2016).

13. N. Elgrishi, K. J. Rountree, B. D. McCarthy, E. S. Rountree, T. T. Eisenhart, and J. L. Dempsey, *J. Chem. Educ.*, **95**, 197 (2018).

14. N. V. Rees and R. G. Compton, *Chem. Commun.*, **46**, 4238 (2010).

15. D. H. Evans, *Chem. Rev.*, **108**, 2113 (2008).

16. J. A. V. Butler, *Trans. Faraday Soc.*, **19**, 734 (1924).

17. T. Erdey-Gruz and M. Volmer, *Z. Physik. Chem.*, **150**, 203 (1930).

18. R. A. Marcus, *Angew. Chem. lnr. Ed. Engl.*, **32**, 1111 (1993).

19. C. Batchelor-McAuley, E. Kaetelhoen, E. O. Barnes, R. G. Compton, E. Laborda, and A. Molina, *ChemistryOpen*, **4**, 224 (2015).

20. E. Laborda, M. C. Henstridge, C. Batchelor-McAuley, and R. G. Compton, *Chem. Soc. Rev.*, **42**, 4894 (2013).

21. R. M. Wightman, M. R. Deakin, P. M. Kovach, W. G. Kuhr, and K. J. Stutts, *J. Electrochem. Soc.*, **131**, 1578 (1984).

22. E. M. Espinoza, J. M. Larsen, and V. I. Vullev, *J. Phys. Chem. Lett.*, **7**, 758 (2016).

23. A. Purc, E. M. Espinoza, R. Nazir, J. J. Romero, K. Skonieczny, A. Je˙zewski, J. M. Larsen, D. T. Gryko, and V. I. Vullev, *J. Am. Chem. Soc.*, **138**, 12826 (2016).

24. E. M. Espinoza, J. M. Larsen-Clinton,M. Krzeszewski, N. Darabedian, G. D. T., and V. I. Vullev, *Pure Appl. Chem.*,**89**, 1777 (2017).

25. J. M. Larsen-Clinton, E. M. Espinoza, M. F. Mayther, J. Clark, C. Tao, D. Bao, C. M. Larino, M. Wurch, S. Lara, and V. I. Vullev, *Phys. Chem. Chem. Phys.*, **19**, 7871 (2017).

26. E. M. Espinoza, J. A. Clark, J. B. Derr, D. Bao, B. Georgieva, F. H. Quina, and V. I. Vullev, *ACS Omega*, **3**, 12857 (2018).

27. H. G. Ryu, M. F. Mayther, J. Tamayo, C. Azarias, E. M. Espinoza, M. Banasiewicz, L. G. Lukasiewicz, Y. M. Poronik, A. Jezewski, J. Clark, J. B. Derr, K. H. Ahn, D. T. Gryko, D. Jacquemin, and V. I. Vullev, *J. Phys. Chem. C*, **122**, 13424 (2018).

28. H. G. Roth, N. A. Romero, and D. A. Nicewicz, *Synlett*, **27**, 714 (2016).

29. M. S. Thomas, V. Nu˜nez, S. Upadhyayula, E. R. Zielins, D. Bao, J. M. Vasquez, B. Bahmani, and V. I. Vullev, *Langmuir*, **26**, 9756 (2010).

30. J. M. Larsen, E. M. Espinoza, J. D. Hartman, C.-K. Lin, M. Wurch, P. Maheshwari, R. K. Kaushal, M. J. Marsella, G. J. O. Beran, and V. I. Vullev, *Pure Appl. Chem.*, **87**, 779 (2015).

31. D. Bao, S. Upadhyayula, J. M. Larsen, B. Xia, B. Georgieva, V. Nunez,

E. M. Espinoza, J. D. Hartman, M.Wurch,A.Chang,C.-K. Lin, J.Larkin,K.Vasquez, G. J. O. Beran, and V. I. Vullev, *J. Am. Chem. Soc.*, **136**, 12966 (2014).

32. D. Bao, B. Millare, W. Xia, B. G. Steyer, A. A. Gerasimenko, A. Ferreira, A. Contreras, and V. I. Vullev, *J. Phys. Chem. A*, **113**, 1259 (2009).

33. D. Bao, S. Ramu, A. Contreras, S. Upadhyayula, J. M. Vasquez, G. Beran, and V. I. Vullev, *J. Phys. Chem. B*, **114**, 14467 (2010).

34. E. T. S. G. da Silva, S. Miserere, L. T. Kubota, and A. Merkoci, *Anal. Chem.*, **86**, 10531 (2014).

35. A. A. G. F. Beati, R. M. Reis, R. S. Rocha, and M. R. V. Lanza, *Industr. Eng. Chem. Res.*, **51**, 5367 (2012).

36. M. Abdul Aziz, B.-K. Kim, M. Kim, S.-Y. Yang, H.-W. Lee, S. W. Han, Y. I. Kim, S. Jon, and H. Yang, *Electroanalysis*, **23**, 2042 (2011).

37. G. Jones II, X. Zhou, and V. I. Vullev, *Photochem. Photobiol. Sci.*, **2**, 1080 (2003).

38. M. Diaz-Gonzalez, C. Fernandez-Sanchez, and A. Costa-Garcia, *Electroanalysis*, **14**, 665 (2002).

39. G. Jones II and V. I. Vullev, *Org. Lett.*, **4**, 4001 (2002).

40. P. Hrncirova and F. Opekar, *Sens. Actuat. B*, **81**, 329 (2002).

41. V. I. Vullev and G. Jones, *Tetrahedr. Lett.*, **43**, 8611 (2002).

42. D. K. Lee, H. J. Lee, G. S. Cha, H. Nam, and K. J. Paeng, *J. Chromatogr. A*, **902**, 337 (2000).

43. G. Jones II, V. Vullev, E. H. Braswell, and D. Zhu, *J. Am. Chem. Soc.*, **122**, 388 (2000).

44. S. Taunier, C. Guery, and J. M. Tarascon, *Electrochim. Acta*, **44**, 3219 (1999).

45. C. D. T. Bratten, P. H. Cobbold, and J. M. Cooper, *Anal. Chem.*, **69**, 253 (1997).

46. G. Jones II, L. N. Lu, V. Vullev, D. Gosztola, S. Greenfield, and M. Wasielewski, *Bioorg. Med. Chem. Lett.*, **5**, 2385 (1995).

47. E. Halls Jonathan, A. Hernan-Gomez, D. Burrows Andrew, and F. Marken, *Dalton Transact*., **41**, 1475 (2012).*Journal of The Electrochemical Society*, **166** (5) H3175-H3187 (2019) H3187

48. Zheng, Evans, and Nelsen, *J. Org. Chem.*, **65**, 1793 (2000).

49. B. Bry and B. Tremillon, *J. Electroanal. Chem. Interfac. Electrochem.*, **46**, 71 (1973).

50. S. P. Gubin, S. A. Smirnova, L. I. Denisovich, and A. A. Lubovich, *J. Organometal. Chem.*, **30**, 243 (1971).

51. A. M. Bond, K. B. Oldham, and G. A. Snook, *Anal. Chem.*, **72**, 3492 (2000).

52. A. M. Bond, E. A. McLennan, R. S. Stojanovic, and F. G. Thomas, *Anal. Chem.*, **59**, 2853 (1987).

53. R. R. Gagne, C. A. Koval, and G. C. Lisensky, *Inorg. Chem.*, **19**, 2854 (1980).

54. S. Trasatti, *Pure Appl. Chem.*, **58**, 955 (1986).

55. W. M. Latimer, *J. Am. Chem. Soc.*, **76**, 1200 (1954).

56. J. M. Larsen, E. M. Espinoza, and V. I. Vullev, *J. Photon. Energy.*, **5**, 055598 (2015).

57. M. K. Ashraf, R. R. Pandey, R. K. Lake, B.Millare, A. A. Gerasimenko, D. Bao, and V. I. Vullev, *Biotechnol. Progr.*, **25**, 915 (2009).

58. V. I. Vullev, *J. Phys. Chem. Lett.*, **2**, 503 (2011).

59. B. Xia, D. Bao, S. Upadhyayula, G. Jones, and V. I. Vullev, *J. Org. Chem.*, **78**, 1994 (2013).

60. S. Upadhyayula, D. Bao, B. Millare, S. S. Sylvia, K. M. M. Habib, K. Ashraf, A. Ferreira, S. Bishop, R. Bonderer, S. Baqai, X. Jing, M. Penchev, M. Ozkan, C. S. Ozkan, R. K. Lake, and V. I. Vullev, *J. Phys. Chem. B*, **115**, 9473 (2011).

61. E. M. Espinoza, B. Xia, N. Darabedian, J. M. Larsen, V. Nunez, D. Bao, J. T. Mac, F. Botero,M.Wurch, F. Zhou, and V. I. Vullev, *Eur. J. Org. Chem.*, **2016**, 343 (2016).

62. M. Krzeszewski, E. M. Espinoza, C. Cervinka, J. B. Derr, J. A. Clark, D. Borchardt, G. J. O. Beran, D. T. Gryko, and V. I. Vullev, *Angew. Chem., Int. Ed.*, **57**, 12365 (2018).

63. O. Borodin, S.-D. Han, J. S. Daubert, D. M. Seo, S.-H. Yun, and W. A. Henderson, *J. Electrochem. Soc.*, **162**, A501 (2015).

64. M. Born, *Z. Phys.*, **1**, 45 (1920).

65. M. J. Bird, T. Iyoda, N. Bonura, J. Bakalis, A. J. Ledbetter, and J. R. Miller, *J. Electroanal. Chem.*, **804**, 107 (2017).

66. T. Kakiuchi, J. Noguchi, and M. Senda, *J. Electroanal. Chem.*, **327**, 63 (1992).

67. M. Rosenblum, J. O. Santer, andW. G. Howells, *J. Am. Chem. Soc.*, **85**, 1450 (1963).

68. A. F. Cunningham Jr., *J. Am. Chem. Soc.*, **113**, 4864 (1991).

69. M. J. Mayor-Lopez, J. Weber, B. Mannfors, and A. F. Cunningham Jr., *Organometallics*, **17**, 4983 (1998).

70. A. H. Ilkhechi, J. M. Mercero, I. Silanes, M. Bolte, M. Scheibitz, H.-W. Lerner, J. M. Ugalde, and M. Wagner, *J. Am. Chem. Soc.*, **127**, 10656 (2005).

71. J. Rodr´ıguez-Otero, E. M. Cabaleiro-Lago, A´ . Pen˜a-Gallego, and M. Merced Montero-Campillo, *Tetrahedron*, **65**, 2368 (2009).

72. A. Irigoras, J. M.Mercero, I. Silanes, and J. M. Ugalde, *J. Am. Chem. Soc.*, **123**, 5040 (2001).

73. M. Scheibitz, R. F. Winter, M. Bolte, H.-W. Lerner, and M. Wagner, *Angew. Chem. Int. Ed.*, **42**, 924 (2003).

74. N. Grover, M. Sankar, Y. Song, and K. M. Kadish, *Inorg. Chem.*, **55**, 584 (2016).

75. M. Boulkroune, L. Ignatovich, V. Muravenko, J. Spura, A. Chibani, and V. Jouikov,

Chem. Heterocyclic Compounds, **49**, 1579 (2014).

76. S. Zhu, Q. Song, S. Zhang, and Y. Ding, *J. Molecul. Struct.*, **1035**, 224 (2013).

77. T. Fujimoto, M. M. Matsushita, and K. Awaga, *J. Phys. Chem. C*, **117**, 5552 (2013).

78. M. Schmittel, Q. Shu, and M. E. Cinar, *Dalton Transact*., **41**, 6064 (2012).

79. K. R. Edelman and B. J. Holliday, *Inorg. Chem.*, **49**, 6787 (2010).

80. A. A. Popov, I. E. Kareev, N. B. Shustova, E. B. Stukalin, S. F. Lebedkin, K. Seppelt, S. H. Strauss, O. V. Boltalina, and L. Dunsch, *J. Am. Chem. Soc.*, **129**, 11551 (2007).

81. G. V. Loukova and V. V. Strelets, *Russ. Chem. Bull.*, **49**, 1037 (2000).

Chapter 4:

Role of intramolecular hydrogen bonds in promoting electron flow through amino acid and oligopeptide conjugates.

Abstract

Elucidating the factors that control charge transfer rates in relatively small flexible conjugates is of importance for understanding energy flows in biology as well as assisting the design and construction of electronic devices. Here we report ultrafast electron transfer (ET) and hole transfer (HT) between a donor, corrole (Cor), linked to a perylene-diimide (PDI) acceptor by a tetrameric alanine $(Ala)_4$. Selective photoexcitation of the donor and acceptor triggers subpicosecond and picosecond ET and HT. Since replacement of the $(Ala)_4$ linker with either a single alanine or phenylalanine does not substantially affect the ET and HT kinetics, we conclude that electronic coupling involving only covalent bonds along the tetramer backbone is not a factor in these reactions. Direct donor-acceptor interactions are not likely either, as the ground-state optical spectra are not perturbed in the linked conjugates. Employing a combination of NMR, circular dichroism and computational studies, we show that intramolecular hydrogen bonding brings the donor and the acceptor close together, in 'scorpion-like' molecular architecture, thereby accounting for the unusually high ET and HT rates. The unique pattern relies on (Cor)NH···O=C-NH···O=C(PDI) electronic-coupling pathway involving two pivotal hydrogen bonds and a central amide group as an effective transmitter. The strategy revealed herein not only provides guidelines for construction of

effective donor-acceptor assemblies linked by long flexible bridges, but it also sheds light on structural motifs for mediating efficient ET and HT in proteins.

Introduction

Many vital biological processes, including photosynthesis [1, 2], enzyme catalysis [3-5] and DNA repair [6-9], rely on electron transfer (ET) through proteins and nucleic acids [10-12]. As the redox centers and chromophores mediating charge transfer (CT) are normally separated by relatively long molecular distances (> 1 nm), the rates of ET and hole transfer (HT) depend critically on the media between donors and acceptors. It follows that the folding of biopolymer backbones plays a key role in governing CT properties.

Owing to the complexities of studying ET processes in biomacromolecules, model systems comprised of donor and acceptor units located at the termini of oligomeric bridges have been employed to gain insight into the factors that control the redox behavior of biological systems. The evolution of biomimetic and bioinspired molecular devices also has become a major driving force for such studies [13]. Despite the inherent flexibility of natural biomolecular oligomers, rigid bridges are common for the myriad of synthetic CT systems [10, 14-19]. The difficulty in accounting for conformational dynamics has plagued interpretations of CT through peptides [20-22] and foldamers [23-25].

Long-range ET through covalent bonds in donor-bridge-acceptor (DBA) complexes has been the subject of numerous investigations over the last 40 years [10-12, 26]. Of particular interest has been work on rigidly linked donor-acceptor units in Ru-modified proteins that provided experimentally validated tunneling timetables for interpretation and prediction of ET

rates in structurally characterized DBA systems [10]. Theoretical work by Beratan and others has shed light on the factors that control these couplings both in small molecular DBA complexes and Ru-proteins [27].

Less well understood are couplings through solvents and other noncovalent molecular assemblies, especially those in DBA complexes that feature B-group hydrogen-bond interactions. In work reported here, we employ amino acids and an oligopeptide as bridges in corrole-peptide-perylenediimide DBA conjugates in order to elucidate the role of hydrogen bonds in mediating biomimetic ET reactions. Specifically, we focus attention on a tetrapeptide bridging group, $(Ala)_4$, which if extended would separate D and A and greatly diminish through-bond coupling. For comparison purposes, we also have investigated related DBA systems, one with a single alanine (Ala), another with phenylalanine (Phe) (Figure 4-1). Varying the number of bridging residues between one and four did not drastically alter the excited-state dynamics of the DBA conjugates. Here we show that intramolecular hydrogen bonding opens efficient DBA electronic coupling pathways for these CT reactions.

Design and synthesis.

The elaborate design of these dyads is based on the following principles: (i) propensity of free-base corroles to form strong hydrogen bonds; (ii) ability of short peptides to fold in *via* intramolecular C=O···HN hydrogen bonds; (iii) the presence of C=O in PDI which may contribute to the folding process again *via* hydrogen bonds; (iv) the proof from our earlier work that an efficient electron transfer occurs between corrole and PDI. Let us elaborate on points (i) and (iv).

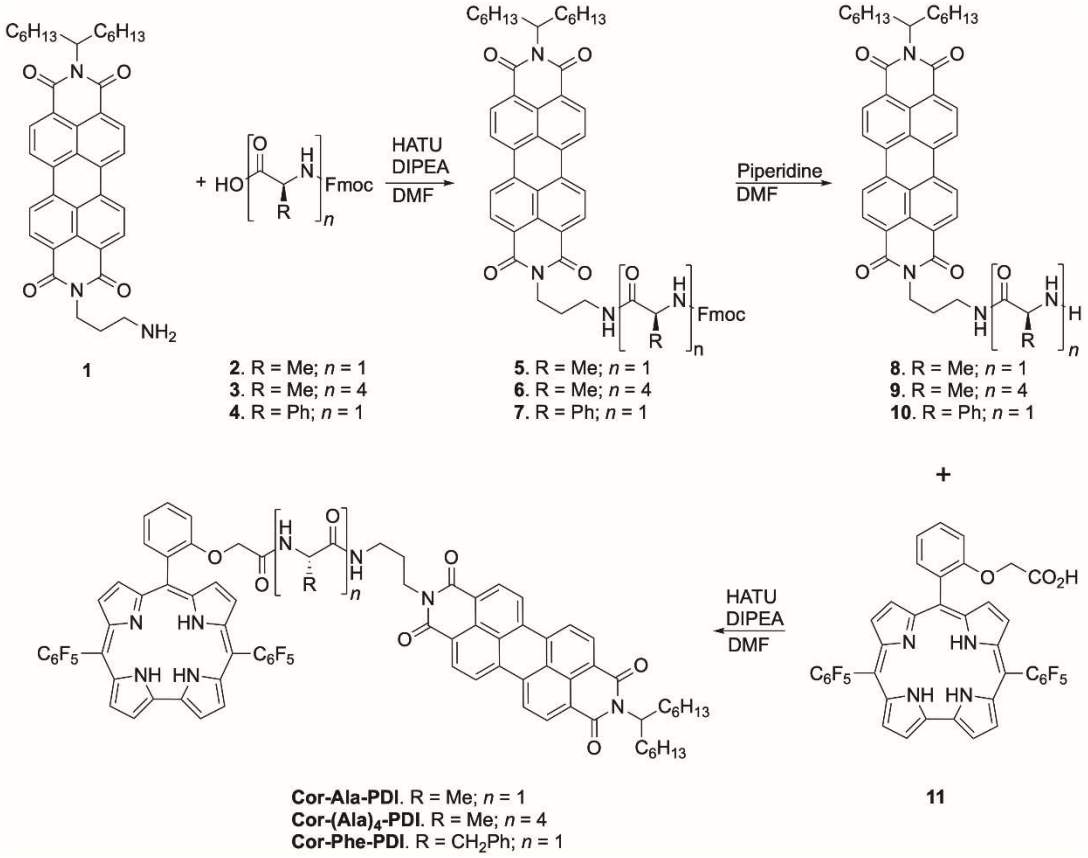

Scheme 4-1. Synthesis of **Cor-Ala-PDI**, **Cor-(Ala)$_4$-PDI** and **Cor-Phe-PDI**.

The exact design of the DBA features take advantage of a unique structural motif of amide-containing corroles that we recently discovered [28]. Specifically, *trans*-A_2B-corroles, bearing -OCH_2CONHR substituents at the *ortho* positions of the *meso*-phenyl group, exhibit a pronounced propensity for hydrogen bonding between the amide carbonyl and corrole-NH [29]. X-ray crystallography and NMR spectroscopy confirm this strong interaction between groups located at *meso*-10 position with the NH of the macrocyclic core in the solid state and in solution, respectively [28-30]. This hydrogen bonding always locks the amide group above the

corrole cavity, which results in pronounced upfield shift of the NMR signals of its protons (Δδ ≈ -3 ppm). We implement the same -OCH_2CONHR linker design in the DBA conjugates for this study (Scheme 4-1). Employing the same structural pattern will enable to rigidify dyad pointing the amino acid/peptide arm above the corrole core decreasing the distance between corrole and PDI in comparison with the extended conformations. Because of this intramolecular hydrogen bonding that perturbs the structure of macrocycle, we use **Cor-Phe** as a control for the electron donor (Figure 4-1). Critically important is the presence of two C_6F_5 groups at positions 5 and 15. Their strongly electron-withdrawing character ensures good stability of intrinsically not so stable corrole core [31].

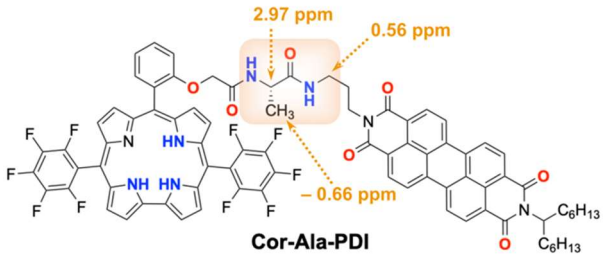

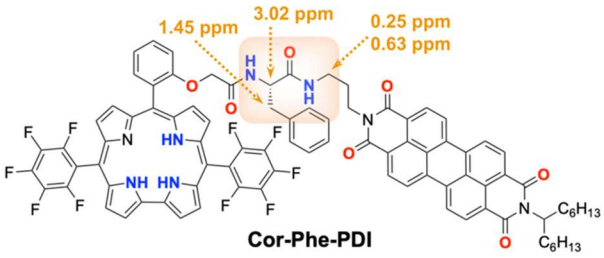

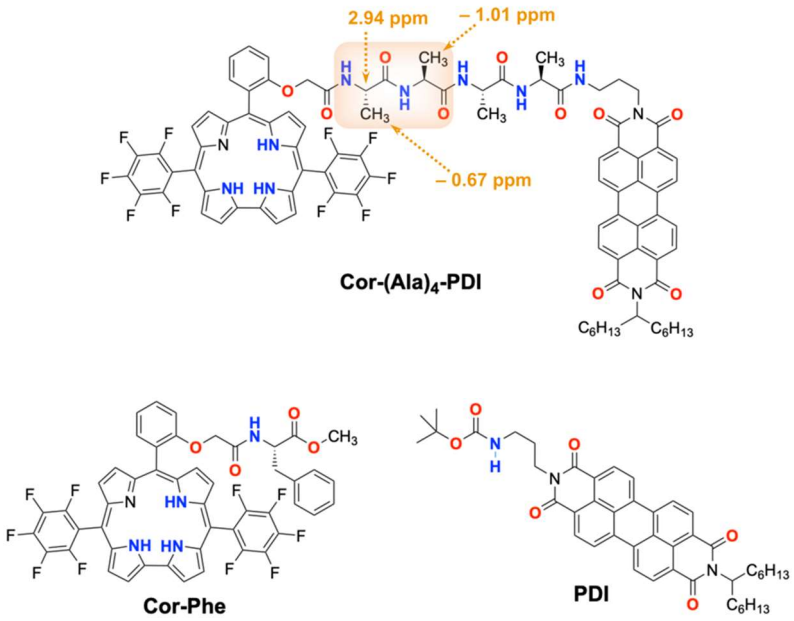

Figure 4-1. Structures of the DBA conjugates comprising a corrole derivative (Cor) as an electron donor, a perrylenediimide derivative (PDI) as an electron acceptor, along with the Cor-Phe and DPI used for controls. The hydrogen-bonding donors are highlighted in blue and the hydrogen-bond acceptors – in red. The listed upfield-shifted chemical shifts, obtained from ^{1}H NMR spectra, indicate for sections of the bridge (highlighted) that are above the plane of the Cor macrocycle.

Our work on charge-transfer (CT) dyads of covalently linked corrole (Cor) as an electron donor and perylenediimide (PDI) as an electron acceptor [32, 33] governs our choice for DBA scaffolds for this study. This choice allows for selective photoexcitation of the acceptor at the 460–530 nm region where Cor absorbs ≤10% of the light, and of the donor at its Soret band between 390 and 440 nm or at wavelengths longer than 570 nm (Figure 4-2). Selective excitation of Cor induces ET to the LUMO of the acceptor, and excitation of PDI induces hole transfer (HT) to the HOMO of the donor. In addition, the large overlap between the emission of PDI and the absorption of Cor indicate that the photoexcitation of PDI can also initiate Förster resonance energy transfer (EnT) from the electron acceptor to the electron donor, i.e.,

assuming randomized orientation of the transition dipole moments, R_0 for EnT from PDI to Cor is 46 Å.

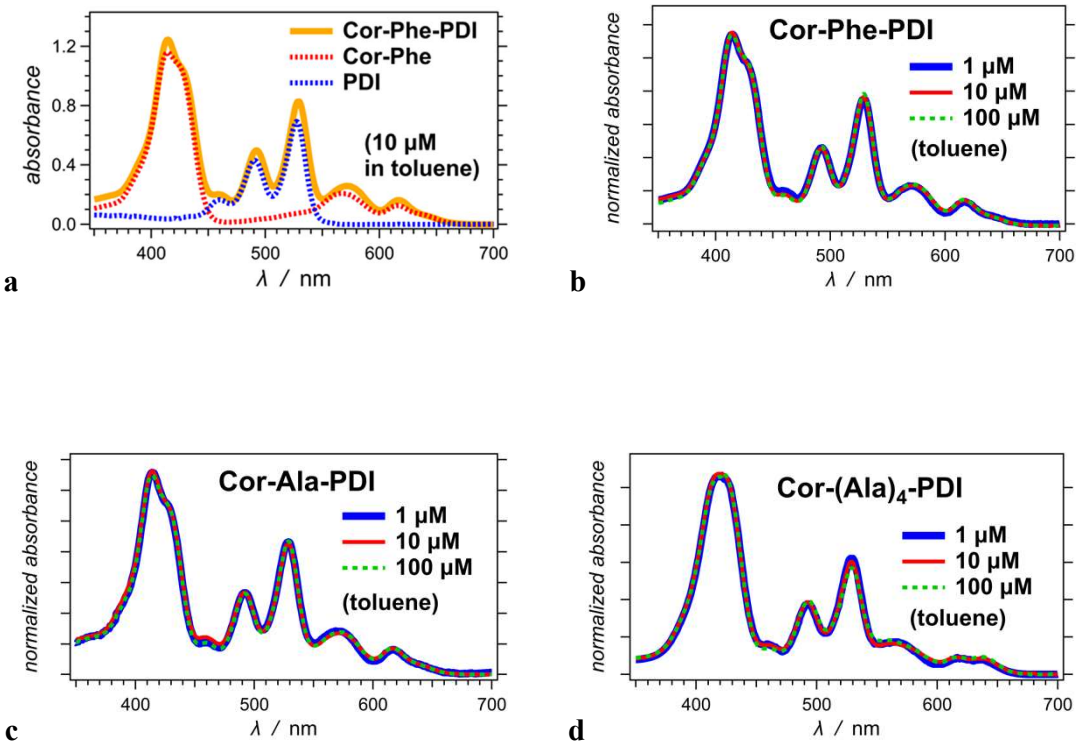

Figure 4-2. Optical absorption spectra of the DBA conjugates. (a) Comparison between the spectra of **Cor-Phe-PDI** and of its components, **Cor-Phe** and **PDI**. (b-d) Overplayed normalized absorption spectra of 1, 10 and 100 μM the DBA conjugates in toluene. For the measurements of 100 μM samples, we use 0.1-mm cuvettes.

A tetrapeptide bridge, such as $(Ala)_4$, in DBA conjugates provides two important features. (i) Adding 12 covalent bonds to a donor-acceptor electron-coupling pathway along the peptide backbone should cause a decrease in the CT rate constant, k_{CT}, that exceeds five orders of magnitude, i.e., $k_{CT} = k_{CT}(R_{DA}=0)\ (0.6^{12})^2 = 4.7\times10^{-6}\ k_{CT}(R_{DA}=0)$ [34]. This feature ensures that any alternative short pathway, involving hydrogen bonds or van der Waals contacts, can readily dominate the CT kinetics. (ii) While almost as flexible as glycines, alanines are heliogenic residues and usually fold into helical loops, which tend to have 3_{10} hydrogen-bonded configurations for short sequences [35-37]. The question arises how

intramolecular hydrogen bonding with the donor and the acceptor may alter the propensity for formation of such 3_{10} patterns?

Shortening the $(Ala)_4$ bridge to a single residue (Ala) or (Phe) should increase the rates of through-bond CT by about a factor of 50. Therefore, the **Cor-Ala-PDI** conjugate (Figure 4-1) serves as a control to test for contributions from through-covalent-bond coupling pathways to the CT kinetics. The side chains can play a role in protein CT by providing electronic-coupling pathways [38-40] and steric hindrance that preferentially tightens some of the conformational folds. The extra phenyl in the side chain of the bridge of the **Cor-Phe-PDI** DBA conjugate provides a means to test for such effects.

Retrosynthetic analysis of complex conjugates containing corroles reveals inherent challenges that warrant particular considerations. Synthesis of the tetrapyrrolic molecules, followed by modification of their peripheral groups for further derivatization, offers routes to complex systems containing a range of porphyrinoids [41]. The moderate stability of corroles, however, limits the number of transformations feasible for building blocks containing this macrocycle. Conversely, preparing elaborate aldehydes, which upon condensation with dipyrranes yield the final complex compounds containing *trans*-A_2B-corroles [42, 43], illustrates an alternative strategy.

The low solubility of perylenediimides presents additional synthetic challenges. While introducing various groups on the nitrogen atoms of PDI can immensely improve its solubility, the presence of amino-acids can induce aggregation that further hampers condensation reactions, as the reported rather low final yields suggest [44]. Hence, the considerable

complexity of the bridge-PDI aldehydes needed for the DBA conjugates (Figure 4-1) renders the strategy with the condensation as a last step unfeasible and unjustifiable.

These considerations led us to select a hybrid approach where the complexity of the aldehyde is just sufficient for the preparation of a *trans*-A_2B-corrole with an aliphatic carboxylate (**11**, Scheme 4-1) employing condensation and deprotection as our reports describe. Concurrently, using Fmoc protocol for peptide synthesis allows for building the DBA conjugates from the acceptor, attached to their C-termini, to the donor at their N-termini (Scheme 4-1). Coupling the Fmoc-protected bridges, **2-4**, to the amine of the PDI derivative, **1**, leads to the Fmoc-bridge-acceptor derivatives **5-7**. Base deprotection of the *N*-terminal amines yield the building blocks **8-9** (Scheme 1). As a final step under mild conditions, coupling of **11** with the *N*-terminal amines of **8-9** yields the DBA conjugates without compromising the integrity of the corrole ring (Scheme 1). The same coupling approach of **11** with phenylalanine methyl ester leads to the model **Cor-Phe** dyad (Figure 4-1).

The known benefits of HATU activation of carboxylates to induce large yields, high reaction speeds, and low epimerization, reflect our choice for this coupling reaction (Scheme 1) (45). The inherent challenges, which PDI and Cor moieties impose, leads to multiproduct mixtures from the HATU coupling reactions. Nevertheless, we isolate the intermediates and the final DBA products in acceptable yields.

Structural considerations.

Our recent studies on the self-organization of *trans*-A_2B-corroles bearing -OCH_2CONHR groups at *ortho* position of the *meso*-phenyl substituent revealed the propensity for formation of intramolecular hydrogen bonds between pyrrole NH groups and

the oxygen of the amide carbonyl [26-28]. In fact, **Cor-Phe** has four hydrogen-bond donors and four hydrogen-bond acceptors; **Cor-Ala-PDI** and **Cor-Phe-PDI** – five hydrogen-bond donor and seven acceptors (two of the seven are on the distal end of PDI, however); and **Cor-(Ala)$_4$-PDI** – eight hydrogen-bond donors and ten acceptors. Such high density of H-bonding groups, along with the flexibility of the bridges, make these conjugates highly prone to intramolecular hydrogen bonding, especially in non-polar media. Amides possess large electric dipole moments [46]; they can be stabilized by burial inside folded molecular structures in non-polar media.

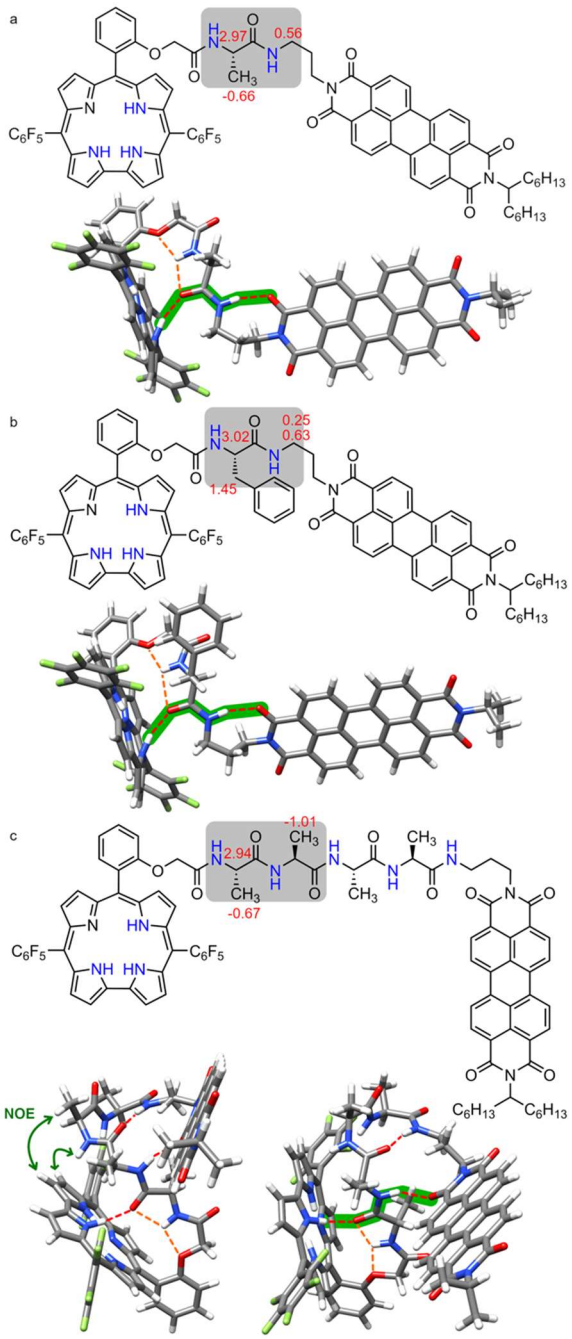

Figure 4-3. Structures of (a) **Cor-Ala-PDI**; (b) **Cor-Phe-PDI** and (c) **Cor-(Ala)$_4$-PDI**, with geometries optimized, using DFT at a B3LYP/6-31G(d,p) level of theory for chloroform. Crucial stabilizing hydrogen-bonding interactions are marked with red dashed lines. Shortest through-bond donor-acceptor electronic-coupling pathways, (Cor)NH···O=C-NH···O=C(PDI), are highlighted in green

Comparative analysis of ^{1}H NMR spectra, along with COSY, HSQC and HMBC, provide correlations for the conjugates that enables assignments of signals and reveals several key structural features. The ^{1}H and ^{13}C NMR spectra show that in **Cor-Ala-PDI**, **Cor-Phe-PDI** and **Cor-(Ala)$_4$-PDI** some signals of the linker are substantially upfield shifted with $\Delta\delta$ reaching −2.9 ppm with respect to their typical δ values. Considering the hydrogen-bonding propensity of the pyrroles with carbonyls from the linker, such upfield shifted signals correspond to protons that are located at similar distances from the corrole ring in three structures (Figure 1, 3). Upfield shifts, indeed, indicate for protons that are in proximity to the axis of the magnetic dipole originating from the current in the corrole macrocyclic ring induced by the external magnetic field. Furthermore, ROESY spectra of **Cor-(Ala)$_4$-PDI** show NOE through-space correlations that indicate for conformers with some of the β-protons of the corrole ring in proximity to the methyl and the *N*-terminal amide of the third alanine (Figure 3c).

These NMR findings, along with previously discussed X-ray results (28-30), provide key guidelines for constructing models of the structures of the DBA conjugates. Geometry optimization at DFT/B3LYP/6-31G(d,p) level of theory with implementation of PCM solvent model [(47)] yields structures that agree with the experimental findings (Figures 4-1, 4-3). For the structures containing single-residue linkers, i.e., **Cor-Ala-PDI** and **Cor-Phe-PDI**, the amino acid and the first methylene group from the aliphatic linker are above the corrole ring (Figure 4-3a,b**)**, which is consistent with the substantial upfield shifts of ^{1}H NMR signals of these groups (Figure 4-1). Intramolecular hydrogen bond between one of the corrole's NHs and the *C*-terminal carbonyl of the amino acid, along with favorable interactions of the amide NH (from *N*-terminus) with two oxygen atoms (one ethereal and the other carbonyl form the *C*-terminal), stabilize this part of a folding motif and leave one carbonyl oxygen (a hydrogen-

bond acceptor) and one amide hydrogen (a hydrogen-bond donor) available for further interactions. The calculations show that an additional engagement between the NH of the *C*-terminal amide of the amino acid and one of the carbonyl oxygen atoms of PDI leads to formation of a conformer with an eight-bond ring that is energetically favorable in low-polarity media. In chloroform, for example, such intramolecular hydrogen bonding with the acceptor and forming the folded conformer stabilizes the DBA conjugate extra 145 meV. This energy difference corresponds to about $5.7 \times k_B T$ for T = 20 ºC, suggesting that the folded conformer represents more than 99% of the population in solution. Formation of such a seam of hydrogen bonds brings the corrole and PDI close together, resulting in center-to-center donor-acceptor distance of 13.3 Å. In these folded structures an electronic-coupling pathway comprising two covalent and two hydrogen bonds emerges, i.e., (Cor)NH···O=C-NH···O=C(PDI) (Figure 3a,b).

While constructing a model for **Cor-(Ala)$_4$-PDI** we anticipate similar motif as in **Cor-Ala-PDI**. NMR data suggest structural similarities, placing two of the alanines within the aromatic-ring current of the corrole. For the construction of the remaining parts of the oligopeptide linker we initiate the analysis with structural preferences that short peptides composed of four alanines assume in the Cambridge Structural Database (CSD) (48). Our CSD search reveals that (Ala)$_4$ exhibits a high propensity for helical conformations in the solid state. The short length of (Ala)$_4$ sequence, however, makes its structure susceptible to perturbations by additional interactions. Despite the pronounced heliogenicity of alanine, helical geometries of (Ala)$_4$, such as α- and 3_{10}-helices, do not match the experimental data. The inherent directionality of α- and 3_{10}-helices orients the carbonyl oxygens of all amides away from the corrole plane, and none of them is available to form an intramolecular hydrogen bond with a pyrrole NH group.

Considering an extended conformation, i.e., β-strand, for the oligopeptide in **Cor-(Ala)$_4$-PDI**, and optimizing it using DFT/B3LYP/6-31G(d,p), for chloroform and toluene media as implemented by the PCM solvation model, converges to a structure in which: (i) the intramolecular hydrogen bond between a corrole NH group and the carbonyl oxygen atom of the first alanine is preserved (see ESI), and (ii) the first and second alanines are situated directly above the corrole plane, which is in agreement with the NMR data. The through-space center-to-center donor-acceptor distance in this fully extended structure is 19.8 Å, and the shortest through-bond electronic-coupling pathway comprises a stretch of 15 covalent bonds, which is unlikely to account for detectable photoinduced CT initiated by sensitizers with nanosecond singlet-excited-state lifetimes. Most importantly, extended conformation leaves three carbonyl oxygens and four amide hydrogens exposed, which is unlikely in non-polar aprotic media.

Implementing another common secondary-structure motif, β-turn-type, allows for favorable interactions between hydrogen-bond donors and acceptors that in the β-strand are exposed to the solvating environment. Geometry optimization yields a folded structure (Figure 4-3c) that is more or less isoenergetic with the extended one. In this folded structure, two new hydrogen bonds form. (i) between the carbonyl oxygen of the second alanine and the NH of the *C*-terminal amide of the oligopeptide meeting the criteria for a β-turn, that assumes a (*i*)←(*i*+3) hydrogen bonding pattern; and (ii) between NH of the second alanine and one of the oxygens of the PDA imide carbonyls (Figure 4-3c). While the energy gain from the later hydrogen bond, i.e., with the PDI carbonyl, is only about 40 meV, it is the synergy with former that stabilizes the folded structure and keeps the donor and the acceptor close together, i.e., center-to-center distance of 12.7 Å (Figure 4-3c). This intramolecular hydrogen bonding leads to the emergence of donor-acceptor electronic coupling pathway, (Cor)NH···O=C-

NH···O=C(PDI), that we observe for **Cor-Ala-PDI** and **Cor-Phe-PDI** (Figure 4-3). Along with the NMR results, these findings indicate that the folded conformers are highly abundant in the **Cor-(Ala)$_4$-PDI** solutions.

Indeed, we also considered other possible conformations, e.g., without a hydrogen bond to PDI or with β-turns connecting different residues, but they either are high-energy structures or do not account for some of the experimental findings. Therefore, our analysis indicates that folded structures of **Cor-Ala-PDI**, **Cor-Phe-PDI and Cor-(Ala)$_4$-PDI** accord with the observed photoinduced dynamics in non-polar solvents.

Optical properties.

Because the pyrrole rings in corroles are not coplanar, they have propensity for deprotonation in polar media even with weak basicity, such as nitrile and carbonyl solvents [(49)]. Therefore, toluene presents a good choice for a solvent for these studies.

Another key concern is the tendency of corroles and perylenediimides to aggregate. For each of the DBA conjugates (Figure 1), varying the concentration between 1 and 100 μM does not cause apparent broadening or shift of the absorption bands (Figure 4-2b-d). These findings suggest that the designed Cor and PDI derivatives (Figure 4-1) do not aggregate when dissolved in toluene at μM concentrations.

Furthermore, incorporating Cor and PDI into the DBA conjugates causes minute perturbations in their ground-state optical absorption, predominantly of the spectral band associated with the electron donor, Cor (Figure 4-2a). These small differences between the absorption spectra of

Cor and the DBA conjugates are most pronounced for **Cor-(Ala)$_4$-PDI** (Figure 4-2). We ascribe these subtle variations in the spectra to intramolecular interactions, such as hydrogen bonding, because of the lack of concentration dependence of the optical spectra (Figure 4-2b-d). Hydrogen-bonding induced tilts of the pyrrole rings out of the plane of the macrocycle affect the ground-state absorption of corroles.

Despite the small perturbations of the electronic spectra of Cor and PDI when conjugated with the peptide bridges, the lack of both significant broadening and of the appearance of CT bands preclude the possibility of π-stacking between the donor and the acceptor. Furthermore, the lack of apparent CT absorption bands in the DBA spectra suggests for weak donor-acceptor electronic coupling and diabatic CT mechanisms.

Attaching even a single amino acid residue with a stereogenic carbon center to the corrole moiety, i.e., **Cor-Phe**, introduces optical activity that is the most pronounced in the spectral region of its Soret band (Figure 4-4). Adding PDI to the structures, amplifies the electronic circular dichroism (ECD) signals; and changing the Ala bridge to Phe further enhances the optical activity of the DBA conjugates (Figure 4-4a,b). These findings suggest that the additional benzene and PDI moieties tighten structures in conformers with preferred chirality.

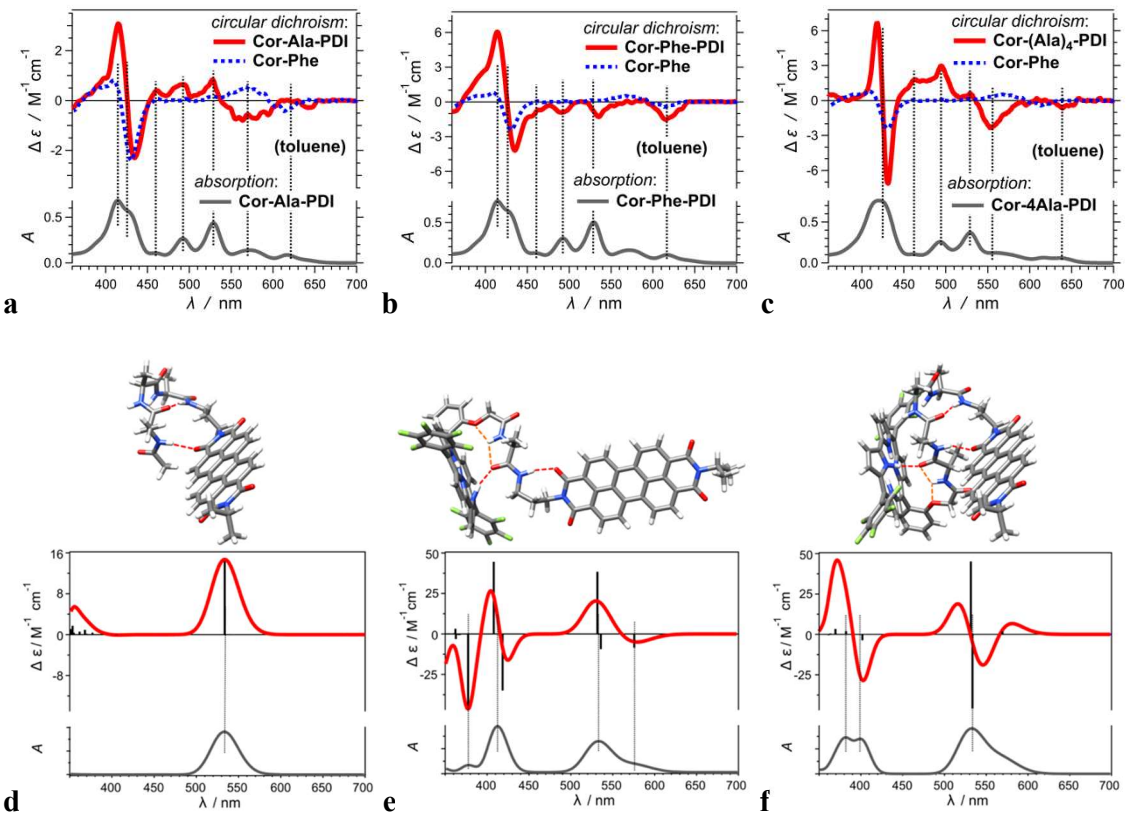

Figure 4-4. (a-c) Experimental electronic circular-dichroism (ECD) spectra of the three DBA conjugates for toluene, displayed along with the ECD spectrum of Cor-Phe. For comparison, the ground-state optical absorption spectra of the DBA compounds are displayed on the bottom of the graphs. (d-f) Theoretically calculated ECD and optical absorption spectra for: (d) PDI linked with a "partial" bridge structure, i.e., **Ac-(Ala)$_3$-PDI**; (e) **Cor-(Ala)-PDI**; and (f) **Cor-(Ala)$_4$-PDI**. The structures, calculated using TD-DFT at a B3LYP/6-31G(d,p) level of theory for toluene, are shown above the corresponding graph with computed spectra.

The shapes of the ECD bands of **Cor-Phe**, **Cor-Ala-PDI** and **Cor-Phe-PDI** suggests for negative Cotton effects originating from Davydov splitting of two vibronic transitions in the Soret band: (1) at about 426 nm, dominating the ECD signal; and (2) at the absorption maximum at about 413 nm, responsible for the hypsochromic ECD shoulder (Figure 4-4a,b).

The ECD spectrum of **Cor-(Ala)$_4$-PDI** reveals that the four-amino-acid bridge further tightens the structure, which also causes subtle changes in the ground-state optical absorption. The sharp ECD signals in the Soret-band region of this DBA conjugate lack the hypsochormic shoulder, i.e., they originate solely from a single vibronic transition (Figure 4-3c). Furthermore, **Cor-(Ala)$_4$-PDI** shows optical activity in spectral region where PDI absorbs (Figure 4-3c).

A chiral center that is not electronically coupled (e.g., π-conjugated) with a chromophore can induce optical activity by: (i) templating chiral assemblies of multiple chromophores with excitonically coupled electric transition dipoles causing magnetic transitions upon photoexcitation, which is the way protein amides and DNA bases produce the well-known distinct circular dichroism (CD) signals in the UV region [50-56]; and (ii) inducing twists or other chiral conformations in a single chromophore that produces magnetic transition dipole moments parallel to their electric transition dipoles (57). Because, the optical absorption spectra reveal a lack of aggregation (Figure 2b-d), we ascribe the observed optical activity of Cor to the latter. In all conjugates, the chiral center of the amino acid residue attached to Cor is about five covalent bonds away with reasonable conformational flexibility (Figure 4-1). Therefore, the induced optical activity suggests for folded structures. Indeed, Phe and PDI are aromatic moieties, but the absorption spectra of the conjugates do not reveal perturbations characteristic for intramolecular π-stacking.

The pyrrole rings of free-base corroles are always twisted out of the plane of the macrocycle (58). Intermolecular hydrogen bonding with a substituent containing an asymmetric center can readily introduce chirality in the arrangement in the twisting of the pyrroles leading to observed optical activity in the electronic transitions of the Cor chromophore. The relative rigidity of the PDI moiety, however, renders the induction of chiral

twisting in its structure by hydrogen bonding with the flexible bridges quite unlikely. The distinct ECD signal of **Cor-(Ala)$_4$-PDI** between 450 and 600 nm, therefore, originate either from the B-band transitions of Cor, or from excitonic coupling between the electric transition dipole moments of PDI and Cor. Indeed, this excitonic coupling does not need to be too strong and lead to detectible ground-state-absorption CT bands and in adiabatic CT kinetics. After all, the transitions with large rotatory strengths do not need to exhibit substantial molar extinction coefficients.

With the modeled structures in hand we calculate ECD spectra using TD DFT. In order to explore structural features that have dominating effects on ECD, we initially treat the two chromophores separately with fragments of the amino-acid bridge. Calculations for the PDI fragment indicate that the hydrogen bonding pattern, indeed, induces an ECD band. Furthermore, for the expected direction of a turn, the theoretically calculated ECD band has the same sign and shape as the band in the experimentally recorded spectrum (Figure 4-4d). For the corrole fragment the calculations reproduce well the energies of the bands and demonstrates that the signs of ECD effects are immensely sensitive to the tilts of the pyrrole rings and to the tautomeric form, i.e., which of the pyrrole rings is deprotonated. Thus, chirality of peptide linkers that are directly hydrogen bonded to the corrole ring affects these structural features. These initial findings allow us to proceed to calculating ECD spectra for the optimized geometries of **Cor-Ala-PDI** and **Cor-(Ala)$_4$-PDI** (Figure 4-4e,f). The differences between the relative intensities of the calculated and experimentally obtained bands is consistent with the inherent challenges for these computational methods to reproduce transition amplitudes. Conversely, the signs of the bands of the experimental and calculated spectra are in quite

reasonable agreement, confirming further the validity of the modeled folded structures that show the emergence of (Cor)NH···O=C-NH···O=C(PDI) motif in all three DBA conjugates.

Thermodynamic considerations for CT.

The reduction potentials for oxidizing Cor and reducing PDI ($E^{(1/2)}_{Cor^{\bullet+}|Cor}$ and $E^{(1/2)}_{PDI|PDI^{\bullet-}}$, respectively), along with their zero-to-zero energies (E_{00}) provide a means for estimating the driving forces for photoinduced CT in media with different dielectric constants, ε [59, 60]:

$$\Delta G^{(0)}_{CT}(\varepsilon) = F\left(E^{(1/2)}_{Cor^{\bullet+}|Cor}(\varepsilon_D) - E^{(1/2)}_{PDI|PDI^{\bullet-}}(\varepsilon_A)\right) - E_{00} + \Delta G_S + W \quad (1)$$

For $\Delta G_{ET}^{(0)}$, $E_{00} = E_{00}^{(Cor)}$; and for $\Delta G_{HT}^{(0)}$, $E_{00} = E_{00}^{(PDI)}$. While toluene is the medium of choice for the photoinduced CT studies, relatively polar media, with dielectric constants ε_D and ε_A, are essential for electrochemical determination of $E^{(1/2)}_{Cor^{\bullet+}|Cor}$ and $E^{(1/2)}_{PDI|PDI^{\bullet-}}$, respectively. The Coulombic work term, W, accounts for the interaction between $Cor^{\bullet+}$ and $PDI^{\bullet-}$. For n-electron transfer between a donor with an initial charge x and an acceptor with an initial charge y, the Born solvation term, ΔG_S, corrects for the differences between the polarities of the media for the CT studies and the electrochemical measurements (60):

$$\Delta G_S = \frac{nq_e^2}{8\pi\varepsilon_0}\left(\frac{2x+n}{r_D}\left(\frac{1}{\varepsilon} - \frac{1}{\varepsilon_D}\right) - \frac{2y-n}{r_A}\left(\frac{1}{\varepsilon} - \frac{1}{\varepsilon_A}\right)\right) \quad (2)$$

where q_e is the electron charge, and r_D and r_A are the effective radii of the donor and the acceptor, respectively.

The various protic equilibria of free-base corroles in polar media, however, present challenges for observing the direct oxidation of their non-charged forms needed for extracting the values of $E^{(1/2)}_{Cor^{\bullet+}|Cor}$ [61, 62]. Conversely, the readily measurable $E^{(1/2)}_{Cor|Cor^{\bullet-}}$ and $E_{00}^{(Cor)}$ provide a means for estimating the reduction potentials of oxidation of Cor, i.e., $E^{(1/2)}_{Cor^{\bullet+}|Cor} \approx E^{(1/2)}_{Cor|Cor^{\bullet-}} + E_{00}^{(Cor)}/F$. Indeed, this estimate assumes that $E_{ECh} \approx E_{00}$, where E_{ECh} is an electrochemical HOMO-LUMO gap, i.e., $E_{ECh}^{(Cor)} = F\left(E^{(1/2)}_{Cor^{\bullet+}|Cor} - E^{(1/2)}_{Cor|Cor^{\bullet-}}\right)$ [63]. While E_{ECh} can be slightly larger than E_{00}, such estimates based on the assumption that $E_{ECh} \approx E_{00}$, still reveal the important features of the CT thermodynamics.

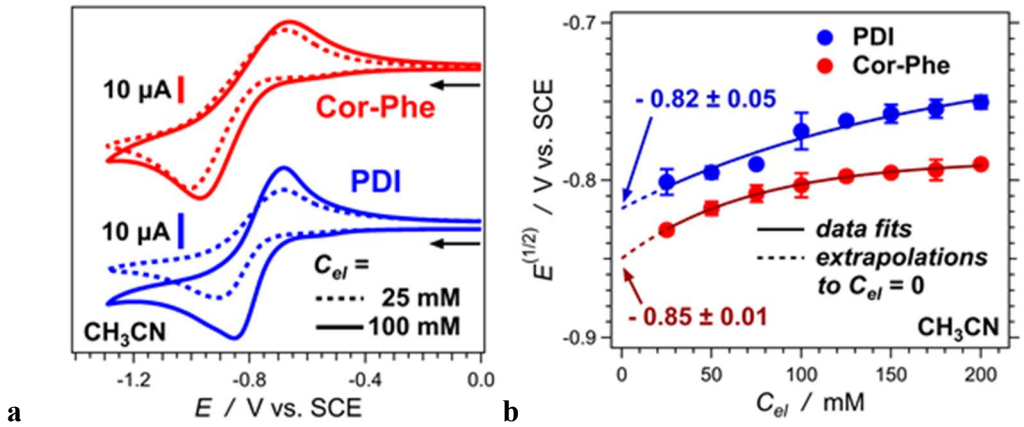

a **b**

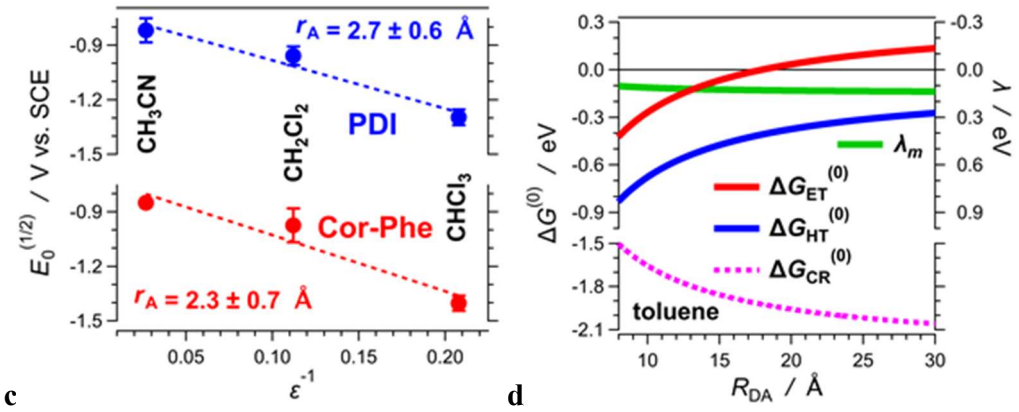

Figure 4-5. Electrochemical analysis of Cor-Phe and PDI. (a) Cyclic voltammograms for acetonitrile at 25 mM and 100 mM of electrolyte concentrations, C_{el}; (supporting electrolyte: $(n\text{-}C_4H_9)_4NClO_4$; scan rate, ν = 100 mV s^{-1}). (b) Dependence of the measured half-wave potentials, $E^{(1/2)}$, on the electrolyte concertation, along with the extrapolated values, $E_0^{(1/2)}$, for neat solvent, i.e., at C_{el} = 0 mM. (c) Dependence of the extrapolated values of the half-wave potentials for different solvents on the inverse dielectric constant of the solvent, proportional to the Born medium polarity, i.e., $1 - \varepsilon^{-1}$. The slopes of the linear data fits provide information about the effective radii of PDI, r_A, and of Cor, r_D, i.e., $E_0^{(1/2)} \propto -nq_e^2(8\pi\varepsilon_0 F r_X)^{-1}$, X = D or A (eq. 2). (d) Calculated thermodynamic driving forces for electron transfer, $-\Delta G_{ET}^{(0)}$, hole transfer, $-\Delta G_{HT}^{(0)}$, and charge recombination, $-\Delta G_{CR}^{(0)}$, for varying donor-acceptor center-to-center distance, R_{DA}; $-\Delta G_{CR}^{(0)} = \Delta G_{ET}^{(0)} + E_{00}^{(Cor)} = \Delta G_{HT}^{(0)} + E_{00}^{(PDI)}$ (eq. 1).

Cyclic voltammograms of PDI and Cor exhibit patterns of reversible reduction at about −1 to −0.7 V vs. SCE for CH_3CN solutions (Figure 5a). The peak potentials and the determined $E^{(1/2)}$ values depend on the concertation of the supporting electrolyte (Figure 5a,b) . Extrapolation to zero electrolyte concentration provides estimates for the values of the reduction potentials of PDI and Cor for neat CH_3CN (Figure 4-5b) [64-66]. Such extrapolated $E^{(1/2)}$ values for solvents with different polarity offer a means for extracting the values of r_D and r_A (Figure 4-5c) needed not only for calculating ΔG_S (eq. 2), but also for evaluating the outer-sphere, or medium, reorganization energy, λ_m (Figure 4-5d) [67].

Both, λ_m and W (eq.1), depend on the center-to-center donor-acceptor distance, R_{DA} (68). The relatively small values of λ_m for the non-polar medium place the HT processes in the Marcus inverted region or close to the tip of the Marcus curve, i.e., in the activationless regime, depending on R_{DA} and the inner reorganization energy (Figure 4-5d). Concurrently, $\Delta G_{ET}^{(0)}$ is within a couple of tenths of an eV from λ_m for R_{DA} ranging between 10 and 18 Å (Figure 5d), which ensures that ET operates at a close-to-optimal regime of $\Delta G_{ET}^{(0)} \approx -\lambda$. An increase in R_{DA} beyond about 18 Å, however, makes $\Delta G_{ET}^{(0)}$ positive and ET improbable (Figure 4-5d, Scheme 4-2). Conversely, the thermodynamics of the charge recombination (CR) step places its kinetics in the Marcus inverted region, i.e., increasing R_{DA} from 8 to 20 Å increase the CR driving force, $-\Delta G_{CR}^{(0)} = \Delta G_{CT}^{(0)} + E_{00}$, from about 1.5 to 2 eV.

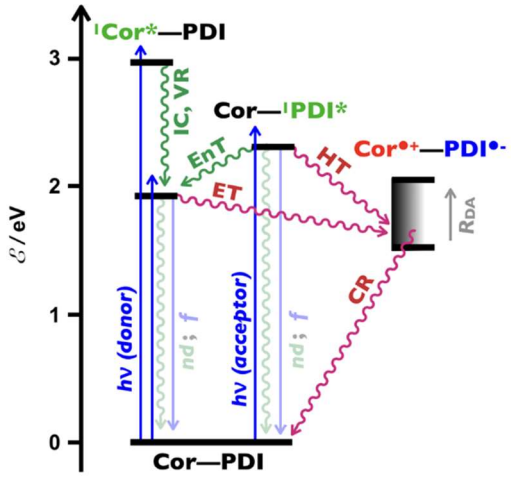

Scheme 4-2. Jabłoński diagram depicting the photoinduced processes in the Cor-PDI conjugates.

These findings suggest that a decrease in R_{DA} should slow HT and CR, as they would be further in the inverted region, while increasing the EnT rates and making ET the prevalent

CT process (Scheme 4-2). Conversely, an increase in R_{DA} beyond 18 Å shuts down ET, making HT the sole CT process. Under such circumstances of inactive ET, EnT, competing with HT, should produce electronically excited Cor that would undergo decay only to its ground state (Scheme 4-2).

Excited-state dynamics.

The electrochemical and photophysical analysis of **Cor-Phe** and **PDI** reveal immensely favorable thermodynamics for the formation of a CT state, **Cor$^{\bullet+}$–PDI$^{\bullet-}$**, via various pathways (Scheme 4-2). On the other hand, the length of the amino-acid linkers, especially of $(Ala)_4$, poses a question if the donor-acceptor coupling is strong enough to ensure CT rates that can compete with the deactivation times of the locally excited (LE) states, **^{1}Cor*** and **^{1}PDI*** (Scheme 4-2).

The fluorescence quantum yields, ϕ_f, of Cor and PDI show quenching of their emission when incorporated in the DBA conjugates. A selective excitation of the electron donor at 620 nm yields ϕ_f(**Cor-Phe**) = 0.15; ϕ_f(**Cor-Phe-PDI**) = 4.5×10^{-3}; ϕ_f(**Cor-Ala-PDI**) = 2.6×10^{-3} and ϕ_f(**Cor-(Ala)$_4$-PDI**) = 1.4×10^{-2}, which suggests for efficient ET even when four amino-acid residues link Cor with PDI. Excitation of the electron acceptor reveals that the quenching of its emission is more pronounced that the quenching of the emission of the donor, i.e., for λ_{ex} = 465 nm, ϕ_f(PDI) = 0.71; ϕ_f(**Cor-Phe-PDI**) = 1.4×10^{-3}; ϕ_f(**Cor-Ala-PDI**) = 9.1×10^{-4} and ϕ_f(**Cor-(Ala)$_4$-PDI**) = 5.1×10^{-3}. This finding suggests that on average HT for all three DBA conjugates is faster than ET.

Furthermore, ϕ_f of **Cor-Ala-PDI** is only about five times smaller than ϕ_f of **Cor-(Ala)$_4$-PDI**, regardless the excitation wavelength. The extra three Ala residues in the $(Ala)_4$ bridge

add nine covalent bonds to the donor-acceptor linker. For through-covalent-bond electronic coupling in this conjugates, therefore, the rates of ET and HT mediated by **Cor-Ala-PDI** should be four order of magnitude larger than the CT rates mediated by **Cor-(Ala)$_4$-PDI** [34, 69], which apparently is not the case. The excited-state lifetimes, τ, of **Cor-Phe** and **PDI** are 4.47 and 4.68 ns, respectively, as determined from monoexponential fits of emission decays recorded using time-correlated single-photon counting (TCSPC). These τ values correspond to radiative, k_f, and non-radiative, k_{nr}, decay rate constants that amount to $k_f = 3.3\times10^8$ s^{-1} and $k_{nr} = 1.9\times10^9$ s^{-1} for **Cor-Phe**, and to $k_f = 1.5\times10^9$ s^{-1} and $k_{nr} = 6.2\times10^8$ s^{-1} for **PDI**. These rate constants imply not only that ϕ_f(**Cor-(Ala)$_4$-PDI**) should be at least 50 or 500 times larger than ϕ_f(**Cor-Ala-PDI**), but also that the extend of quenching of ^{1}Cor* and ^{1}PDI* in **Cor-(Ala)$_4$-PDI** should not exceed 5%, considering that $\phi_f = k_f / (k_f + k_{nr} + k_{CT})$ where k_{CT} is a CT rate constant. In addition, the observed ϕ_f for **Cor-Ala-PDI** and **Cor-Phe-PDI** suggest for HT and ET rate constants, k_{HT} and k_{ET}, respectively, that exceed 10^{10} s^{-1}. The two amide and eight σ-bonds, linking the donor with the acceptor in **Cor-Ala-PDI** and **Cor-Phe-PDI** (Figure 1), however, cannot provide electronic coupling for such fast CT processes. This analysis, therefore, precludes major contributions from the electronic-coupling pathways, comprising only covalent bonds, to the CT processes responsible for the observed emission quenching.

The fluorescence decays of the three DBA conjugates exhibit a multiexponential character, with intensity-averaged lifetimes, $\langle\tau\rangle$, smaller than the lifetimes of **Cor-Phe** and **PDI**. This finding is consistent with emission quenching resulting from CT mediated by DBA conjugates with multiple conformers. As monitored at the corrole emission, however, the decreased in the lifetimes of the DBA conjugates, i.e., $\langle\tau\rangle_{\text{Cor-Phe-PDI}} = 0.16$ ns, $\langle\tau\rangle_{\text{Cor-Ala-PDI}} = 0.13$ ns and $\langle\tau\rangle_{\text{Cor-(Ala)4-DPI}} = 1.9$ ns, do not appear to account for major contributions from fast

ET and HT, i.e., $k_{CT} \gtrsim 10^{10}$ s^{-1}, as expected from the ϕ_f trends. Such a discrepancy is consistent with LE states of DBA conformers that have lifetimes considerably shorter than the low limits of the TCSPC dynamic range. Therefore, we resort to pump-probe spectroscopy to elucidate the excited-state dynamics of the CT conjugates (Scheme 2).

Table 4-1. Charge-transfer kinetics for the three DBA conjugates obtained from TA spectroscopy studies.

	λ_{ex} = 400 nm		λ_{ex} = 465 nm		
	$k_{ET} \times 10^{-10}$ / s^{-1}	$k_{CR} \times 10^{-10}$ / s^{-1}	$k_{HT/EnT} \times 10^{-10}$ / s^{-1}	$k_{ET} \times 10^{-10}$ / s^{-1}	$k_{CR} \times 10^{-10}$ / s^{-1}
Cor-Ala-PDI	27.9 ± 1.6 (0.39) 2.43 ± 0.08 (0.61)	0.156 ± 0.019	110 ± 4	3.12 ± 0.16	0.146 ± 0.034
Cor-Phe-PDI	20.9 ± 1.9 (0.35) 1.78 ± 0.06 (0.65)	0.0754 ± 0.0278	63.4 ± 12.6	1.41 ± 0.04	0.0455 ± 0.0084
Cor-(Ala)$_4$-PDI	36.2 ± 4.5 (0.36) 2.07 ± 0.13 (0.64)	0.0694 ± 0.0142	54.3 ± 26.6	1.59 ± 0.88	0.0625 ± 0.0195

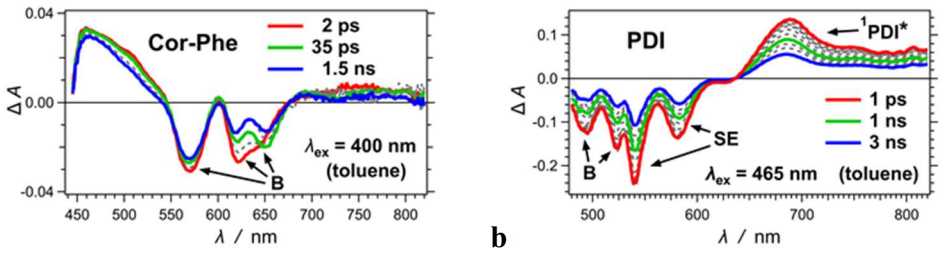

Figure 4-6. TA spectra of (a) Cor-Phe, λ_{ex} = 400 nm; and (b) PDI, λ_{ex} = 465 nm for toluene (B = ground-state bleach; SE = stimulated emission).

As transient absorption (TA) spectroscopy reveals, photoexcitation of the Cor in the DBA derivatives leads to a picosecond rise of PDI $^{\bullet-}$ and Cor$^{\bullet+}$ transients, absorbing between 650 and 850 nm (32), with concurrent appearance of bleach bands corresponding to the ground-state absorption of PDI (Figure 4-6, 4-7). Consistent with photoinduced ET, this TA dynamics shows similar heterogeneous kinetics for all three DBA conjugates with a fast components between 3 and 5 ps and slow components between 40 and 60 ps (Figure 4-7d-f, Table 4-1). This finding indicates that the donor-acceptor electronic coupling for all DBA conjugates is similar, regardless the length of the bridge. That is, the single amino acid linkers and the tetrameric oligo peptide fold preferentially in conformers that open very similar electronically coupled pathways.

The CR reactions of all DBA conjugates are about one to three orders of magnitude slower than the ET processes (Figure 4-7d-f, Table 4-1), which is consistent with the CT thermodynamics (Figure 5d). Conversely, the CR rates for **Cor-Phe-PDI** and **Cor-(Ala)$_4$-PDI** are twice slower than the CR for **Cor-Ala-PDI** (Table 4-1). This CR kinetics correlates with the CD results (Figure 4-4a-c), indicating that improving the definition of the secondary conformation decreases the CR efficiency, which can be corollary of: (i) suppressing

vibrational modes important for nuclear tunneling responsible for increased CR rates in the inverted region; or (ii) impeding exploration of conformations with improved electronic coupling between $PDI^{\bullet-}$ and $Cor^{\bullet+}$.

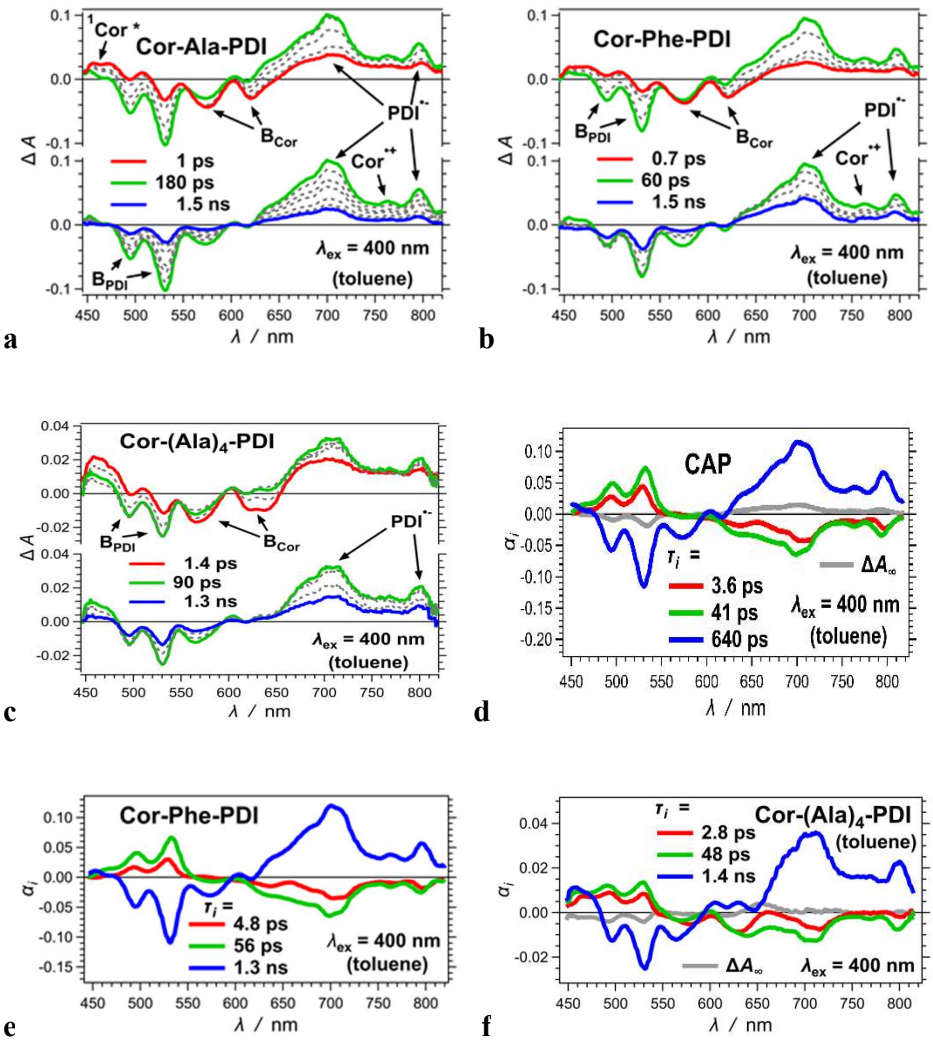

Figure 4-7. TA dynamics of the DBA conjugates upon excitation of the electron donor, Cor, at 400 nm. (a-c) TA spectra showing the ground-state bleach of the electron donor, B_{Cor}, and of the electron acceptor, B_{PDI}, along with the TA of the radical ions. (d-f) Spectral distribution of the preexponential parameters, α_i, obtained from multiexponential global fits, $\Delta A(t, \lambda) = \Delta A_\infty(\lambda) + \Sigma_i \alpha_i(\lambda) \exp(-t / \tau_i)$.

Photoexcitation of PDI shows the formation of its singlet-excited state characterized by its ground-state bleach, the stimulated emission and a broad TA signal in the 650–850 nm region (Figure 6b). Within 1–2 ps in the DBA conjugates, the PDI stimulated emission disappears and the broad ^{1}PDI * TA in the 650–850 nm changes shape into bands corresponding to the PDI$^{\bullet-}$ and Cor$^{\bullet+}$ transients (Figure 4-8). This TA dynamics is consistent with photoinduced HT to Cor. After these initial picosecond changes in the TA spectra, further increase in the radical-ion TA accompanies further growth of the PDI ground-state bleach (Figure 8d-f), which is consistent with ET from ^{1}Cor* to PDI as observed upon direct photoexcitation of the donor (Figure 4-7). The observation of ET with 30–70 ps timeconstants upon photoexcitation of the acceptor indicates that EnT from ^{1}PDI * to Cor accompanies the initial HT.

The changes in the TA spectra of the DBA conjugates when exciting the acceptor do not provide sufficient resolution for the global-fit analysis to discern the rates of the competing HT and EnT. Nevertheless, comparison between the amplitudes, $\alpha_i(\lambda)$, for the consequent ET and CR reveals that for **Cor-Ala-PDI** and **Cor-Phe-PDI** about 60% of the CT state originates from ET from ^{1}Cor* to PDI. For **Cor-(Ala)$_4$-PDI**, on the other hand, the direct HT from 1PDI* to Cor produces about 90% of the CT state. These findings indicate that **Cor-(Ala)$_4$-PDI** mediates EnT considerably less efficiently than the other two DBA conjugates.

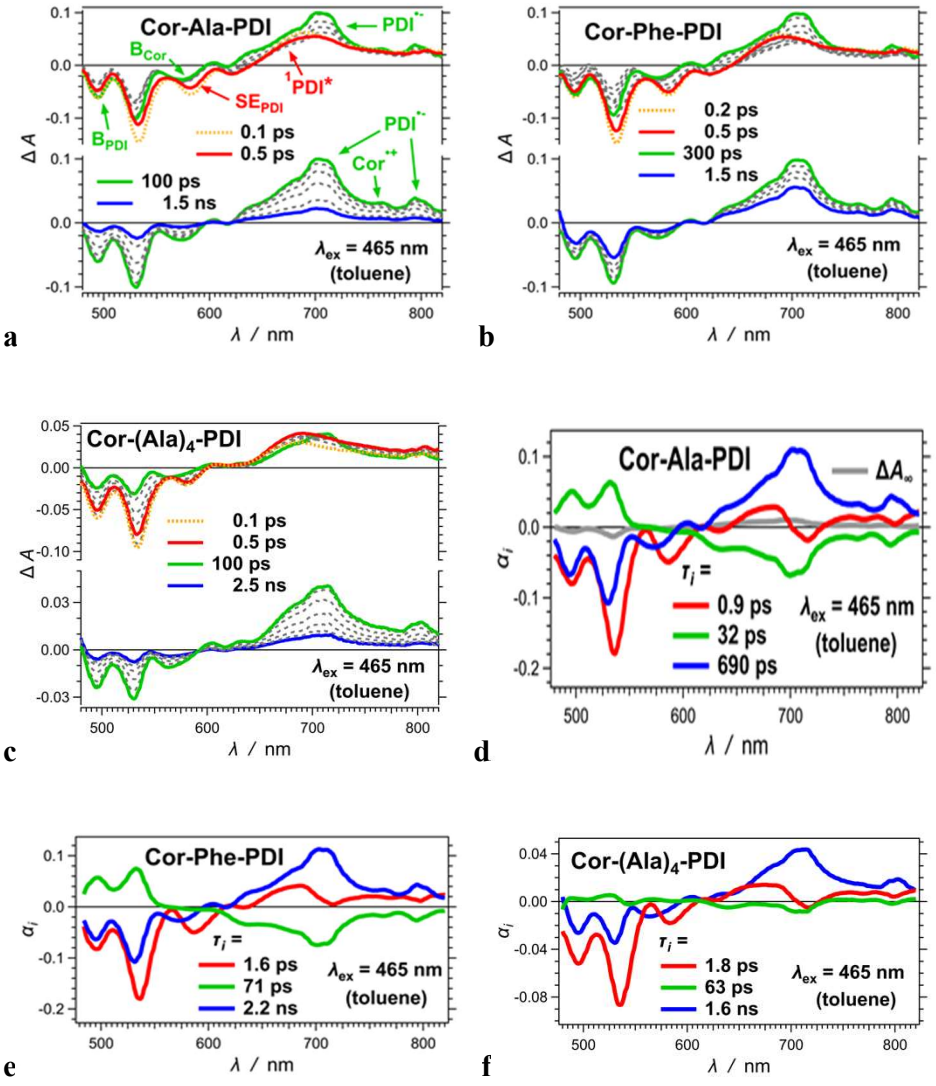

Figure 4-8. TA dynamics of the DBA conjugates upon excitation of the electron acceptor, PDI, at 465 nm. (a-c) TA spectra showing the ground-state bleach, B_{PDI}, the stimulated emission, SE_{PDI}, and the singlet-excited state, ^{1}PDI*, of the electron acceptor, at early times, that evolve into the ground-state bleach of the donor, B_{Cor}, and the TA of the radical ions. The spectral features of the two radical ions overlap in the 650 – 900 nm region, and the molar extinction coefficient of $PDI^{\bullet-}$ is overwhelmingly larger than that of $Cor^{\bullet+}$, making the TA of $Cor^{\bullet+}$ not always apparent. (d-f) Spectral distribution of the preexponential parameters, α_i, obtained from multiexponential global fits, $\Delta A(t, \lambda) = \Delta A_\infty(\lambda) + \Sigma_i\, \alpha_i(\lambda) \exp(-t / \tau_i)$.

While the calculated R_0 value of 46 Å assumes a random distribution of the orientation of the transition dipole moments of the donor and the acceptor, i.e., $\kappa = 2/3$, this assumption do not appear representative for these DBA conjugates and especially for **Cor-(Ala)$_4$-PDI**. As the CD results suggest, **Cor-(Ala)$_4$-PDI** has a preference for forming tight conformers in toluene (Figure 4-4c). The lowered EnT efficiency suggests that in these conformers the transition dipole moment for PDI emission is close to orthogonal to the transition dipole moment of Cor $S_0 \rightarrow S_1$ absorption responsible for the Q bands at the bathochromic edge of its spectrum.

CT kinetic analysis.

Semiclassical theory provides a platform for analysis of the observed picosecond CT processes (Table 1):

$$k_{CT} = \frac{2\pi}{\hbar\sqrt{4\pi\lambda k_B T}}|H_{DA}|^2 \exp\left(-\frac{\left(\Delta G_{CT}^{(0)} + \lambda\right)^2}{4\lambda k_B T}\right) \tag{3}$$

In (3), λ is the reorganization energy, comprising the inner, λ_v, and medium, λ_m, contributions, i.e., $\lambda = \lambda_v + \lambda_m$. Structures of the DBA conjugates, along with the Pekar factor, $\gamma = (n^{-2} - \varepsilon^{-1})$, allow estimation of λ_m, i.e., $\lambda_m = \gamma e^2(4\pi\varepsilon_0)^{-1}((2r_D)^{-1} + (2r_A)^{-1} - R_{DA}^{-1})$ (70). The pathway model, focusing on contributions from covalent bonds, $\epsilon^{(C)}$, and hydrogen bonds, $\epsilon^{(H)}$, allows an estimation of the donor-acceptor electronic coupling, i.e., $H_{DA} = H_{DA}^{(0)} \prod_i \epsilon_i^{(C)} \prod_i \epsilon_i^{(H)}$, where

$H_{DA}^{(0)}$ represents the electronic coupling when the donor and the acceptor are at direct contact, $\epsilon^{(C)} = 0.6$, $\epsilon^{(H)} = 0.36 \exp(-1.7\,(r_i^{(H)} - 2.8))$, and $r_i^{(H)}$ is the length of the i^{th} hydrogen bond (34).

The electrochemical and optical properties of Cor and PDI (Figure 5), the calculated structures (Figure 3), and the solvent characteristics, allow for estimating all parameters for the semiclassical analysis (eq. 3) except $H_{AD}^{(0)}$ and λ_v. As we previously reported (64, 66), varying both, $H_{AD}^{(0)}$ and λ_v, over three orders of magnitude reveals that for $H_{AD}^{(0)}$ ranging between 0.1 and 0.5 eV, and λ_v – between 0.2 and 0.6 eV, eq. 3 yields values of k_{CT} values that are in the range of measured k_{ET} and k_{HT} ones (Figure 4-9a,b and Table 4-1).

For CR, however, semiclassical theory does not yield plausible estimates of k_{CT}. For k_{CR} of about 10^9 s^{-1}, the magnitude of either λ_v or $H_{AD}^{(0)}$ has to exceed 1 eV (Figure 9c), which is highly unlikely. Therefore, for the analysis of CR kinetics, it is more reasonable to apply the Marcus-Levich-Jortner (MLJ) theory, as it includes nuclear tunneling pathways that come into play (71) when, as in our reactions, driving forces are deep in the Marcus inverted region:

$$k_{ET} = \frac{2\pi}{\hbar}|H_{DA}|^2 \frac{\exp\left(-\frac{\lambda_v}{h\nu_C}\right)}{\sqrt{4\pi\lambda_m k_B T}} \sum_{j=0}^{\infty} \frac{\left(\frac{\lambda_v}{h\nu_C}\right)^j}{j!} \exp\left(-\frac{\left(\Delta G_{CT}^{(0)} + \lambda_m + jh\nu_C\right)^2}{4\lambda_m k_B T}\right) \quad (4)$$

In (4), ν_C represents a single high frequency (or an average of frequencies). The inclusion of nuclear tunneling, according to MLJ, yields k_{CR} values of about 10^9 s^{-1} a for reasonable magnitudes of $H_{AD}^{(0)}$ and λ_v (Figure 4-9d-f). These findings indicate that high-frequency

tunneling occurs during CR, as there is an orders-of-magnitude increase in reaction rate (compare Figure 4-9c with 4-9d-f, and with Table 4-1).

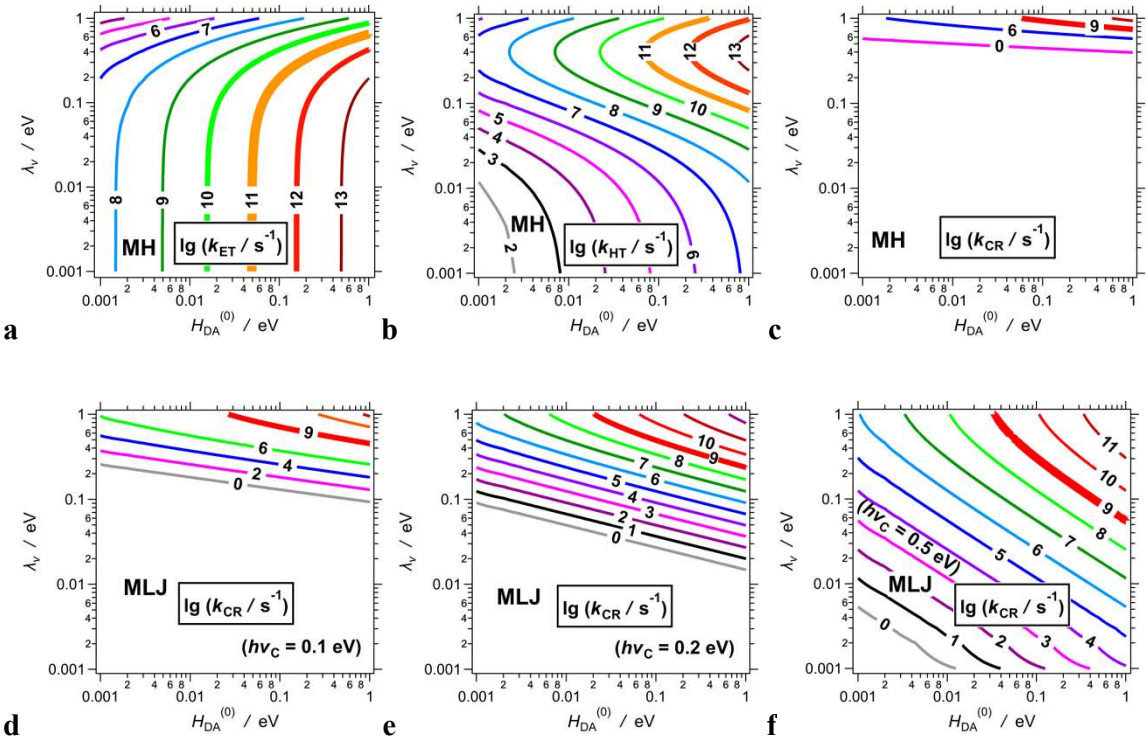

Figure 4-9. Dependence of the CT rate constants, k_{CT}, on the inner reorganization energy, λ_v, and the electronic coupling at zero donor-acceptor distance, $H_{DA}^{(0)}$, calculated for the folded conformation of **Cor-(Ala)$_4$-DPI** (Figure 3c) using (a-c) the Marcus-Hush (MH) formalism (eq. 3) and (d-f) the Marcus-Levich-Jortner (MLJ) formalism for different tunneling frequencies, ν_C (eq. 4). The estimates for the electronic coupling are for the (Cor)N-H···O=C–N-H···O(PDI) pathway, $H_{DA} = H_{DA}^{(0)} \prod_i \epsilon_i^{(C)} \prod_i \epsilon_i^{(H)}$, where $\boldsymbol{\epsilon}^{(C)} = 0.6$ for both covalent bonds, and $\epsilon^{(H)} = 0.36 \exp(-1.7\,(r_i^{(H)} - 2.8))$ with $r_{(Cor)N\text{-}H\cdots O}^{(H)} = 2.87$ Å and $r_{N\text{-}H\cdots O(PDI)}^{(H)} = 3.00$ Å, which along with $R_{DA} = 12.7$ Å, are obtained from the computed structure
In summary, the analysis (eq. 3,4) demonstrates that a CT pathway through a single H-bonded amide can strongly couple the donor to the acceptor, i.e., (Cor)NH···O=C–NH···O=C(PDI), accounting for picosecond reaction rates (Figure 4-9, Table 4-1).

Discussion

The comprehensive photophysical studies described above revealed that: (i) the rates of ET and HT are in the picosecond range; (ii) they are similar for all three DBA conjugates in

spite of apparent differences between the through-covalent-bond donor-acceptor distances. These picosecond rates of ET and HT suggest that the electronic-coupling pathways cannot comprise solely covalent bonds, since they would involve too many sp^3 carbons. Neither can they be π-π interactions, since absorption spectra show no perturbations attributable to π-stacking or any other strong donor-acceptor electronic coupling, precluding through van der Waals (through-space) CT pathways.

These considerations leave only one option: the one for which we conceived this research. Namely, the unprecedented propensity of the secondary amines of corroles to form tight hydrogen bonding with carbonyl and ether oxygens in the proximity of the macrocycle center set the foundation of our designs, i.e., we place the linker to the bridge at the *ortho* position of the central *meso* substituent (**11**, Scheme 1). Furthermore, peptide bridges provide a number of hydrogen-bond donors for linking with the carbonyls on the PDI acceptor. Flexibility of the donor-acceptor bridge allows for exploration of the conformational space and establishing hydrogen-bonding networks essential for efficient CT.

Folded structures with intramolecular hydrogen-bonding network have important implications on the kinetics of CT mediated by the DBA conjugates. The relatively large edge-to-edge donor-acceptor distances through the covalent bonds of the bridges renders the photoinduced CT processes quite inefficient for excited-state lifetimes of about 5 ns. Similar to proteins, intramolecular hydrogen-bonding networks can shorten donor-acceptor electronic-coupling pathways and substantially increase CT rates [(72)].

The close similarity of the CT dynamics for all three DBA conjugates (Table 4-1) suggests for similar through-space donor-acceptor distances and similar electronic-coupling

pathways, regardless the length of the bridge. The strong propensity of the pyrrole NH groups of the corrole for hydrogen bonding is crucial for shortening the electronic-coupling pathway between the donor and the middle of the bridge, which is part of the initial design. In addition, this study reveals another equally important structural feature: the tendency of the PDI imide carbonyls to interact with hydrogen-bond donors on the bridge (Figure 4-3). This hydrogen-bonding capabilities of the donor and the acceptor leads to an important recurring motif, (Cor)NH···O=C–NH···O=C(PDI). Such single amide from the middle of the bridge that hydrogen bonds with both, the donor and the acceptor, not only provides sufficiently strong electronic coupling between them to ensure picosecond CT rates, but also brings them close enough together to render ET possible, i.e., $R_{DA} < 18$ Å so that $\Delta G_{ET}^{(0)} < 0$ (Figure 4-5d).

Long flexible bridges in DBA systems tend to be problematic for CT kinetics. The long length of bridges can readily preclude through-covalent-bond CT. While bridge flexibility allows for exploration of DBA conformational space and for attaining the fraction of structures with strong enough donor-acceptor electronic coupling, it also can lead to heterogeneous CT kinetics that is often dominated by the molecular dynamics.

Secondary amides in the bridges, on the other hand, provide an incomparable means for addressing these challenges, when the electron donor and the acceptor are enriched with hydrogen-bond donors and acceptors. With dipole moments exceeding 4 D [46], amides are among the most polarized groups. Non-polar solvent media, therefore, forces folds where the amides are buried inside the molecular structures. Therefore, the flexibility of the linkers that contain secondary amides is an important benefit, allowing folds with propensity for a large degree of intramolecular hydrogen bonding.

Employing aprotic solvents ensures intramolecular hydrogen bonding and the formation of network of CT pathways providing strong donor-acceptor electronic coupling. Free hydrogen-bond donating and accepting cites are immensely unfavorable. It drives the formation of intramolecular hydrogen bonding networks. For example, satisfying all hydrogen-bonding cites at the termini of protein helices is crucial for stabilizing these secondary conformations [73, 74]

The three DBA conjugates, **Cor-(Ala)$_4$-PDI**, **Cor-Ala-PDI**, and **Cor-Phe-PDI**, provide an excellent biomimetic illustration of these design principles. Their relative simplicity, i.e., containing only one or four amino acids, reveals structure-function relationships that are of key importance to large proteins and other complex biomolecules and supramolecular assemblies. The complexity of the natural systems often makes the ascription of the structural features that strongly affect the CT functionality quite challenging. In the three DBA systems, we keep the number of amino acid residues in the bridge to four or less. This small number of residues ensure maximum one donor-acceptor electronic-coupling pathway that can provide CT rates fast enough to compete with the nanosecond deactivation of the locally excited states. This feature allows for avoiding constructive or destructive interference between parallel electronic-coupling pathways that can affect the CT kinetics [75].

For the motif emerging in the three DBA structures, i.e., (Cor)N-H···O=C–N-H···O(PDI), the pathway model predicts $H_{DA} = H_{DA}^{(0)} \prod_i \epsilon_i^{(C)} \prod_i \epsilon_i^{(H)} \approx 0.03\ H_{DA}^{(0)}$, considering the computed lengths of the two hydrogen bonds in **Cor-(Ala)$_4$-PDI**, $r_1^{(H)}$ and $r_2^{(H)}$, are 2.87 Å and 3.00 Å (Figure 3c). This model, indeed, suggests that the electronic-coupling pathway motif of an amide between two hydrogen bonds decreases the rates of CT by three orders of magnitude, i.e., $k_{CT} \propto |H_{DA}|^2$ (eq. 3,4). Describing the rate attenuation from all covalent bonds, $\epsilon^{(C)}$, with

the same parameter, 0.6, is a key feature of the pathway model. Treating sp^3–sp^3, sp^3–sp^2, and sp^2–sp^2 bonds the same allows the pathway model to provide straightforward and accurate descriptions of superexchange pathways for long-range CT. In the amide, however, both covalent bonds have sp^2–sp^2 character and the π-conjugation extends between the oxygen and the nitrogen with a node on the carbon for some of the frontier orbitals [76]. The π-orbitals of the amide are orthogonal to the hydrogen bonds and do not overlap with the frontier orbitals of the donor or the acceptor, i.e., validating $\epsilon^{(C)} = 0.6$. Conversely amides are relatively electron rich, i.e., $E^{(1/2)} \approx 1.5$ vs. SCE, allowing reasonable alignment of the energy levels of their HOMOs with those of the HOMOs of the donor and the acceptor, improving the efficiency of superexchange tunneling. Hence, it is feasible to assume that $0.03H_{DA}^{(0)}$ can be somewhat of an underestimate, but not by much. After all, the two hydrogen bonds contribute principally to the attenuation of the CT rates along this pathway, N-H⋯O=C–N-H⋯O.

Matching the driving force with the reorganization energy, i.e., $-\Delta G_{CT}^{(0)} \approx \lambda$, leads to picosecond CT even when the electronic-coupling pathway imposes such rate attenuations of three orders of magnitude (Figure 9a,b). For example, λ_v between 0.3 and 0.5 eV results in the best match between the total reorganization energy, λ, and the HT driving force, $-\Delta G_{HT}^{(0)}$, at $R_{DA} \approx 13$ Å (Figure 4-5d, 4-9b). For similarly high ET rates, λ_v has to be smaller than about 0.2 eV (Figure 4-9a). Because different locally excited states initiate ET and HT, it is reasonable to expect different inner reorganization energies, λ_v, for the two processes. Conversely, while the computed structures present static pictures of the most stable conformers, molecular dynamics inducing fluctuations in the PDI orientation and in the corrole exact position least to changes in the electronic coupling and in the center-to-center donor-acceptor distance, R_{DA}, which in its turn alters the driving forces and the medium reorganization energy (Figure 4-5d).

The heterogeneity of the measured HT and ET kinetics (Figure 7d-f and 8d-f) is consistent with the structural fluctuations of these DBA conjugates.

The structural motif with key importance for efficient CT, which emerges from this study, contains two hydrogen bonds with a secondary amide, i.e., N-H···O=C–N-H···O. This bridging motif of two hydrogen bonds, N-H···O, and two covalent bonds, C=O and C–N, is incomparably abundant in protein α-helices, 3_{10}-helices, β-sheets, and many other structures of biological significance. Therefore, understanding the details of how N-H···O=C–N-H···O mediates CT cannot be overstated. The short amino-acid bridges of these DBA systems, comprising an electron donor and acceptor capable of forming hydrogen bonds, are excellent biomimetics for examining CT through a motif prevalently abandoned in native proteins and other supramolecular structures.

Conclusions

The structure-function analysis of DBA conjugates, comprising peptide bridges, reveal important guidelines for molecular designs of efficient CT systems. When the electron donor and acceptor contain substituents capable of hydrogen bonding, aprotic non-polar (but polarizable) environment, while precluding π-π stacking, enforces folds and intramolecular interaction that can provide electronic-coupling pathways for efficient CT. Specifically, a (donor)N-H···O=C–N-H···O=C(acceptor) motif emerges as an electronic-coupling pathway for mediating picosecond CT. This amide-mediated hydrogen-bonding motif is vastly abundant in proteins and other natural molecules, making the elucidation of its CT capabilities crucially important for understanding energy flows in biology. Despite the diabatic nature of the forward ET and HT, their rate constants can exceed 10^{11} s^{-1}. Furthermore, the return CT, i.e., CR, even though aided by quantum mechanical nuclear tunneling, is one to three orders of magnitude slower than the initial photoinduced ET and HT. Relatively small DBA conjugates, such as the ones reported here, serve as important biomimetics not only for understanding the dynamics of ET and HT mediated by complex proteins and other natural supramolecular self-assemblies, but also for devising key bioinspired paradigms for energy science and engineering.

References

1. Ritz T, Damjanovic A, & Schulten K (2002). *Chemphyschem* 3(3):243-248

2. Nelson N & Yocum CF (2006). *Annu. Rev. Plant Biol.* 57:521-565.

3. Reece SY, Hodgkiss JM, Stubbe J, & Nocera DG (2006). *Philos. Trans. R. Soc. London, Ser. A* 361(1472):1351-1364.

4. Weinberg DR*, et al.* (2012). *Chem. Rev.*112(7):4016-4093.

5. Reece SY & Nocera DG (2009). *Annu. Rev. Biochem.* 78:673-699.

6. Jortner J, Bixon M, Langenbacher T, & Michel-Beyerle ME (1998). *PNAS* 95(22):12759-12765.

7. Reagan MS, Pittenger C, Siede W, & Friedberg EC (1995) *J. Bacteriol.* 177(2):364-371.

8. Sancar A, Lindsey-Boltz LA, Unsal-Kacmaz K, & Linn S (2004). *Annu. Rev. Biochem.* 73:39-85.

9. Rochaix JD (2011). *Biochimica Et Biophysica Acta-Bioenergetics* 1807(3):375-383.

10. Winkler JR & Gray HB (2016)(vol 114, pg 3369, 2014). *Chem. Rev.*116(14):COVER3-COVER3.

11. Gray HB & Winkler JR (2005). *PNAS* 102(10):3534-3539.

12. Winkler JR & Gray HB (2014). *J. Am. Chem. Soc* 136(8):2930-2939.

13. Vullev VI (2011) *J. Phys. Chem. Lett.* 2(5):503-508.

14. Scott AM, Ricks AB, Colvin MT, & Wasielewski MR (2010). *Angew. Chem. Int. Ed.*49(16):2904-2908.

15. Scott AM & Wasielewski MR (2011). *J. Am. Chem. Soc* 133(9):3005-3013.

16. Weiss EA, Wasielewski MR, & Ratner MA (2005). *Molecular Wires: from Design to Properties* 257:103-133.

17. Gilbert M & Albinsson B (2015). *Chem. Soc. Rev.* 44(4):845-862.

18. Wolffs M*, et al.* (2009). *J. Am. Chem. Soc* 131(13):4819-4829.

19. Li XS*, et al.* (2016). *J. Am. Chem. Soc* 138(41):13568-13578.

20. Giese B (2006). *Bioorg. Med. Chem.* 14(18):6139-6143.

21. Wagenknecht HA (2005)*Charge Transfer in DNA: from Mechanism to Application*:VII-VIII.

22. Jones G, Zhou X, & Vullev VI (2003). *Photochemical & Photobiological Sciences* 2(11):1080-1087.

23. Zeidan TA, Wang Q, Fiebig T, & Lewis FD (2007). *J. Am. Chem. Soc* 129(32):9848-.

24. Son M, Fimmel B, Dehm V, Wurthner F, & Kim D (2015). *Chemphyschem* 16(8):1757-1767.

25. Sebaoun L, Maurizot V, Granier T, Kauffmann B, & Huc I (2014). *J. Am. Chem. Soc* 136(5):2168-2174.

26. Guldi DM & Asmus KD (1997). *J. Am. Chem. Soc* 119(40):9588-9588.

27. Lin JP, Balabin IA, & Beratan DN (2005). *Science* 310(5752):1311-1313.

28. Orlowski R*, et al.* (2015). *Chem. Commun.* 51(39):8284-8287.

29. Orlowski R*, et al.* (2017). *Chem. Eur. J.*23(42):10195-10204.

30. Orlowski R*, et al.* (2019). *Chem. Eur. J.*25(41):9658-9664.

31. Orlowski R, Gryko D, & Gryko DT (2017). *Chem. Rev.*117(4):3102-3137.

32. Flamigni L*, et al.* (2008). *Chem. Eur. J.*14(1):169-183.

33. Tasior M*, et al.* (2008) . *J. Phys. Chem. C* 112(49):19699-19709.

34. Beratan DN, Betts JN, & Onuchic JN (1991). *Science* 252(5010):1285-1288.

35. Armen R, Alonso DOV, & Daggett V (2003). *Protein Sci.* 12(6):1145-1157.

36. Jones G, Willett P, Glen RC, Leach AR, & Taylor R (1997). *J. Mol. Biol.* 267(3):727-748.

37. Gresh N, Tiraboschi G, & Salahub DR (1998). *Biopolymers* 45(6):405-425.

38. Mandal I, Paul S, & Venkatramani R (2018). *Faraday Discuss.* 207:115-135.

39. Langen R*, et al.* (1995). *Science* 268(5218):1733-1735.

40. Ru XY, Zhang P, & Beratan DN (2019). *J. Phys. Chem. B* 123(24):5035-5047.

41. Holten D, Bocian DF, & Lindsey JS (2002). *Acc. Chem. Res.* 35(1):57-69.

42. Tasior M, Gryko DT, Pielachinska DJ, Zanelli A, & Flamigni L (2010). *Chem. Asian J.*5(1):130-140.

43. Ding T, Aleman EA, Modarelli DA, & Ziegler CJ (2005). *J. Phys. Chem. A* 109(33):7411-7417.

44. Fink AL (1998). *Fold Des.* 3(1):R9-R23.

45. Vrettos EI*, et al.* (2017). *Rsc Advances* 7(80):50519-50526.

46. Upadhyayula S*, et al.* (2011). *J. Phys. Chem. B* 115(30):9473-9490.

47. Frisch MJ*, et al.* (2009) Gaussian 09, Revision E.01 (Gaussian, Inc., Wallingford CT).

48. Allen FH (2002). *Acta Crystallogr., Sect. B: Struct. Sci* 58:380-388.

49. Straight SD*, et al.* (2005). *J. Am. Chem. Soc* 127(8):2717-2724.

50. Adler AJ*, et al.* (1974). *Biochemistry* 13(3):616-624.

51. Chou PY, Adler AJ, & Fasman GD (1975). *J. Mol. Biol.* 96(1):29-45.

52. Cowman MK & Fasman GD (1980) . *Biochemistry* 19(3):532-541.

53. Fasman GD (1979). *Federation Proceedings* 38(3):R9-R9.

54. Greenfie.N & Fasman GD (1969). *Biochemistry* 8(10):4108-&.

55. Perczel A, Park K, & Fasman GD (1992) *Anal. Biochem.* 203(1):83-93.

56. Hannah KC & Armitage BA (2004). *Acc. Chem. Res.* 37(11):845-853.

57. Crabbe P & Klyne W (1967). *Tetrahedron* 23(8):3449-&.

58. Paolesse R (2008). *Synlett* (15):2215-2230.

59. Rehm D & Weller A (1970). *Israel J. Chem.* 8(2):259-271.

60. Bao D*, et al.* (2009). *J. Phys. Chem. A* 113(7):1259-1267.

61. Fang YY, Ou ZP, & Kadish KM (2017). *Chem. Rev.* 117(4):3377-3419.

62. Shen J*, et al.* (2006). *Inorg. Chem.* 45(5):2251-2265.

63. Larsen-Clinton JM*, et al.* (2017). *Phys. Chem. Chem. Phys.*19(11):7871-7876.

64. Bao D*, et al.* (2014). *J. Am. Chem. Soc* 136(37):12966-12973.

65. Purc A*, et al.* (2016). *J. Am. Chem. Soc* 138(39):12826-12832.

66. Krzeszewski M*, et al.* (2018). *Angew. Chem., Int. Ed.* 57(38):12365-12369.

67. Espinoza EM*, et al.* (2019). *J. Electrochem. Soc.* 166(5):H3175-H3187.

68. Kuss-Petermann M & Wenger OS (2016). *Phys. Chem. Chem. Phys.* 18(28):18657-18664.

69. Heck A*, et al.* (2012). *J. Phys. Chem. B* 116(7):2284-2293.

70. Marcus RA & Sutin N (1985). *Biophys. Acta* 811(3):265-322.

71. Bixon M & Jortner J (1991). *J. Phys. Chem.* 95(5):1941-1944.

72. Jones G, II & Vullev VI (2002). *Org. Lett.* 4(23):4001-4004.

73. Maison W, Arce E, Renold P, Kennedy RJ, & Kemp DS (2001). *J. Am. Chem. Soc* 123(42):10245-10254.

74. Miller JS, Kennedy RJ, & Kemp DS (2001). *Biochemistry* 40(2):305-309.

75. Beratan DN*, et al.* (2009) *Acc. Chem. Res.* 42(10):1669-1678.

76. Espinoza EM*, et al.* (2018) . *ACS Omega* 3(10):12857-12867.